Technical University of Denmark

DTU

Representing vegetation processes in hydrometeorological simulations using the WRF model

Nielsen, Joakim Refslund; Dellwik, Ebba; Hahmann, Andrea N.; Boegh, Eva

Link back to DTU Orbit

DTU Library
Technical Information Center of Denmark

Representing vegetation processes in hydro-meteorological simulations using the WRF model

Risø-PhD-Report

Joakim Refslund Nielsen
Risø-PhD-0016(EN)
May 2013

DTU Wind Energy
Department of Wind Energy

Author: Joakim Refslund Nielsen
Title: Representing vegetation processes in hydrometeorological simulations using the WRF model
Department: DTU Wind Energy

Abstract:
For accurate predictions of weather and climate, it is important that the land surface and its processes are well represented. In a mesoscale model the land surface processes are calculated in a land surface model (LSM). These processes include exchanges of energy, water and momentum between the land surface components, such as vegetation and soil, and their interactions with the atmosphere. The land surface processes are complex and vary in time and space. Significant effort by the land surface community has therefore been invested in improving the LSMs over the recent decades. However, improvements are still needed in the representation of the land surface variability and of some key land surface processes.

This thesis explores two possibilities for improving the near-surface model predictions using the mesoscale Weather Research and Forecasting (WRF) model. In the first approach, data from satellite images were used to investigate the impact of accurate representation of vegetation fractions in the Noah LSM, which is the default LSM in WRF. In the second approach, advanced land surface parameterizations included in a new version of the Noah LSM with multiparameterization options (Noah-MP) were investigated.

A novel method was used to derive high-resolution, high-quality vegetation information from Moderate Resolution Imaging Spectroradiometer (MODIS) vegetation indices. The indices were converted into a vegetation fraction, which is a key parameter for the representation of vegetation in WRF, using both a linear and a quadratic approach. The quadratic approach was identified as superior over the linear approach for use in the WRF model. In addition, it was noted that vegetation seasonality during 2006 deviated significantly from its climatology over some regions of Europe, possibly due to the occurrence of heat wave and drought conditions. The results of the simulations over these regions obtained using the WRF model, at relatively low spatial resolution and using MODIS vegetation data sets, showed improved temperature predictions when using the quadratic approach.

The quadratic MODIS vegetation data and the default vegetation data in WRF were further used in high-resolution simulations over Denmark down to cloud-resolving scale (3 km). Results from two spatial resolutions were compared to investigate the influence of parametrized and resolved convection. The simulations using the parametrized convection showed large overestimations of precipitation during the summer, while the ones using resolved convection more accurately followed the observations. In general, equally good performance for precipitation, temperature and wind speed was found using both vegetation data sets. However, the MODIS data improved the simulation of the temporal evolution of the Bowen ratio during the summer. The work on the Noah-MP LSM included coupling, debugging and evaluation of its performance in the WRF modeling framework. In addition, new options were added, such that several thousand combinations of parameterization settings are now available. In this thesis, the model is presented together with an evaluation of its performance during a summer simulation using the current recommended options. The simulations show that good results are obtained for temperature and precipitation.

The thesis is submitted to the Danish Technical University in partial fulfilment of the requirements for the PhD degree.

Author: Joakim Refslund Nielsen
Title: Repræsentation of vegetations processer i hydrometeorologiske simuleringer ved brug af WRF modellen
Department: DTU Vindenergi

Dansk Resumé:

For nøjagtig forudsigelse of vejr og klima er det vigtig at landoverfladen, samt dens processer, er præcist repræsenteret. I en mesoskala model er landoverfladens processer beregnet i en landoverflade model (LSM). Disse processer inkluderer udvekslinger af energi, vand og impuls mellem landoverfladens komponenter, såsom vegetation og jorden, og deres interaktion med atmosfæren. Landoverfladens processer er komplekse og varierer i tid og rum. En betydelig indsats er derfor blevet udført for at forbedre landoverflade modeller i de seneste årtier. Der er dog stadig behov for forbedret repræsentation af landoverfladens variabilitet samt af visse vigtige landoverflade processer.

Denne afhandling undersøger to muligheder for at forbedre model forudsigelser nær overfladen ved hjælp af den mesoskala vejrprognose og forskningsmodel (WRF). I den første fremgangsmåde, data fra satellitbilleder blev anvendt til at undersøge virkningen af nøjagtig repræsentation af vegetations brøkdele i Noah LSM. I den anden fremgangsmåde, undersøges avancerede landoverflade parameteriseringer inkluderet i en ny Noah LSM med multiparameteriserings indstillingsmuligheder (Noah-MP).

En ny metode blev anvendt til at frembringe høj-opløst, høj-kvalitets vegetations brøkdele fra Moderate Resolution Imaging Spectro-radiometer (MODIS) vegetations-indekser. Indekserne blev omdannet til vegetations brøkdele ved hjælp af både en lineær og en kvadratisk fremgangsmåde. Den kvadratiske metode blev identificeret som overlegen overfor den linære metode til brug i WRF modellen. Desuden blev det bemærket at sæsonudsving i vegetationen i 2006 afveg signifikant fra dens klimatologi over nogle områder af Europa, muligvis på grund af perioder med varmebølger og tørke. Resultater af simuleringer over disse områder ved anvendelse af WRF modellen, ved relativ lav rumlig opløsning og ved brug af MODIS vegetations datasæt, viste forbedret forudsigelse af temperatur når den kvadratiske metode blev anvendt.

Det kvadratiske MODIS vegetation datasæt og standard vegetation datasættet i WRF blev yderligere anvendt i højt-opløste simuleringer over Danmark ned til sky-opløst skala (3 km). Resultaterne fra to rumlige opløsninger blev sammenlignet for at undersøge indflydelsen af parameteriseret og opløst konvektion. Den parameteriserede konvektion viste store overestimeringer af nedbøren, mens den opløste konvektion fulgte observationerne mere nøjagtigt. Generelt var resultaterne for nedbør, temperatur og vindhastighed lige gode i sommer perioden for begge vegetations datasæt. Dog forbedrede MODIS datasættet væsentligt simuleringen af den tidslige udvikling af Bowen forholdene i sommer perioden.

Arbejdet med Noah-MP LSM omfattede kobling, fejlsøgning og evaluering af dens ydeevne i rammerne af WRF modellen. Derudover blev nye instillingsmuligheder tilføjet således at flere tusinde kombinationer af parameteriserings muligheder er tilgængelige. I denne afhandling præsenteres modellen sammen med en evaluering of dens ydeevne under en sommer simulering ved brug af anbefalede instillingsmuligheder. Simuleringerne viser at der opnås gode resultater for temperatur og nedbør.

Preface

This thesis was written as part of the requirements for the PhD degree at the Technical University of Denmark. The work was carried out at Risø Campus except during a six months visit at the National Center for Atmospheric Research (NCAR), Boulder, USA. Financial support was provided by the Wind Energy Division, Technical University of Denmark, National Center for Atmospheric Research and the Danish Agency for Science Technology and Innovation (grant no. 274-08-0380).

Supervision of the research was done by Dr. Ebba Dellwik and Dr. Andrea N. Hahmann at DTU Wind Energy and Dr. Eva Boegh at Roskilde University. Supervision during the visit at NCAR was done by Dr. Michael J. Barlage.

The goal of the work presented in this thesis was to improve the representation of the land surface processes in the WRF model using satelitte measurements and improved land surface parameterizations. Initially, several suggestions to improve the roughness parameterizations in WRF were investigated. However, these investigations were abandoned in favour of developing new MODIS vegetation fraction data sets. A flexible method for this purpose was designed to ensure its use in future research applications at DTU Wind Energy. In addition, a plan to extend the Noah LSM with a seperate canopy layer was changed in favor of assisting in coupling, debugging and evaluating the new Noah-MP LSM in WRF. These taks have been interesting and challenging.

The main work done in this thesis is represented in Appendix A and B and in Chapter 5

Acknowledgements

I would like to express my thanks to my supervisors Ebba Dellwik, Andrea N. Hahmann and Eva Boegh for their scientific support, patience and their friendship. A special thanks go to Ebba for always being supportive, understanding and for helping me through rough times.

I am deeply grateful to Michael J. Barlage for hosting me at NCAR and for the many fruitful discussions, support and friendship. Thanks go to Kevin Manning, Mukul Tewari and Fei Chen for the pleasant working environment and interesting cakes during our friday meetings. Thanks to NCAR for giving me the opportunity to collaborate with such a strong scientific land surface group.

Many thanks to DTU Wind Energy for providing me with this opportunity. Special thanks to everyone at the MET group, for the pleasant and interesting working environment.

Many thanks to all of my office mates and fellow PhD students. Special thanks to Caroline Draxl, Ioanna Karagali and Claire Vincent for your help during the first part of my PhD and for letting me turn the office into an Ubuntu room! Your support has been invaluable.

I would like to thank my friends for their patience and support during these years. Finally, thanks to Tete for being with me all the way through this battle. I hope the future will be ours.

Contents

CHAPTER 1

Introduction

Quantitative predictions of climate change or weather prediction are primarily based on the use of complex numerical models that describe the many important processes within the atmosphere and climate system. These models have been updated and improved over many decades to increase their predictive skills but nevertheless significant uncertainties still remain in their predictions. The common goal within the modeling community is *to reduce model uncertanties*, which are being tackled through better understanding of the processes within the climate system. In the attempt of achieving this goal, comprehensive observational data sets play a key role for the improvement of the numerical methods, initialization and assimilation purposes, and for validation of model results.

Modeling of the Earth's climate is a tremendous task that is facilitated by dividing the model system into modules and submodules that handle the different components of the climate system. Improvements of the physical processes are therefore usually limited to a subset of the climate components, which allow initial test of the affected modules without the full interactions of the complex model system. Unfortunately, it is not certain that a physically more realistic module tested in offline conditions will improve the predictive skill when coupled to the full model. It is possible that the improved module will be incompatible with other modules (Niu et al., 2011) or that the climate might drift (Dirmeyer, 2001).

The physics schemes handle subgrid scale processes that are not resolved at the model grid spacing and these processes must be parametrized. A good parameterization should, in principal, describe the mechanism behind a physical process without too many tuning parameters. Nevertheless, all parameterizations include tuning parameters that cannot directly be derived from observations, and therefore increase the uncertainty of the models (Gulden et al., 2008). Thus, the modeling community engages in a constant battle of adding more physical realism

to the models without adding further uncertainties. The scheme that controls the land surface is referred to as the LSM.

The purpose of the LSM is to represent the processes that occur at the Earth's land surface and provide lower boundary conditions to the atmospheric model. These processes refer to exchanges of energy, water, momentum, aerosols and trace gases between the land components (soils, vegetation, snow, inland water, urban areas and more) and their interactions with the atmosphere (Yang, 2004). The land surface processes are complex and vary considerably due to the temporal and spatial variability in vegetation cover, soil moisture, snow cover, atmospheric forcing and more. For both weather and climate change predictions, it is important that the land surface and its processes are accurately represented by the LSM. For instance, the daytime sensible and latent heat fluxes affect the growth of the planetary boundary layer (PBL), the formation of cloud cover and can result in changes to the timing and location of convective precipitation (Pielke, 2001). However, the land surface characteristics may, on a wide range of time scales, be significantly altered by persistent weather conditions (such as omega blocks) or changes in climate, which result in changes in the land–atmosphere interactions.

For Europe, recent climate change studies have projected that the ongoing climate change will result in increased occurrence of summer heat waves, drought events and above-average high temperatures in the coming decades (Schär et al., 2004, Seneviratne et al., 2006, Teuling et al., 2010). Such events will inevitably influence the land surface conditions and result in large impacts of the vegetation cover and its seasonality. Changes of the land cover characteristics will influence the surface energy distribution and lead to altered exchanges of heat and moisture between the land surface and the atmosphere. Heat waves and droughts are typically confined to smaller regions and may therefore not be significant in global climate assessments. However, it is important that regional climate assessments in areas regularly affected by these extreme events reflect both the intra-annual and inter-annual variability caused by climate changes.

The mesoscale Weather Research and Forecasting (WRF) model was originally intended as a state-of-the-art numerical weather prediction (NWP) system for research and weather forecasting purposes. However, it is now increasingly being used as a regional climate model (RCM) to perform dynamical downscaling of global reanalysis and IPCC climate scenarios simulations (Bukovsky and Karoly, 2009, Soares et al., 2012, Mooney et al., 2013). Although, the representation of vegetation cover and its seasonality is critical for accurate simulation of the land surface processes, many studies using the WRF model completely ignore the impact of altered vegetation phenology. In WRF, the vegetation cover and its seasonality is typically described using a default 5-year green vegetation fraction climatology derived nearly 20 years ago. Being a climatology, it is not able to describe interannual variations in vegetation cover and its low spatial resolution (~ 15 km) do not accommodate the high spatial resolution applied in many recent

regional climate simulations using WRF (Barstad et al., 2009, Soares et al., 2012, Warrach-Sagi et al., 2013).

The study presented in this thesis is part of the research project "Implementing Earth Observations, Advanced Satelitte based Sounders and Distributed Temperature Sensing for Effective Land Surface Representation in Water Resource Modeling". The initial proposal for this Ph.D project was to carry out research within mesoscale modeling focusing on the exchange of energy and water between the land surface and the atmosphere. The research goals should be achieved by (1) using satelitte observations for better representation of the land surface characteristics and (2) by improving the land surface parameterizations.

We selected the mesoscale WRF model for our investigations since it is routinely applied in research and commercial projects at DTU Wind Energy. For the first task, this thesis investigates the impact of accurate representation of vegetation cover in the Noah LSM coupled to the WRF model. The new vegetation cover has a profound impact on the energy and water exchanges and plays a key role for accurate description of the land surface characteristics. For the second task, an initial plan to extend the Noah LSM with a seperate canopy layer was abandoned in favor of assisting in coupling, debugging and improving a new Noah land surface model with multiparameterization options (NoahMP) in WRF. A research collaboration with the National Center for Atmospheric Research (NCAR), USA, was established and a 6 months "change of environment" at NCAR under guidance of Dr. Michael J. Barlage was carried out.

The main research questions addressed in this thesis are:

- Which method should be used concerning Moderate Resolution Imaging Spectroradiometer NDVI images to produce vegetation data for use in the Noah LSM?

- Do the use of concurrent vegetation data improve the predictive skill of near-surface variables using the Noah LSM in year-long simulations?

- Is the Noah-MP coupled to the WRF modeling framework improving WRF modeling results compared to using the Noah LSM and what can we learn from it?

The presented work is composed as follows. Chapter 2 introduces the background on land surface energy and moisture balances and motivates the importance of land cover for LSMs. The influence of extreme weather and climate change on vegetation phenology is represented in section 2.3 and followed by a historic overview of the evolution of LSMs. Chapter 3 introduces some observational data sets used in this thesis for validation purposes and investigate their weakness. Chapter 4 presents the Noah LSM and its important parameterizations for the work done in this thesis. This results in a motivation of the papers

presented in Appendix A and B. The Noah-MP LSM is introduced in Chapter 5 together with results from coupled WRF/Noah-MP seasonal simulations. Finally, a summary and a conclusion is given in Chapter 6 followed by future perspectives in Chapter 7.

Background

The main purpose of the LSM is as mentioned to provide accurate predictions of the land surface processes, which partly control the evolution of the near-surface meteorological conditions. The predictions of the land surface processes are complicated by the significant spatial and temporal heterogeneity of the Earth's surface. Often, a variety of land cover types coexist over smaller areas which can introduce local and regional scale atmospheric circulations that affects the surface climate. A well-known example of such circulation is the sea breeze circulation initially forced by temperature differences between water and land surfaces. However, similar circulations can also occur inland due to differences in land surface characteristics (Avissar and Pielke, 1989). Land surface characteristics such as albedo, leaf area index (LAI), roughness and emissivity influence the partitioning of the surface radiative forcing into radiative and turbulent fluxes and thus the overall energy and moisture balances.

The following section will briefly review the surface energy and moisture balances equations that arex the basis for all land surface models. This is followed by a description of land cover changes that may alter these balances.

2.1 Surface energy and moisture balance

The balance between the shortwave and longwave radiation at the Earth's surface determines the net radiation that is distributed between the land surface, the soil and its overlying atmosphere. The total amount of shortwave radiation that reaches the land surface can be described as

$$S_n = S_\downarrow - S_\uparrow = (1 - \alpha)S_\downarrow \tag{2.1.1}$$

where $S_\downarrow$ and $S_\uparrow$ represent shortwave incoming and outgoing solar radiation, respectively. The absorbed part of $S_\downarrow$ is represented by $(1 - \alpha)$ where α is the broadband albedo. It depends on the characteristics of the surface and for the most part on the direction of the solar irradiance. The net longwave radiation at the land surface can be written as

$$L_n = L_\downarrow - L_\uparrow = L_\downarrow - \varepsilon\sigma T_{rad}^4 \tag{2.1.2}$$

where $L_\downarrow$ and $L_\uparrow$ represent downward and upward longwave radiation, σ is the Stefan-Boltzmann constant and T_{rad} is the radiative temperature of the land surface. The emissivity (ε) defines the land surface relative ability to emit radiative energy and it equals absorptivity for a surface in thermal equilibrium. Equations 2.1.1 and 2.1.2 can be combined to an equation that expresses the net radiative flux at the land surface, written as

$$R_n = (1 - \alpha)S_\downarrow + L_\downarrow - \varepsilon\sigma T_{rad}^4 \tag{2.1.3}$$

where R_n represents the net radiation. The added energy into the land surface system, e.g. in daytime cloud-free conditions during the summer, is partitioned between sensible and latent heat fluxes and heating of the surface layer (including soil and vegetation), such that the surface energy balance may be written as

$$\frac{dH}{dt} = R_n - SH - \lambda E - G \tag{2.1.4}$$

where dH/dt represents heating of the surface layer. SH is the sensible heat flux, λE is the latent heat flux (λ represents latent heat of vaporization, fusion or sublimation) and G represent the soil heat flux. The surface energy balance is coupled to the moisture balance

$$\frac{dS_w}{dt} = P - E - R_s - R_d \tag{2.1.5}$$

through the evapotranspiration term (E), which encompass transpiration, soil evaporation, evaporation of intercepted water and sublimation from snow. dS_w/dt represents a change in water content within the soil layer, P is the precipitation rate and R_s and R_d indicate surface runoff and drainage (or baseflow if groundwater is included in the model). Both the surface energy and moisture balances depend on the carbon budget since it is important for photosynthesis and respiration processes that control plant transpiration. It can be written as

$$\Delta C_{leaf} = A_{leaf} - (S_s + S_t + S_r) \tag{2.1.6}$$

where C_{leaf} is the carbon mass allocated in leaves, A_{leaf} is the assimilated carbon mass in leaves while S_s, S_t and S_r are carbon losses due to leaf stresses, leaf turnover and respiration, respectively. The carbon budget is, however, in many LSM not implemented.

2.2   The importance of the land cover

Land cover changes will affect the surface energy and moisture budgets, represented in Equation 2.1.4 and 2.1.5, through modification of the land surface characteristics, such as albedo, leaf area index, surface roughness, soil texture, color and structure. Some land cover changes result in instant changes of the land surface characteristics, while others slowly adjust to a change in weather or climate.

Large changes of the land cover are typically a result of human intervention and an extreme example is urbanization. A study by Cotton and Pielke (2007) showed that urbanization can cause changes in rainfall and increase the frequency of extreme rain events. The impacts were primarily related to convergence zones, which altered the boundary layer structure, rather than a consequence of roughness changes. Sertel et al. (2010) found in a WRF modeling study that conversion of croplands and forested areas into urban resulted in increased surface temperatures. In addition, the impervious surfaces (soil structure change) of urban areas affect the moisture balance through reduced infiltration and increased surface runoff.

A more slow adjustment in land cover due to weather and climate is represented by vegetation and its seasonality. A study by Schwartz and Karl (1990) investigated the impact of green-up during spring. They found that early emergence of leaves resulted in reduced maximum daily temperatures due to the added transpiration, while the opposite occured when leaf emergence was delayed. An observational study by Durre and Wallace (2001) found that the diurnal temperature range during the warm season was affected by vegetation. They argued that simulation of the diurnal temperature range during the warm season required realistic representation of soil–vegetation–atmosphere interactions. These findings implies that improved prediction of surface temperatures and, therefore also the energy and moisture balances, requires accurate representation of vegetation phenology in addition to accurate soil moisture simulations.

The coupling between the surface energy and water balance is evapotranspiration, which for the most part occur through the process of transpiration by the vegetation. However, the different vegetation types have also different characteristics. For example, conversion of forests into croplands (deforestation) will tend to increase albedo, lower the surface roughness and hereby decrease both sensible and latent heat fluxes (Hahmann and Dickinson, 1997). This can result in less cloud formation with reduced precipitation as a consequence (Bonan, 2008). Thus, vegetation plays an important role for the land surface processes.

2.3   Heat waves and drought conditions

The impacts of increased greenhouse gases (GHG) on climate is an intense research area within the climate community. According to the IPCC (Field et al., 2012), there is strong evidence that GHG emissions have a significant impact on the mean state of the climate and on the variability of its properties. In a regional climate study of the 2003 European heat wave, Schär et al. (2004) found that increased GHG enhanced the temperature variability by up to 100% in central and eastern Europe. They argued that Europe might be experiencing enhanced summer climate variability in the future and that the frequency of heat waves and drought events might increase. The last decade has confirmed this trend with heat waves in 2003, 2006, 2010 and 2012 over Europe. These events were associated with widespread impact on human mortality, water shortages, ecosystem damages and crop failures and severe thunderstorm development (Teuling et al., 2010). Robine et al. (2008) estimated that about 70000 people died during the 2003 heat wave. In an observational study, Della-Marta et al. (2007) showed that the length of the western European heat waves had doubled since 1880. The importance of seasonal forecasting to detect heat wave events, like the unprecedent heat wave in 2003, has therefore become increasingly important.

The underlying mechanism for the increase in summer temperature variability is related to land surface – atmosphere feedbacks (Seneviratne et al., 2006, Vidale et al., 2007, Fischer et al., 2007, Hirschi et al., 2010). In particular, soil moisture feedbacks on temperature and precipitation through evapotranspiration was found to be very important. However, above-average temperatures and low soil moisture conditions will affect vegetation seasonalities and result in further changes in the energy and moisture balances (Zaitchik et al., 2006). For example, Teuling et al. (2010) showed that forests and grasslands have different adaptation strategies to heat wave conditions. Grasslands suppress initial heating through increased evaporation, while forest are conservative in their water use. Thus, forests may mitigate the impact of extreme heating during longer lasting heat waves with limited soil moisture availability, while grasslands eventually wilts. These strategies need to be accounted for in land surface models.

The enhanced interannual variability due to climate changes is a great challenge for land surface models. In addition to adequate parameterizations of the land surface processes in LSMs, these processes require accurate representation of the land cover and soil moisture conditions. Many LSMs represent vegetation phenology via climatological vegetation data, e.g. the Noah LSM, however, this approach may not be sufficiently accurate with increased climate variability. The models need to account for interannual variations of vegetation both in hindcast mode and for seasonal forecasting purposes. The former requires accurate satellite data to be included, while the latter depends on implementation of dynamic vegetation models. In addition, the soil moisture initialization is critical

for predicting these extreme heat wave events. However, the accuracy of such initialization is difficult to verify.

2.4 Historic overview of land surface models

Land surface models have become increasingly comprehensive during the last four decades to represent numerous interactions and feedbacks using complex parameterizations. In the following, a brief overview of the evolution of LSM are presented.

First generation

The first generation of LSMs represented the land surface processes in a simple way to solve the energy balance (Eq. 2.1.4). The very early models used prescribed albedo, assumed constant soil moisture and some models neglected soil heat storage (Bonan, 2008). Sensible and latent heat fluxes were described using bulk aerodynamic transfer equations. The influence of vegetation on the latent heat flux was implicitly parameterized as a function of soil wetness, using a so-called β factor (see section 4.1.1). This dimensionless weighting factor was multiplied by the potential evaporation (E_p) to adjust the latent heat flux to limited soil moisture conditions. E_p was defined as the latent heat flux that would occur over a water surface, given the atmospheric conditions. The hydrological cycle was later added using a simple bucket model to represent water storage in one soil layer (Manabe, 1969). This was parameterized using a field capacity of 15cm of water everywhere and a critical soil water taken as 75% of the field capacity. Excess soil water was characterized as runoff.

Second generation

Development of the second generation models was initiated by the model of Deardorff (1978). This model included a seperate vegetation canopy layer and a two-layer soil column. The vegetation canopy layer allowed calculation of both canopy and ground temperatures and distinguished between canopy and ground turbulent and radiative fluxes. The latent heat fluxes were seperated into evaporative fluxes from intercepted water, evaporation from soil and transpiration. The multiple soil layers were introduced to differentiate near-surface soil temperature and soil moisture from the deeper soil. This enabled a quick response of the upper soil layer to the daily temperatures and precipitation amounts, while the deeper layers responds at longer timescales.

Two famous second generation models are the Biosphere–Atmosphere Transfer scheme (BATS) (Dickinson et al., 1986, 1993) and the Simple Biosphere Model (SiB) (Sellers et al., 1986). These models are much more complex than the first

generation models. Their radiative transfer calculations considers optical properties of leaves, stems and soil in the canopy and distinguish between visible and near-infrared wavebands in direct and diffuse beams (Bonan, 2008). Absorption and emission of longwave radiation is included. Soil evapotranspiration is controlled by soil water and turbulent transfer at the ground, while stomata regulates transpiration using the multiplicative and empirical approach of Jarvis (1976). The soil water balance is solved using Richards equation and snow is represented as a seperate layer, although later extended to multiple layers (Pitman, 2003).

The land surface in these models is described by its vegetation and soil characteristics such as, fractional vegetation cover, vegetation height, leaf area index, root profile and soil texture. These datasets are provided by satellite products of high spatial resolution. BATS and SiB allowed seasonally varying vegetation fractions and leaf area indexes, however, it is now common to use constant vegetation fractions and letting vegetation seasonality be determined by the leaf area indexes. The second generation models are considered as a major milestone within land surface modeling.

Third generation

Third generation models utilize more advanced formulations of the response of stomata to the environmental factors. Instead of empirical formulations, third generation LSM use a biochemical model of photosynthesis (Farquhar et al., 1980) and semi-empirical models for stomatal conductance (Ball et al., 1987, Leuning, 1990, Collatz et al., 1992). The rate of photosynthesis is parametrized as function of rubisco or light limitations and stomatal conductance is related to net photosynthesis, relative humidity, leaf ambient CO_2 concentration and empirical constants depending on vegetation type. These new formulations have allowed simulation of atmospheric CO_2 into the models.

Next generation

The next generation models include simulation of the carbon cycle on land and simulation of vegetation dynamics. Vegetation dynamics can be simulated through changes in the existing land cover types (short-term dynamics) or include modification of the geographical distribution of vegetation types (long-term dynamics). The models hydrology are extended to include watersheed processes represented in irregular catchments (Bonan, 2008). In addition, dust entrainment, a source of aerosols into the atmosphere, and emissions of biogenic volatile organic compounds are being included for air quality purposes.

The land surface models used for this thesis is described in more detail in Chapter 4 and 5. The Noah LSM is based on a mixture of elements from the first and second generation models. It uses bulk aerodynamic transfer equations and

calculate evaporation based on potential evaporation (first generation). However, it also include multiple soil layers, a snow layer and distinguish between soil evaporation, evaporation of intercepted water and the Jarvis-type transpiration (second generation). In contrast, the options in Noah-MP LSM may represent implementations included in both second, third and next generation models. The Noah-MP results presented in this thesis correspond to implementations of the third generation models.

CHAPTER 3

Observational data

One main uncertainty in weather and climate modeling is caused by insufficient data availability, needed for better understanding of the complex processes in the climate system and for validation and initialization of model simulations. On larger scale, remote sensing and gridded data from land based measurement stations are the most widely used data sets for model evaluation. These typically include parameters such as precipitation, temperature and wind speed. However, recent advances in remote sensing have enabled validation agaits gridded soil moisture measurements of the uppermost soil column. These measurements are important for evaluation the performance of LSMs and can add credibility to precipitation measurements (Refslund et al., 2013b). In addition, they may contribute to improvements of seasonal forecasts in the future.

Measurements of the vertical distribution of temperature, moisture and wind speed in the lower atmosphere are also important, because of the tight coupling between the land surface and its overlaying atmosphere. These vertically resolved data are typically point measurements from radiosondes, mast data and advanced lidars (Floors et al., 2013) to describe more localized conditions. The absence of spatially distributed measurements of the energy balance terms and the soil moisture content in the deeper soil layers is, however, of greater concern for evaluation of LSMs.

This thesis only considers land measurements for validation of the modeling results. The following section compares two land-based observational gridded data sets (E-OBS and DMI Climate grid), for precipitation and surface temperature, for the area of Denmark. In addition, a new remotely sensed soil moisture product from the European Space Agency – Climate Change Initiative (ESA–CCI) soil moisture project (Wagner et al., 2012) is introduced.
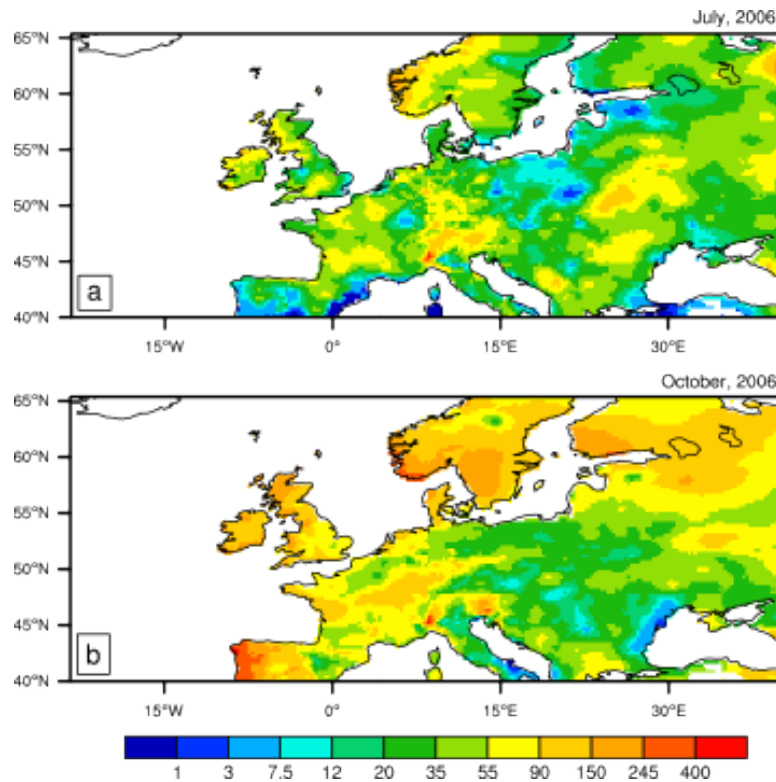
Figure 3.1.1: *Monthly accumulated precipitation (mm) represented by E-OBS for (a) July and (b) October during 2006. Horisontal resolution is 0.244º.*

3.1   E-OBS

Several land-based gridded data sets for analysis and evaluation of larger scale weather and climate conditions have been produced in recent years. Examples are the Climatic Research Unit (CRU, Harris et al. 2013) at the University of East Anglia and the European gridded data (E-OBS, Haylock et al. 2008). Only the observations represented in the E-OBS gridded data (version 5.0) is considered in this thesis.

The E-OBS data covers the period from 1950-2006 and was derived from daily observations of precipitation and minimum, maximum and mean surface temperature. It includes most part of Europe in a 25×25 km grid using over 2000 stations for the interpolations. The E-OBS data is frequently used for investigation of climatic trends in temperature and precipitation (Ylhäisi et al., 2010, Guttorp and Xu, 2011) and for validation of model simulations (Rauscher et al., 2009, García-Díez et al., 2012, Mooney et al., 2013).

Figure 3.1.1 shows two examples of the E-OBS accumulated precipitation over Europe during July and October 2006. In July, heat wave and drought conditions were significantly affecting large parts of Europe (Rebetez et al., 2009). The area of Poland was highly affected by missing rainfall as indicated in Fig. 3.1.1a.
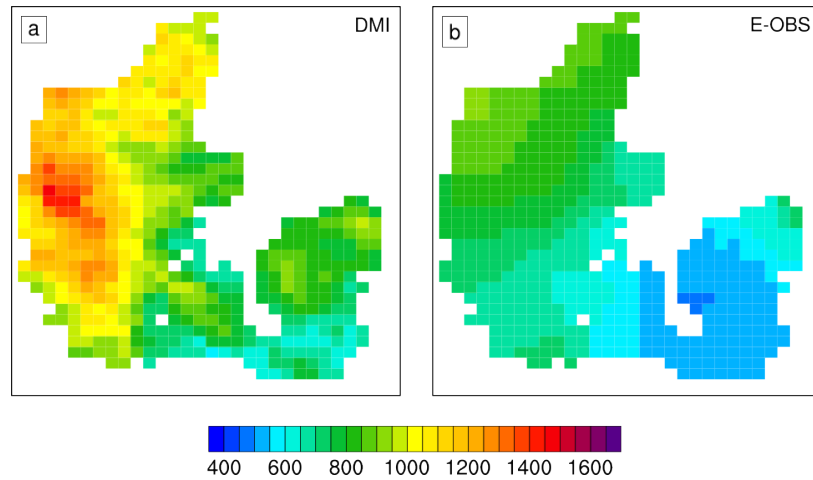
Figure 3.1.2: *Yearly accumulated precipitation (mm) over Denmark 2006 represented by (a) DMI and (b) E-OBS.*

This coincide with large modifications of the vegetation seasonalities compared to its climatological behavior Refslund et al. (2013a). Therefore, it is likely that the heat and drought conditions had large impact on the vegetation phenology. More precipitation fell during October as indicated in Fig. 3.1.1b, except in south-eastern Europe.

The uncertainties in E-OBS originate from the underlying station density, used in the interpolation processes, and from complex topography of certain areas. These uncertainties are mostly small for continouos variables but can be substantial for discontinouos variables (Hofstra et al., 2009, 2010). Especially, the convective precipitation can be severely underestimated in areas with low station density. However, Kyselý and Plavcová (2010) also found significant temperature biases in E-OBS when compared to station measurements. Therefore, it is important to compare and validate E-OBS to observational data sets produced from denser station networks. Such comparison is done below for the area of Denmark.

3.1.1   E-OBS versus DMI Climate grid

The Danish Meterological Institute has produced a high resolution, observational gridded data set for evaluation of model simulations: the DMI Climate grid (Scharling, 2012). This data is referred to as the DMI data in the following paragraphs and includes several observed meteorological parameters. However, only observations of 2-m temperature and precipitation are considered.

In comparison to the large spatial coverage of E-OBS (partly shown in Fig. 3.1.1), the DMI data represents the relatively small area of Denmark (43.050 km^2). The observed temperatures in the DMI data was produced from 78 SYNOP and climate stations, while more than 500 stations were included for precipitation.
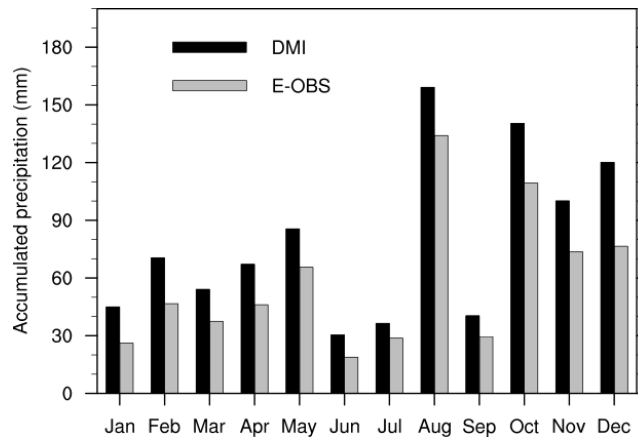
Figure 3.1.3: *Monthly accumulated precipitation (mm) over Denmark 2006 represented by (a) DMI and (b) E-OBS.*

The interpolated observed temperatures are produced in a 20×20 km grid, while observed precipitation uses a 10×10 km grid. The gridded precipitation of DMI was corrected for sheltering and wetting effects using standard corrections (Allerup et al., 1998), which range between 10 and 40%. In comparison, E-OBS represents the area of Denmark using 29 stations in the 25×25 km grid. The E-OBS data was regridded to the grid sizes applied by the DMI data using the method outlined in Refslund et al. (2013b). The high station density used in the derivation of the DMI data is a great advantage compared to E-OBS, and therefore it is considered as the most reliable.

Fig. 3.1.2 shows the yearly accumulated precipitation over Denmark represented by the DMI data and E-OBS. The figure indicates large differences in both the western and eastern regions of Denmark with E-OBS mostly showing lower precipitation. E-OBS represents about 50% less precipitation in the most western region compared to the DMI data. The average accumulated precipitation over Denmark shown by the DMI data is 950 mm, which is much higher than the 693 mm shown by E-OBS. In fact, the uncorrected value of DMI (777 mm) is also higher than the value represented in E-OBS. This discrepancy in observed precipitation is either due to the low station sampling in E-OBS, or that E-OBS accidently used uncorrected precipitation measurements from Denmark.

A montly view of the accumulated precipitation for the DMI data and E-OBS is shown in Fig. 3.1.3. Precipitation is underestimated in E-OBS in every month with 10-40 mm compared to the DMI data. The corrections applied to the DMI data during October, November and December were probably to large due to very mild weather conditions in the last part of 2006 (Refslund et al., 2013b). This would lower the DMI monthly precipitation measurements, however, precipitation would still be underestimated in E-OBS. Figure 3.1.2 and 3.1.3 show the importance of using high station density for deriving gridded precipitation
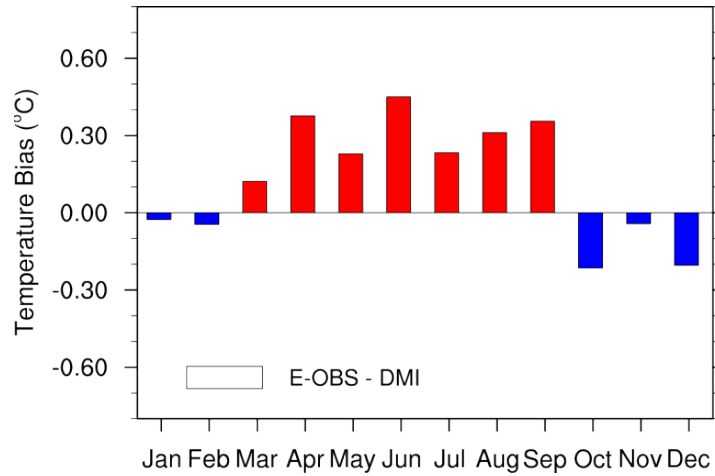
Figure 3.1.4: *Monthly average temperature biases (E-OBS – DMI) over Denmark 2006. Units in °C.*

data and that validation of simulated precipitation over Denmark should not be based on the measurements in E-OBS. Such validation could potentially lead to wrong conclusions about the performance of the model.

Finally, monthly averaged daily temperatures represented by the DMI data and E-OBS are shown in Fig. 3.1.4. The DMI daily temperature is the "true" station average, while mean temperature in E-OBS is derived as $\overline{T} = (T_{min} + T_{max})/2$. The figure shows that mean monthly temperatures in E-OBS are warmer than in the DMI data for the most part. The absolute biases are lower than 0.5°C during all of 2006. Negative biases are found during the winter months and late fall, while positive biases exist during the summer. However, the spatial agreement is good during all months (not shown). The DMI data and E-OBS share all of the 29 stations used in the derivation of temperature in E-OBS and, therefore it is not surprising that they show good agreement. In addition, errors resulting from complex topography are small since Denmark is generally flat.

3.2   Soil moisture data

Validation of land surface models is limited by the lack of comprehensive, spatially distributed measurements for several key parameters. Especially the lack of soil moisture measurements and the energy balance terms is of great concern. However, recent advances in the estimation of ground heat fluxes Verhoef et al. (2012) and measurements of soil moisture from satellites (Wagner et al., 2012) have great potential for improving both the predictions of LSMs and their validation.

The ESA-CCI soil moisture product (Wagner et al., 2012) was used by Refslund et al. (2013b) to validate the soil moisture predictions of the Noah LSM and,
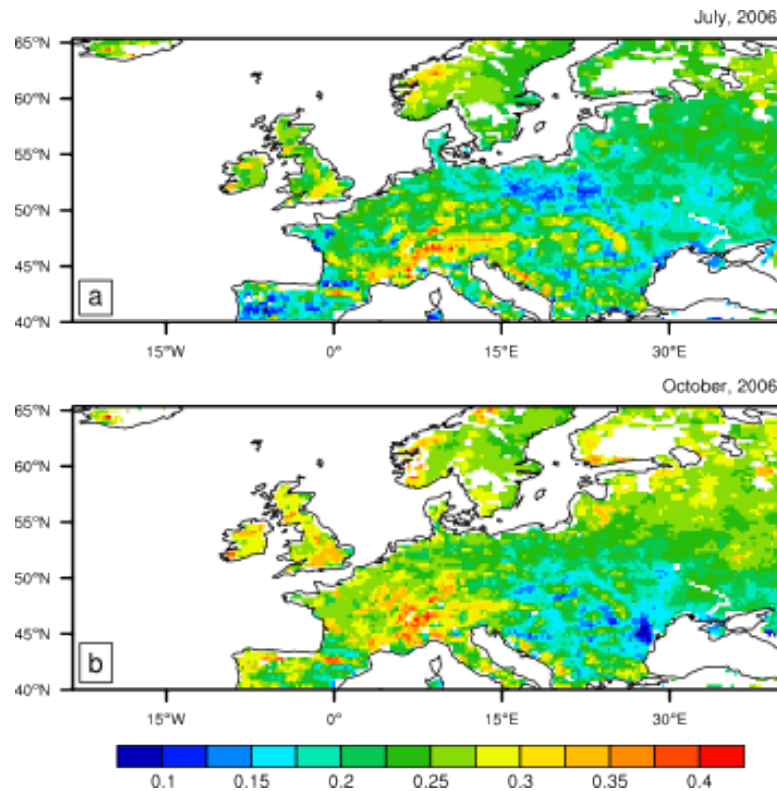
Figure 3.2.1: *Average soil moisture content (-) representative for depths of 0.5–2 cm over Europe 2006 derived by ESA-CCI for (a) July and (b) October. Horisontal resolution is 0.244°.*

is in this thesis used for validation of the NoahMP LSM. The remotely sensed data was generated by merging active and passive microwave observations of soil moisture into a single long-term data set. These measurements may represent soil moisture in the absolute top soil layer down to a depth of 0.5–2 cm. The ESA-CCI soil moisture data is produced with a grid spacing of 0.25° and temporal resolution of about every third or fourth day.

An example of the observed soil moisture content averaged during July and October is shown in Fig. 3.2.1a-b. Only the best quality data is shown and therefore missing pixels are seen in the averages. Comparison of Fig. 3.2.1a to Fig. 3.1.1a shows that the spatial pattern in soil moisture is in good compliance with the spatial pattern in precipitation. For instance, the area over Poland which received very little rain during July is also represented by very low soil moisture content in the top soil layer. Similarly for Fig. 3.2.1b and Fig. 3.1.1b, south-eastern Europe show dry soils due to very little precipitation. These soil moisture measurements cannot replace deep soil observations, however, they can be used as an estimate of how the top soil layer are represented by the land surface models and, in addition, add credibility to precipitation observations.

3.3   MODIS and AVHRR

Satellite images from two sensors aboard polar-orbiting satellites are used to represent land cover and vegetation characteristics in the Noah LSM in this thesis. The sensors are the Advanced Very High Resolution Radiometer (AVHRR) and the Moderate Resolution Imaging Spectroradiometer (MODIS). The AVHRR sensor aboard the NOAA satellites has been collecting data continuously since 1981 using five channels that covers different parts of the electromagnetic spectrum. The highest achievable resolution with AVHRR is 1.1 kilometer, however, the early available measurements were of lower resolution. The MODIS sensor aboard the Terra and Aqua satellites provides 36 spectral bands with different wavelenghts. The highest achievable resolution is 250 meter, but for this thesis only data at 1 km resolution is considered. The Terra satellite was launched in 1999, while Aqua has been available since 2002. The different sensors and methods applied to retrieve various land surface products means that the AVHRR and MODIS products are showing significant differences. For instance, the Normalized Difference Vegetation Index (NDVI) data derived by MODIS is generally higher than in the product of AVHRR. Thus, special treatment of the specific satellite products may be necessary, depending on its purpose.

Noah land surface model

All model simulations carried out in this thesis used the Advanced Research WRF (WRF-ARW) model (Skamarock et al., 2008). It is the successor of the fifth-generation NCAR/Penn State Mesoscale Model (MM5) system, which originally was designed for numerical weather prediction purposes. The WRF model has evolved into a flexible state-of-the-art NWP system that is used for both weather and climate research. It uses a non-hydrostatic, mass-conserving dynamical solver to integrate the compressible Eulerian equations using vertical terrain-following coordinates. It includes one-way and two-way nesting capabilities and allows for grid nudging, which is important for long-term simulations. The physics package includes several options for the six main categories: microphysics, cumulus parameterization, planetary boundary layer, surface physics, radiation and diffusion. The purpose of the surface physics is (1) to provide lower boundary conditions to the atmospheric column and (2) to provide predictions of surface or near-surface variables for public and research interest. Over land, these computations are done by the land surface model and several options are available in WRF. This section only concerns the Noah LSM that was applied in the modeling simulations carried out in Refslund et al. (2013a,b).

The Noah LSM is based on the Oregon State University (OSU) LSM (Mahrt and Pan, 1984, Pan and Mahrt, 1987) but has been extended significantly during the last decade for improved performance (Chen et al., 1996, Koren et al., 1999, Chen and Dudhia, 2001, Ek et al., 2003). Although the model is fairly simple, it shows similar performance to more complex models, such as BATS and SiB, with relatively fewer tuning parameters (Chen and Dudhia, 2001).

The purpose of this chapter is to provide a background and a motivation for the papers in Appendix A and B. This is done through description of how vegetation fraction and phenology enters the surface parameterizations. In addition,

this chapter is connected to the new LSM with multiparamterization options (Noah-MP) in WRF since the Noah LSM was used as its baseline model.

In the following, a short description of the Noah LSM is given with main focus on the parameterizations that depend on the vegetation information. This is followed by a description of how the land surface heterogeneity, vegetation fraction and its phenology are represented in the model. An overview of the WRF-ARW model and short introductions to the various model parameterizations is given in Skamarock et al. (2008).

4.1   Model structure and key equations

4.1.1   Surface energy and water parameterizations

The Noah LSM has a combined ground–vegetation surface and four soil layers extending down to a depth of 2 m with thicknesses of 10, 30, 60 and 100 cm. The surface energy balance (equation 2.1.4) is solved using a linearized Penman-based potential evaporation approach described in Mahrt and Pan (1984), Chen and Dudhia (2001). In the absence of snow cover, the total evapotranspiration is computed as the sum of three contributions: direct soil evaporation (E_s), canopy transpiration (T_r) and evaporation of intercepted water by the canopy (E_c). The direct soil evaporation is parameterized as

$$E_s = (1 - F_v)\beta^2 E_p \tag{4.1.1}$$

where F_v is the green vegetation fraction and β represents a normalized soil moisture availability term

$$\beta = \frac{\Theta - \Theta_w}{\Theta_{ref} - \Theta_w} \tag{4.1.2}$$

where Θ_w represents the wilting point, Θ_{ref} is the field capacity and Θ is the top soil layer volumetric soil moisture content. The maximum possible evaporation that could occur over a water surface given the atmospheric conditions is represented by the potential evaporation E_p. Similarly, E_c is given by

$$E_c = F_v E_p \Big(\frac{W_c}{S}\Big)^{\frac{1}{2}} \tag{4.1.3}$$

where W_c represents the intercepted water content and S indicates the maximum water holding capacity of the canopy, currently set to 0.5 mm. The canopy transpiration is calculated using

$$T_r = F_v E_p P_c \Big[1 - \Big(\frac{W_c}{S}\Big)^{\frac{1}{2}}\Big]. \tag{4.1.4}$$

where P_c represents the plant coefficient which includes the influence of a Jarvis-type formulation (Jarvis, 1976) of the stomatal control (R_c) given by

$$R_c = \frac{R_{c,min}}{\text{LAI}\, F_1 F_2 F_3 F_4} \tag{4.1.5}$$

where $R_{c,min}$ is the minimum canopy resistance and F_1, F_2, F_3 and F_4 represent the effects of solar radiation, vapor pressure deficit, air temperature and rootzone soil moisture, respectively.

The ground heat fluxes are calculated using a diffusion equation where the thermal conductivities are functions of soil texture and soil moisture. The upper boundary condition is described by the skin temperature (T_{sk}) of the combined vegetation-ground surface layer, while an annual mean climatological temperature represents the lower boundary condition. The soil texture is described using the FAO 16-category product at $0.083°$ horisontal resolution (Miller and White, 1998). The skin temperature is derived as a diagnostic quantity of the surface energy balance and is used in equation 2.1.3 as T_{rad} (Chen and Dudhia, 2001). The ground heat flux in the upper soil layer is given by

$$G = K_s \frac{T_{sk} - T_s}{\Delta Z_s} \tag{4.1.6}$$

where T_s represents the upper soil layer temperature, ΔZ_s is the upper soil layer depth and K_s is the thermal conductivity of the upper soil layer. In the presence of vegetation, the thermal conductivity is reduced

$$K_s = K_s e^{-2F_v} \tag{4.1.7}$$

to account for lower heat conductivity through vegetation. The sensible heat flux (H) from the combined ground-vegetation surface is calculated from

$$H = \rho c_p C_h |U| (T_{air} - T_{sk}) \tag{4.1.8}$$

where ρ is the air density, c_p is the specific heat capacity at constant air pressure, C_h is the exchange coefficient, while $|U|$ and T_{air} are the lowest atmospheric model layer wind speed and temperature, respectively.

Common to all atmospheric models is to provide a diagnostic variable about the temperature at the 2-m level. In Noah, this level is easily determined due to the combined ground–vegetation surface. In Noah-MP it is, however, more difficult to define what a 2-m level means since each grid cell include two different surfaces with different heights (section 5.2). The 2-m temperature (T_2) in the Noah LSM is related to the sensible heat flux through

$$T_2 = T_{sk} - \frac{H}{\rho c_p C_{h2} |U|} \tag{4.1.9}$$

where C_{h2} indicates a 2-m exchange coefficient. The exchange coefficients in equations 4.1.8 and 4.1.9 are inputs parameters computed prior to the energy and water balance calculations in the Noah LSM. Equations 4.1.1 through 4.1.7 show the critical role played by vegetation fraction in the calculation of the surface energy balance in Noah. Other properties of the land surface, such as LAI, albedo, emissivity and roughness depend on the representation of the land surface heterogeneity and, in addition, on the seasonality of the vegetation fraction data (described in the following sections). Thus, the exchange coefficients in equations 4.1.8 and 4.1.9 also depend on the representation of vegetation fraction, which result in changes of the surface humidity and 10-m wind speeds.

4.1.2   Soil and snow parameterizations

The soil layer hydrology is computed using Richards equation which includes consideration of diffusion, soil evaporation and transpiration, precipitation (without the intercepted part by vegetation), surface runoff, and base flow runoff (Chen and Dudhia, 2001). Free water drainage is assumed at the bottom of the 2-m soil column and thus ground water processes are not included in Noah. The volumetric soil ice content is predicted as a function of soil temperature, soil moisture content, and soil type (Koren et al., 1999). Snow processes are described in a single snowpack layer with snow density predicted as a function of snow age and temperature. Snow albedo depends on the partial snow cover of a grid cell determined as a function of snow depth (Ek et al., 2003). One of the deficiencies of the Noah LSM is due to the relatively simple parameterization of snow cover which result in too early snowmelt (Barlage et al., 2010).

4.2   Land cover classification

Representation of the land surface heterogeneity was in the very early models based on coarse maps and ground surveys of the land cover (Sertel et al., 2010). Nowadays, global land cover classification (LLC) products are derived from high resolution satelitte images of Normalized Difference Vegetation Index (NDVI). The spatial resolution of these LLC products applied in a weather or climate model determines the maximum possible land surface heterogeneity that can be resolved by the model.

The WRF model defines the land surface properties of a model grid box by its dominant land cover type. Thus, each model grid box is represented as a homogeneous area. This approach is effective in terms of computing time but less suitable for coarse simulations over very heterogene surfaces. As the spatial resolution of the model simulations increases the errors introduced by this type of land surface representation are reduced. Therefore, most parameterizations tend to include heterogeneities implicitly to a certain degree.

The properties of each land cover type are defined in lookup tables. The most important are the number of soil layers included in the rootzone, the minimum stomatal resistance, and the minimum and maximum values of LAI, albedo, emissivity and surface roughness length. While the depth of the rootzone and $R_{c,min}$ are constants, the other properties varies in time depending on the seasonality of the vegetation fraction.

Two LCC products are available for use in WRF with horisontal resolutions of $0.008°$ (~ 1 km). The U.S. Geological Survey (USGS) 24-category LCC product and the International Geosphere Biosphere Program (IGBP) 17-category LLC product (Loveland et al., 2000). The USGS data was derived using NDVI composites from the Advanced Very High Resolution Radiometer (AVHRR) during 1992–1993, while the IGBP LCC data applied NDVI composites from the Moderate Resolution Imaging Spectroradiometer (MODIS) collected during 2001 (Friedl et al., 2002). The MODIS-based LCC product in WRF is extended to either 20 categories by adding three tundra classes or to 21 categories by further adding an inland lake class. An example of the 20-category MODIS LCC data for Europe is shown in figure 4.2.1.

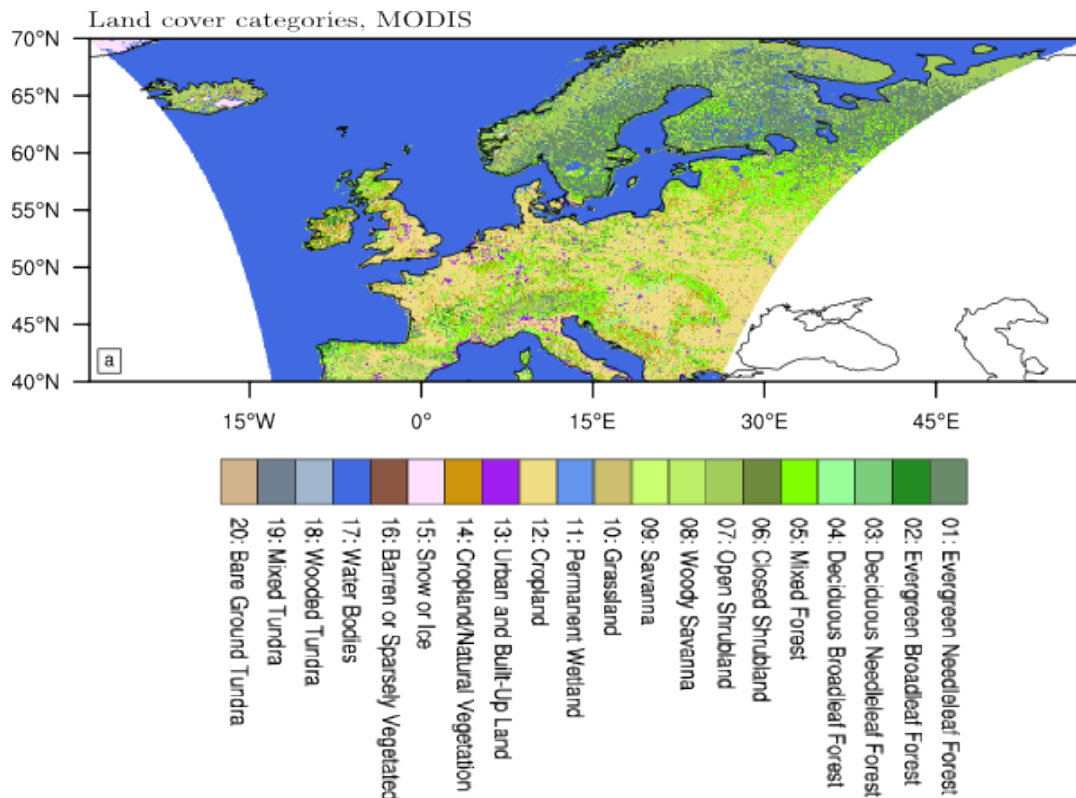The accuracy of the LCC data is important for the performance of the Noah

Figure 4.2.1: *Land cover categories over Europe as represented by the MODIS land cover classification data at horisontal grid spacing of $0.0083° \times 0.0083°$.*

LSM. Any misclassification has the potential to significantly alter the model predictions due to inappropriate assignment of the associated land cover type properties. For example, Sertel et al. (2010) showed how misclassifications (or errors) in the USGS LCC product negatively affected 2-m temperature predictions during a 2004 summer simulation using the Noah LSM. Their study shows the importance of concurrent LCC products to accurately represent the areas that are simulated by the Noah LSM. This favours the use of the MODIS LCC data for simulations representing the surface heterogeity after year 2000. Furthermore, this data plays a major role in the derivation of new MODIS vegetation fraction products, as described in Refslund et al. (2013a).

4.3   Green vegetation fraction

The vegetation fraction and its seasonal development is described by green vegetation fraction in the Noah LSM. It is a prescribed quantity and therefore it does not change according to the model climate. In Noah, it is assumed that other land surface properties such as LAI, albedo, surface emissivity and surface roughness length show similar seasonality as the F_v data, as mentioned in section 4.1.1. Their seasonalities are calculated using a linear interpolation between their respective minimum and maximum values, given in a lookup table, with the interpolation factor (W_F) given by

$$W_F = \frac{F_v - F_{v,min}}{F_{v,max} - F_{v,min}} \tag{4.3.1}$$

where $F_{v,min}$ and $F_{v,max}$ are the annual (climatological) minimum and maximum vegetation fractions within a grid cell.

Figure 4.3.1 shows the potential impacts of a decrease in F_v on predicted soil moisture content in the Noah LSM. The effects on soil moisture are related to changes in both F_v and the scaled land surface parameters. The canopy intercepted water and the soil moisture evaporation (equations 4.1.1 and 4.1.3) are directly affected by a decrease in F_v, which results in either increasing or decreasing soil moisture conditions (Fig. 4.3.1). In rainy conditions, decreased F_v will increase throughfall and increase the soil moisture content, while depletion of upper layer soil moisture content from increased soil evaporation will occur in dry conditions. A decrease in LAI results in less transpiration and consequently to higher soil moisture content, especially in the deeper rootzone. Both F_v and LAI values will contribute to the reduced transpiration, as indicated by equations 4.1.4 and 4.1.5. The impact from increased albedo and decreased surface roughness length, due to decreased F_v, result in similar feedbacks on the soil moisture content. The feedbacks operate through the surface energy balance (equation 2.1.4). Lower sensible and latent heat fluxes at the land surface reduce the moisture and heating of the atmosphere and result in more soil moisture content within the top
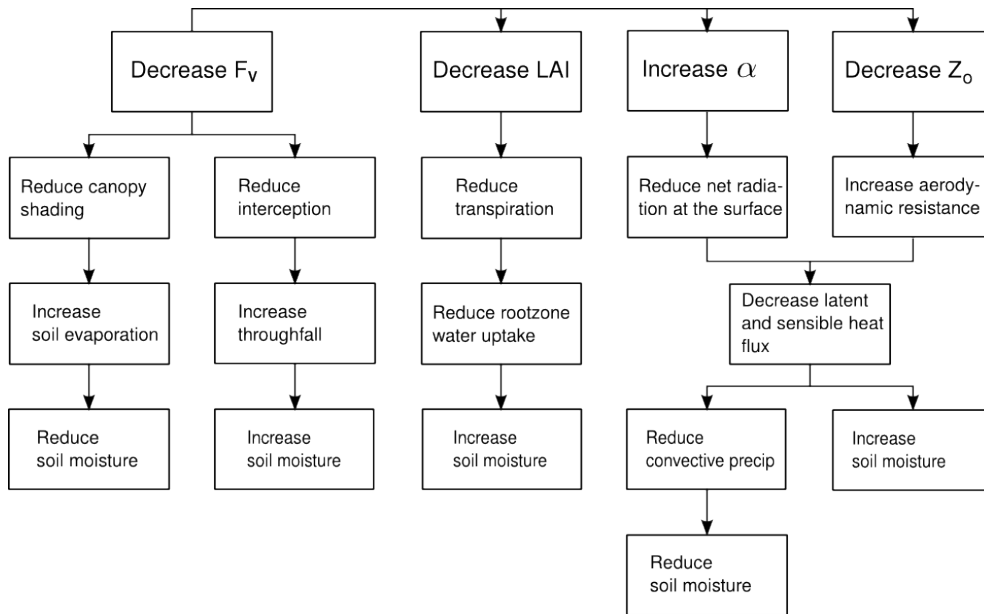
Figure 4.3.1: *Diagram of the impact a decrease in GVF has on the soil moisture content predicted by the Noah LSM.*

soil layer. However, it also lead to less convective rainfall and thereby a reduction of the soil moisture content. A change in emissivity due to F_v will alter both the incomming and outgoing longwave radiation, as indicated in equation 2.1.2, however, its impact is small and it is neglected in Fig. 4.3.1. The diagram illustrates how important the representation of vegetation phenology is in Noah, and how vegetation phenology is linked with multiple energy and moisture feedbacks. The vegetation impacts on soil moisture through equations 4.1.1, 4.1.3 and 4.1.4 can be verified through offline experiments, while feedbacks from albedo and surface roughness length require online or coupled modeling setup.

A change in soil moisture content due to the many feedbacks listed above will result in precipitation feedbacks trough the surface energy balance, Fig. 4.3.2. This effect is large in soil moisture limited regions where the soil moisture control on the surface energy balance are strongest. The latent heat flux is reduced in regions with limited soil moisture conditions, while the sensible heat flux increases. The result in an increase in surface temperature and reduced atmospheric water vapor, which lead to less the convective precipitation. This effect is believed to play a major role in prolonged heat wave conditions (Seneviratne et al., 2010).

4.3.1 AVHRR green vegetation fraction

Until recently (WRF-ARW version 3.5, April 2013), the only F_v product available in the WRF model was a global 5-year monthly climatology derived during 1985–
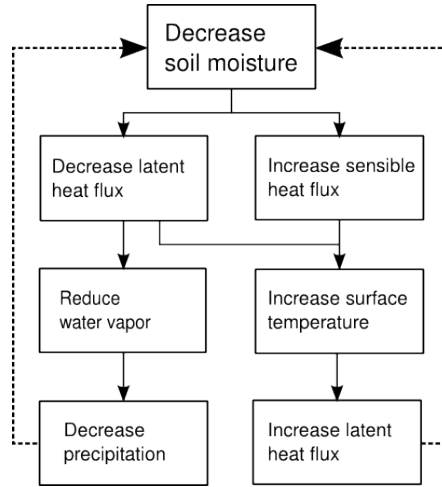
Figure 4.3.2: *Diagram showing the soil moisture impact on surface temperature and precipitation.*

1991 with horisontal resolution of 0.144° (∼ 15 km) (Gutman and Ignatov, 1998). It was produced from weekly composites of AVHRR NDVI satelitte images that were aggregated to monthly values. The NDVI images were subjected to spatial smoothing using a spatial filter (3×3 pixels) for cloud reduction and gap filling purposes (Jiang et al., 2010). A linear NDVI to F_v relationship was assumed given by

$$F_v = \Big(\frac{N - N_s}{N_v - N_s}\Big)^p \tag{4.3.2}$$

with p equal to 1 and where N represents NDVI of the pixel, N_s indicates a bare soil NDVI value and N_v indicates the maximum vegetation NDVI value. Gutman and Ignatov (1998) assumed that N_s and N_v were temporally and spatially global constants with values of 0.04 and 0.52, respectively.

The low spatial resolution of the AVHRR F_v climatology is a significant disadvantage for high resolution modeling, as it blurs the heterogeneity reflected in the LCC products (section 4.2). Furthermore, the effective resolution may be even lower than the proposed (15 km) due to the spatial filtering process (Jiang et al., 2010). The climatological AVHRR F_v data in WRF at 3 km grid spacing for 1 August 2006 over Denmark is shown in figure 4.3.3a, together with the LCC data for Denmark at similar grid spacing in Fig. 4.3.3c. The figure clearly illustrates the inability of the climatological F_v data to represent variations in vegetation fraction between different land cover classes represented in the LCC data. In a small region such as Denmark, the AVHRR F_v seasonalities for different land cover types are almost identical, as noted in Refslund et al. (2013b). In addition, the monthly temporal resolution is not able to represent changes in veg-

etation fraction on weekly or biweekly scale, while representation of interannual variations is impossible using a climatology.

4.3.2 MODIS green vegetation fraction

Several recent studies have investigated the use of high resolution MODIS F_v data in Noah and its impacts on the surface energy balance calculations (Miller et al., 2006, Hong et al., 2009, Lakshmi et al., 2011). The studies applied a new land cover class dependent method (Zeng et al., 2000) that assumes time-varying N_v and N_s using either a linear or a quadratic NDVI to F_v relationship. Furthermore, the maximum vegetation fraction is considered a function of vegetation type. Therefore, the data is dependent on the LCC product applied in the procedure. It requires calculation of histograms to determine the N_v values for each land cover type.

Miller et al. (2006) found large differences between the AVHRR F_v climatology and a MODIS-based F_v product derived using a linear approach. They argued that the seasonality of needleleaf forest and grasslands were improved, while the seasonality for deciduous and mixed forest during winter were degraded. However, they did not attempt to show that the new data improved the skill of the model. Hong et al. (2009) and Lakshmi et al. (2011) applied both the linear and the quadratic method in short-term simulations but they were unable to decide the most suitable method for WRF simulations using in the Noah LSM.

Figure 4.3.3b shows the quadratic MODIS F_v product derived in Refslund et al. (2013a) on the 1 August at 3 km grid spacing over Denmark. The MODIS F_v product is able to separate vegetation phenologies between different landuse classes, e.g. between cropland and mixed forest over Zealand (also shown in (Refslund et al., 2013b)). In addition, this product represents much more variability in the vegetation than the AVHRR F_v product.

4.4 Introduction to Appendix - Paper I

Paper I focuses on a thorough investigation of the use of MODIS-derived green vegetation fraction in connection with the Noah LSM. A detailed description of the method applied in the derivation of the new MODIS F_v products is given. In addition, the MODIS products are evaluated in lower resolution WRF simulations over Europe during year 2006. The performance of the model simulations are evaluated to observations given by the E-OBS gridded data.

The main goals of Paper I were (1) to determine whether MODIS NDVI data should be combined with the linear or the quadratic method to obtain F_v for use in WRF and (2) to develop a flexible method from which climatological and single year F_v data of high spatio-temporal resolution could be derived. It was chosen to avoid noisy satellite retrievals by only using the highest quality data

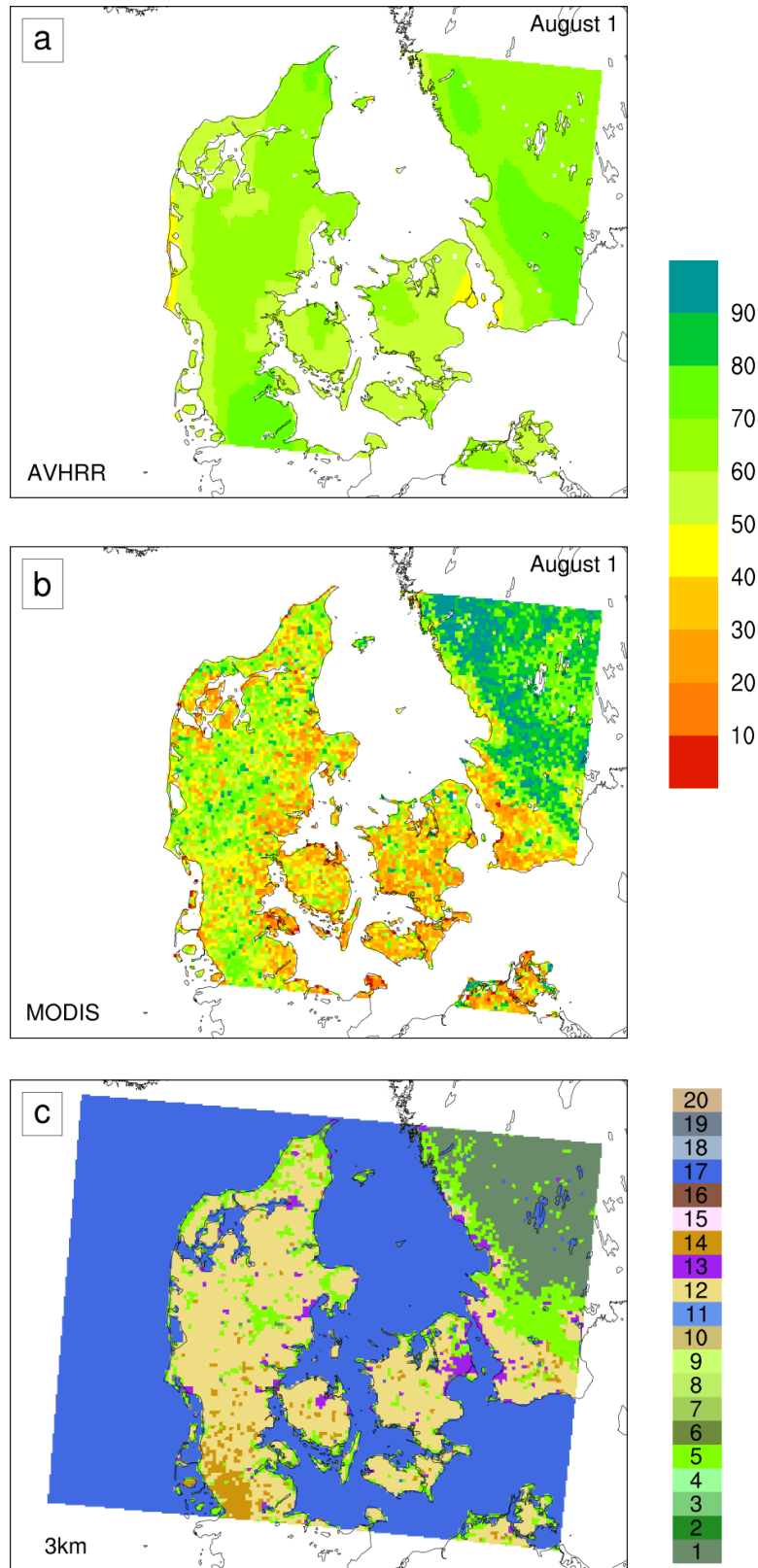**Figure 4.3.3:** *Illustration of the (a) AVHRR F_v climatology and (b) land cover classes represented in a WRF simulation at 3 km grid spacing on August 1. The land cover classes corresponds to the 20-category MODIS LCC shown in figure 4.2.1.*

and using the method outlined in Zeng et al. (2000) to derived the F_v products. A combination of existing and novel data processing techniques were applied to create a multi-year NDVI climatology with a spatial resolution of 0.0083° (~ 1 km) and 8-days temporal sampling. The advantage of the multi-year NDVI climatology is twofold. First, it allows for gap filling of missing data in during single year NDVI data extractions using the climatological trends at each pixel. Second, it can be used in a near real-time product for the benefit of the real-time weather forecasting at DTU Wind Energy.

4.5 Introduction to Appendix - Paper II

Paper II evaluates the performances of the quadratic MODIS F_v product and the AVHRR F_v climatology in high resolution, seasonal WRF simulations down to cloud-resolving scales. The study compared modeling results to gridded observational data of precipitation, surface temperature, wind speed and soil moisture and, in addition, to hourly station measurements of temperature, wind speed and Bowen ratio. The aims of the study were (1) to investigate the influence of spatial resolution on simulated precipitation due to parametrized and resolved convection and (2) to investigate the effects of concurrent vegetation data in WRF-Noah simulations. The gridded observational datasets were represented by the DMI data. The station data was obtained from the DMI network of measurement stations.

CHAPTER 5

Noah-MP

This chapter presents the work done on coupling, debugging and evaluating the performance of the recently developed Noah land surface model with Multi-parameterization Options (Noah-MP, Niu et al 2011) within the WRF modeling framework. The work was carried out at NCAR with the main focus directed towards the surface energy balance calculations, although significant amounts of time were spend on the water balance calculations as well. The many tasks turned out to be more time consuming than initially expected due to the many available options in Noah-MP. New options were added for better representation of vegetation fraction and calculation of exchange coefficients, while several errors were corrected. For example, the initial 2 meter temperature calculations resulted in unrealistically low values ($\sim 200K$) and the urban category had a too permeable surface. In addition, the work included rearrangement of the WRF modeling structure to allow coupling of future sea-ice models. The following sections seek to (1) give an overview of the model implementations and options in the original model and those added, (2) present how the surface energy balance are solved and (3) present a model evaluation of the most common meteorological surface variables.

Thorough investigation of the performance of Noah-MP coupled to WRF has not been documented so far in the literature. This is a huge task which requires careful planning, nearly unlimited computer ressources and a lot of patience. The number of options in Noah-MP result in several thousands of combinations available for testing. The model evaluation presented below is limited to a summer simulation over Denmark 2006, which coincides with the period studied in the paper in Appendix A, using the recommended options in Noah-MP. The performance of the recommended options in Noah-MP can be used as a basis for future ensemble investigations of the Noah-MP model. The simulation is compared to

a similar simulation using the Noah LSM using the default F_v climatological and verified against observational gridded data of precipitation, soil moisture and temperature.

New features and options available in Noah-MP are briefly presented in Section 5.1. This is followed by a more detailed description of the energy balance calculations in section 5.2. The modeling setup and validation data are described in section 5.3, while the results are presented in section 5.4. Finally, a short discussion and a conclusion is given in section 5.5.

5.1   Background

The motivation behind the development of Noah-MP was to allow for ensemble representations of land surface processes in a single LSM. The ensemble approach has been supported by several studies; Project for Intercomparison of Land Surface Parameterization Schemes (PILPS) and the Global Soil Wetness Project (GSWP) (Guo and Dirmeyer, 2006, Dirmeyer et al., 2006), showing that multimodel averages generally result in better behavior than single model parameterizations. Furthermore, the ensemble structure permits easier detection of optimal parameterization settings for various research applications and possible identification of the controlling processes between the land surface and the atmosphere (Niu et al., 2011).

Niu et al. (2011) chose to use the Noah LSM model as the baseline model for developing the a new LSM with ensemble possibilities. The Noah LSM do not itself facilitate ensemble simulations since only one parameterization is available for each physical process. Several deficiences and limitations of the Noah LSM were identifiedand advanced parameterizations with similar complexity were implemented to facilitate the ensemble methodology of the new Noah-MP LSM. The performance of Noah-MP was evaluated at various observational sites and compared to the performance of the Noah LSM in offline settings (Niu et al., 2011, Yang et al., 2011). Offline simulations only allow one-way interactions using a prescribed meteorology, while online (or coupled) simulations allow two-way interactions such that the LSM impact the atmospheric conditions. A summer dry-down experiment during June 1987 showed large improvements in the simulation of sensible, latent and ground heat fluxes over grasslands compared to the Noah LSM. In addition, the soil moisture content down to a depth of 1 m was significantly better predicted by Noah-MP, showing much wetter soils, compared to Noah. In a winter case study, Noah-MP showed excellent performance in simulating snow surface albedo, depth and mass, while poor performance was shown by Noah. The offline results indicated the great potential of Noah-MP for improving the model predictions when coupled to WRF.

Table 5.1.1: *New features to the Noah-MP model to circumvent deficiencies of the baseline model.*

Vegetation canopy layer	e.g. Bonan (2008)
Two-stream radiation scheme	Dickinson (1983), Niu and Yang (2004)
Ball-Berry stomatal resistance	Ball et al. (1987), Collatz et al. (1992)
Dynamic vegetation model	Dickinson et al. (1998), Yang and Friedl (2003)
Three-layer snow model	Yang and Friedl (2003)
Groundwater and runoff	Niu et al. (2005, 2007)
Frozen soil scheme	Niu and Yang (2006)

5.1.1 Options in Noah-MP

Table 5.1.1 indicates the new features that were introduced in Noah-MP to alleviate some of the shortcomings of the Noah LSM. The most profound change is the introduction of a vegetation canopy layer to replace the mixed ground–vegetation layer used in the Noah LSM. It allows for the calculation of seperate vegetation canopy and ground temperatures, introduction of a short-term dynamic vegetation model and complex calculation of radiation transfer using a two-stream radiation scheme. Furthermore, it permits the carbon budget to be introduced into the WRF modeling framework, which is important for climate change studies. However, the structural change prevents a configuration of Noah-MP that exactly match the configuration of the original Noah LSM, which would simplify parameterization evaluation. The complexity of the hydrology in Noah-MP is also enhanced by e.g. adding an unlimited aquifer below the soil column to simulate groundwater exhanges and a three layer snow model. The many options are briefly described below with the recommended options listed in Table 5.1.2.Below the 2 m bottom of the

Vegetation coverage and phenology − 4 options

Two options were implemented by Niu et al. (2011) to represent vegetation coverage and phenology. The first option assumes time-varying vegetation fractions, using the climatological F_v data in WRF, combined with monthly varying leaf and stem area indexes (LAI and SAI) defined in a lookup table. This option is very similar to the method applied in the Noah LSM. The second and most advanced option uses a dynamic vegetation model (DVM) to predict vegetation phenology. It describes the carbon budgets by accounting for photosynthesis, respiration, and carbon allocation in vegetation (leaf, wood and roots) and soils to predict LAI and SAI (Dickinson et al., 1998, Yang and Friedl, 2003). The predicted total vegetation area index (VAI) is converted into vegetation fraction

using

$$F_v = 1 - e^{-0.52\text{VAI}} \qquad (5.1.1)$$

where VAI=LAI+SAI. Only the development of the dominant vegetation class within a grid cell is predicted by the DVM. The carbon budgets are not computed when the DVM option turned off (Niu et al., 2011).

We added two additional options to the coupled version of Noah-MP. The third option combines equation 5.1.1 with table values of LAI and SAI to represent monthly varying vegetation phenology. In the fourth option, I assumed annually constant F_v and combined it with the time-varying LAI and SAI values from the lookup table. The constant vegetation fraction is derived as the annual maximum F_v in the climatological F_v data.

A fifth option in Noah-MP is proposed here. It should allow the use of satelitte derived LAI and SAI combined with the constant vegetation fraction introduced in option four. This approach is currently not possible with Noah-MP but will be a simple addition since the WRF modeling framework already allows for easy ingestion of satellit LAI.

Canopy geometry for radiation - 3 options

Radiation transfer through the vegetation canopy is implemented with three options that assume different vegetation distributions. First option introduces between-canopy and within-canopy gap probabilities in the vegetation layer by collecting leaves into canopy crowns. The crowns are assumed evenly distributed and are functions of vegetation type, height and density, defined in a lookup table, and solar angle. A constant gap probability is assumed for scattered (diffuse) light (refer section 5.2). The second option assumes a cloud of leafs with a gap probability equal to zero for both direct and diffuse light, while a gap probability equal to the non-vegetation fraction $(1 - F_v)$ is assumed in the third option. No options were added, although different parameterizations were investigated.

Stomatal resistance - 2 options

A Ball-Berry type stomatal resistance and photosynthesis model (Ball et al., 1987, Collatz et al., 1992) was implemented as the first option. The second option is the Jarvis type stomatal resistance calculation also used in the Noah LSM (Chen et al., 1996). The Ball-Berry model must be used in connection with the dynamic vegetation model. A detailed description of the Ball-Berry stomatal resistance calculations is given in Niu et al. (2011). No additional options added.

Soil moisture factor for stomatal resistance - 3 options

Three options are available to calculate the soil moisture stress factor (β factor) that influences vegetation transpiration. The first option parametrizes the β fac-

tor as a function of soil moisture and is identical to the method used in the Noah LSM (Chen et al., 1996). The remaining two options use matric potentials as function of soil type but with different functional behavior. A detailed comparison of the three options is shown in Niu et al. (2011) (see Fig. 3 therein). No options added.

Surface layer exchange coefficients - 4 options

The calculation of exchange coefficients over land in Noah-MP changes the structure of the WRF model, as illustrated in Figure 5.1.1. The purpose of the atmospheric surface layer (ASL) schemes in the Noah LSM is to provide surface fluxes over water to the PBL scheme and exchange coefficients to the LSM, which are necessary for the calculation of the land surface fluxes. However, the ASL–LSM coupling is removed using Noah-MP since the land surface exchange coefficients are calculated within the Noah-MP energy balance routine. Thus, the ASL effectively turns into a water surface layer scheme when using Noah-MP, which allows an easier coupling of ocean models to WRF in the future. This modeling structure follows the recommendations proposed in Polcher et al. (1998).

Niu et al. (2011) implemented two options for the calculation of land surface exchange coefficients for momentum and heat based on Monin-Obukhov theory. The two methods use the same stability functions for stable and unstable conditions (Paulson functions, see Chen et al. (1997)). The first option includes the zero-plane displacement height in its formulation and assumes equal surface roughness lengths for heat and momentum (z_{0h} and z_{0m}). The second option uses $z_{0h} = z_{0m} \exp(-\kappa C \sqrt{Re})$ but neglects the zero-plane displacement height to derive the exchange coefficients.

I added two new options to calculate exchange coefficients when using the MYJ and YSU PBL schemes in Noah-MP. The third option is similar to the land surface calculations in the Eta ASL scheme in the Noah LSM (Janjic, 1996), while the fourth option is similar to the calculation done in the YSU ASL scheme (Skamarock et al., 2008).

Runoff and groundwater - 4 options

Four options are available for runoff and groundwater calculations. The first and second options are based on the TOPMODEL runoff scheme using either a simple groundwater parameterization or a equilibrium water table parameterization (Niu et al., 2005, 2007). The third option is similar to the surface and subsurface runoff schemes used in the Noah LSM (Schaake et al., 1996), while the fourth option uses the BATS runoff schemes (refer Niu et al. (2011)). No new options added.
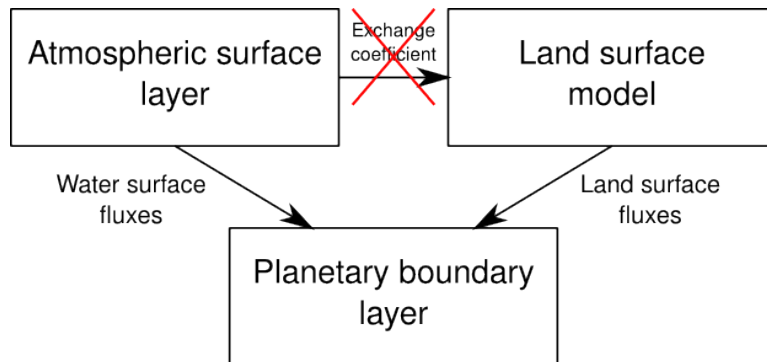
Figure 5.1.1: *Illustration of the structural change between the atmospheric surface layer, the land surface model and the planetary boundary layer scheme when using Noah-MP (with red cross) compared to the Noah LSM (without red cross).*

Rain and snow partitioning - 3 options

Three options are implemented to describe the partitioning of rainfall and snowfall at air temperatures (T_{air}) close to freezing (T_{frz}). The first option assumes that all precipitation is snow when $T_{air} < T_{frz}+0.5$K and rain when $T_{air} > T_{frz}+2.5$K. At temperatures within the range of these extremes, the snow fraction is either 0.6 or linearly increasing towards a snow fraction of 1.0. The second option represents all precipitation as snow when $T_{air} < T_{frz} + 2.2$K, while the third option represents all precipitation as snow when $T_{air} < T_{frz}$. The latter option is similar to the parameterization in the Noah LSM. No new options added.

Snow surface albedo - 2 options

Two options are available for calculating snow surface albedos. The first option (from the BATS scheme) accounts for fresh snow albedo, snow age, solar zenith angle, grain size growth, dirt on snow and distinguish between visible and near-infrared wave bands (Dickinson et al., 1993). The second option (from the CLASS scheme) accounts for fresh snow albedo and snow age but does not distinquish between different wavebands (Verseghy, 1991). The second option is closest to the parameterization used in the Noah LSM. The BATS scheme generally produces higher snow surface albedos compared to the CLASS scheme but include tunable parameters to provide better estimates (Niu et al., 2011). No new options added.

Frozen soil liquid water - 2 options

Two options applies to supercooled liquid water (or ice fraction) in the frozen soil. The first option is described in detail in Niu and Yang (2006), while the second option is similar to the approach used in the Noah LSM (Koren et al., 1999). No new options added.

Frozen soil permeability - 2 options

Two options applies to calculate the frozen soil permeability. As in the case of supercooled liquid water, the first option is described in detail in Niu and Yang (2006), while the second option is similar to the approach used in the Noah LSM (Koren et al., 1999). No new options added.

Soil temperature boundary condition - 2 options

The first option assumes zero heat flux at the bottom of the soil column, while the second option use the approach in the Noah LSM, mentioned in **??**, using an annual mean temperature to describe the bottom soil temperature. No new options added.

Snow/soil temperature time scheme - 2 options

Finally, two options are available for adjustment of the snow and soil temperatures. First option uses a semi-implicit time scheme, while the second option uses a fully-implicit time scheme as in the Noah LSM (Skamarock et al., 2008). No new option added.

Table 5.1.2: *The recommended options in Noah-MP are based on considerations of complexity and initial testing. These were proposed by the land surface group at NCAR.*

| Parameterization	Option	Recommended
Vegetation coverage and phenology	dveg	4
Canopy geometry for radiation	opt_rad	1
Stomatal resistance	opt_crs	1
Soil moisture factor for stomatal resistance	opt_btr	1
Surface layer exchange coefficient	opt_sfc	1
Runoff and groundwater	opt_run	1
Rain and snow partitioning	opt_snf	1
Snow surface albedo	opt_alb	2
Supercooled liquid water	opt_frz	1
Frozen soil permeability	opt_inf	1
Soil temperature boundary condition	opt_tbot	2
Snow/soil temperature time scheme	opt_stc	1
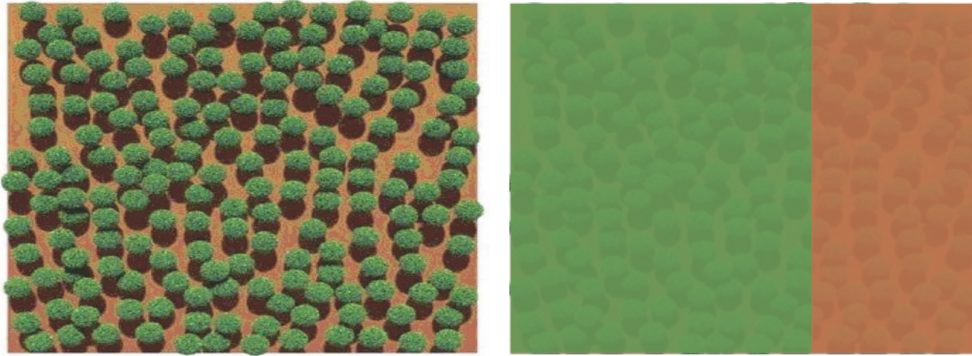
Figure 5.2.1: *Illustration of the approaches applied for calculation of radiation transfer (left) and turbulent transfer (right) within a grid cell.*

5.2   Surface energy balance

This section presents the surface energy balance methodology used in Noah-MP. Due to the many new implementations and the structural change, this approach is very different from the method applied in the Noah LSM, as presented in section 4.1.1. The main part of my work on Noah-MP was devoted to the parameterizations within the energy balance calculations.

The surface energy balance in Noah-MP is solved using a "semitile" subgrid method to deal with radiative and turbulent transfers between the ground, the vegetation and the atmosphere. Shortwave radiative transfer is calculated over an entire grid cell, represented on the left hand-side of figure 5.2.1, while calculation of longwave radiation, latent heat, sensible heat and ground heat fluxes use a tiled approach with a vegetated (green) and a non-vegetated (brown) tile, indicated on the right hand-side of the figure.

Shortwave radiation: The shortwave radiative budget is calculated using a two-stream radiation scheme that accounts for scattering and multiple reflections in two wavebands: visible and near-infrared (Dickinson, 1983, Sellers, 1985). An illustration of the shortwave radiation budget for a direct and a diffuse beam is given in figure 5.2.2. The letter B indicates a unit beam of solar radiation with the subscripts 'd' and 'i' representing direct or diffuse light, respectively. F_{av} represents the absorbed fraction of solar radiation by vegetation, while F_{td} and F_{ti} represent the direct and diffuse transmitted fractions. The reflected part of a beam that initially hits the vegetation, is represented by F_{rvg}, while F_{rg} indicates the reflected part of a beam incident on the ground. The ground albedos (α) are derived as function of soil color (currently same color for all soil types), soil moisture and snow albedo (see section 5.1.1). The gap probability (P_g) for the direct beam depends on the solar angle and the canopy crown structure, while
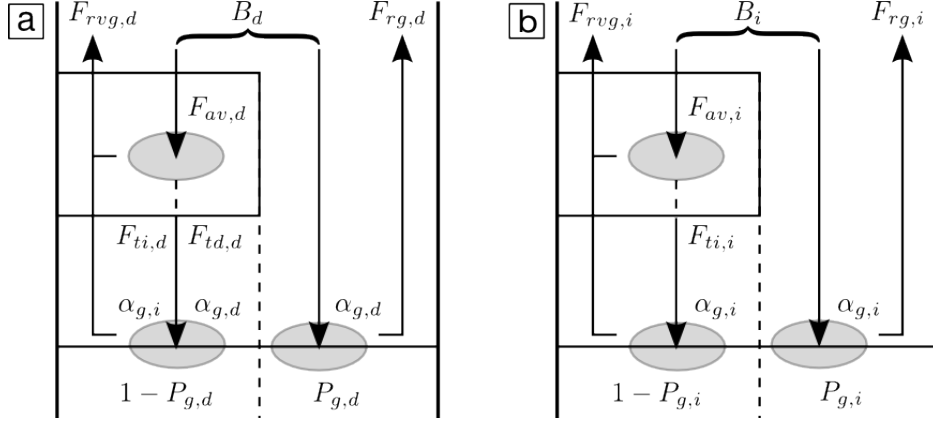
Figure 5.2.2: *Schematic of the modified shortwave radiation transfer for (a) a direct beam and (b) a diffuse beam.*

for a diffuse beam is assumed constant ($P_g = 0.05$). The resulting absorbed shortwave radiation by vegetation (S_{av}) and ground (S_{ag}) can be written as

$$S_{av} = F_{av,d}S_d + F_{av,i}S_i \tag{5.2.1}$$

$$S_{ag} = \Big[(1 - P_{g,d})\big[F_{td,d}(1 - \alpha_d) + F_{ti,d}(1 - \alpha_i)\big] + P_{g,d}(1 - \alpha_d)\Big]S_d$$
$$+ \Big[[F_{ti,i}(1 - P_{g,i}) + P_{g,i}](1 - \alpha_i)\Big]S_i \tag{5.2.2}$$

where S_d and S_i are the total incoming direct and diffuse shortwave radiation, respectively. The total reflected shortwave radiation over a grid cell is converted to a grid cell surface albedo by dividing with the incoming shortwave radiation over that particular grid box.

Iterative process: The vegetation-absorbed and ground-absorbed shortwave radiation (equation 5.2.1 and 5.2.2) must be balanced by the net absorbed long-wave radiation (L), latent heat flux (LH), sensible heat flux (H) and ground heat flux (G) over the vegetated and non-vegetated tiles. These energy balances are derived using an iterative process that solves for the unknown temperatures within each tile. The energy balances over a vegetated tile are therefore given by

$$S_{av} = F_v[L_{av}(T_v, T_{g,v}) + LH_v(T_v, T_{g,v}) + H_v(T_v, T_{g,v})] \tag{5.2.3}$$

$$S_{ag}F_v = F_v[L_{ag}(T_v, T_{g,v}) + LH_g(T_v, T_{g,v}) + H_g(T_v, T_{g,v}) + G(T_{g,v})] \tag{5.2.4}$$

where F_v represents the vegetation fraction, while T_v and $T_{g,v}$ represent vegetation and ground temperatures, respectively. The energy balance over the non-vegetated tile is represented similarly to equation 5.2.4 using T_g instead of T_v and $T_{g,v}$ and changing F_v to the non-vegetated fraction. The iterative process
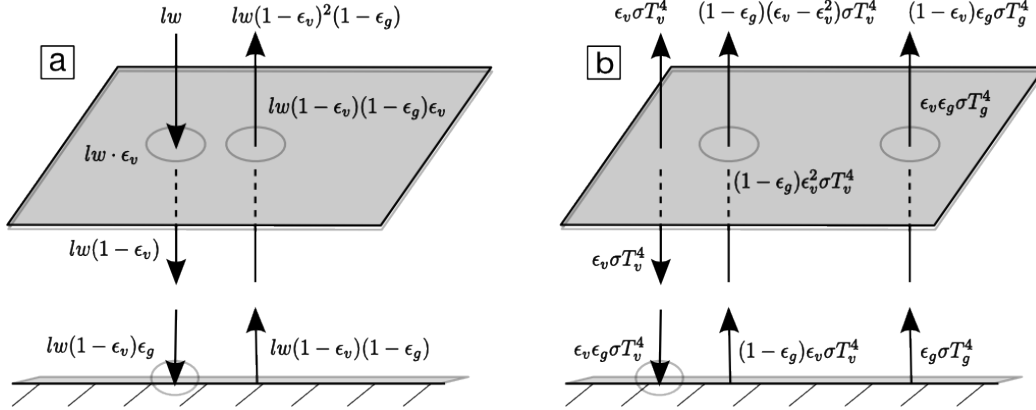
Figure 5.2.3: *Schematic of (a) downwelling longwave radiation budget and (b) long-wave raditation budget due to radiant emittance from vegetation and ground over a vegetated fraction. The absorbed portions of the radiation are indicated by grey circles.*

is suspended as the energy balances are achieved, or if the maximum number of iterations have been carried out. I increased the maximum number of iterations significantly in the coupled version of Noah-MP to ensure that the desired energy balance threshold was obtained in most cases.

Longwave raditation: The longwave radiation tranfer budgets over a vege-tated tile are represented in Fig. 5.2.3 for (a) the downward longwave radiation (lw) and (b) the longwave radiant emittance. The radiation budgets depend on the emissivity of the vegetation (ϵ_v) and the emissivity of the ground (ϵ_g). The ground emissivity is assumed constant while ϵ_v depends on the vegetation area index

$$\epsilon_v = 1 - e^{-\text{VAI}}. \tag{5.2.5}$$

The net absorbed longwave radiation for the vegetation layer (equation 5.2.3) is given by (positive to the atmosphere)

$$\begin{aligned} L_{av} = & - \epsilon_v[1. + (1. - \epsilon_v)(1. - \epsilon_g)]lw \\ & - \epsilon_v\epsilon_g\sigma_b{T^4}_g + (2. - \epsilon_v(1. - \epsilon_g))\epsilon_v\sigma_b{T^4}_v \end{aligned} \tag{5.2.6}$$

while the net absorbed longwave radiation (positive to the atmosphere) at the ground below the canopy (equation 5.2.4) is given by

$$L_{ag} = -\epsilon_g(1. - \epsilon_v)lw - \epsilon_g\epsilon_v\sigma_b{T^4}_v + \epsilon_g\sigma_b T_g^4. \tag{5.2.7}$$

Heat fluxes: Calculation of the sensible, latent and ground heat fluxes over a vegetated tile, to fullfil the surface energy balances in equation 5.2.3 and 5.2.4, follows the approach outlined in Bonan (2008). The following paragraph shows
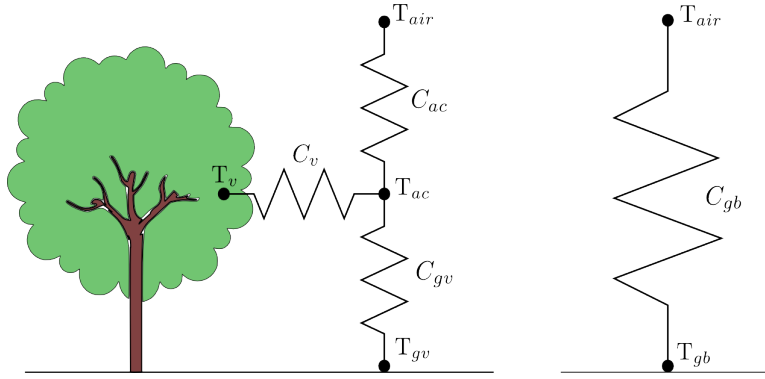
Figure 5.2.4: *Illustration of the sensible heat fluxes over a vegetated and non-vegetated area in a grid cell represented by a single vegetation layer.*

how the sensible heat fluxes are obtained, while the derivation of latent and ground heat fluxes are neglected since similar approaches apply. Figure 5.2.4 shows the sensible heat fluxes over a vegetated and a non-vegetated tile in a grid cell. The sensible heat flux from the canopy air (subscript ac) to the atmosphere (H_{air}) must equal the sensible heat fluxes to the canopy air from the vegetation canopy and the ground surface ($H_v + H_g$), since heat storage in the canopy air is neglected. These fluxes are given by

$$H_x = \rho c_p C_x |U|(T_x - T_{ac}).\tag{5.2.8}$$

where x represents either vegetation (v) or ground (g), ρ is the air density, c_p is the heat capacity for dry air and C represents the exchange coefficient for heat. The canopy air space temperature (T_{ac}) is estimated using a linear weighted function of the surrounding temperatures and exchange coefficients, given by

$$T_{ac} = \frac{C_{gv}T_{gv} + C_v T_v + C_{ac}T_{air}}{C_{gv} + C_v + C_{ac}}\tag{5.2.9}$$

where initial guesses of T_{gv} and T_v are hardcoded to reflect summer and winter values, while T_{air} represents the lowest atmospheric model layer temperature. The sensible heat flux to the atmosphere over a vegetated tile ($H_{v,air}$) is thus given by

$$H_{v,air} = \rho c_p C_{ac} |U|(T_{ac} - T_{air})\tag{5.2.10}$$

while the sensible heat flux over a non-vegetated tile is derived by changing C_{ac} and T_{ac} with the corresponding exchange coefficient and temperature of the non-vegetated ground.

2-m temperature: Appropriate 2-m temperatures for the vegetation and ground surfaces are calculated at the end of the final iteration. These calculations depend on the method used to calculate the exchange coefficients. The methods
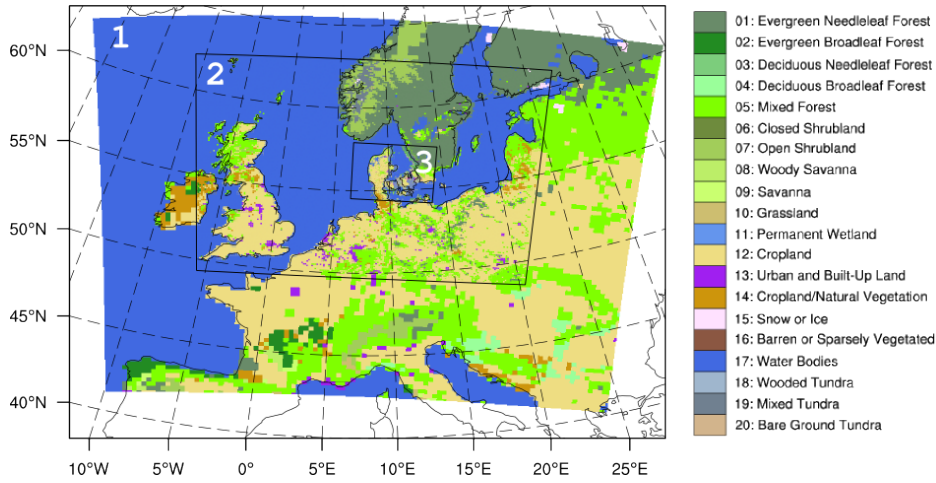
Figure 5.3.1: *Domain configuration for the simulations with Noah-MP using grid spacing in domain (1) 27 km, (2) 9 km and (3) 3 km.*

implemented by Niu et al. (2011) are derived from

$$T_{2x} = T_x - \frac{H_{x,air}}{\rho c_p} \frac{\left[\log(2 + z_{0h})/z_{0h} \right]}{u_{*,x}\kappa} \tag{5.2.11}$$

where x represents either vegetation (v) or ground (g), $u_{*,x}$ is the friction velocity over the specific surface, κ is the von Karman constant and z_{0h} is the roughness length for heat. The new options for the YSU and MYJ PBL schemes use similar approach as represented in equation 4.1.9. The final 2-m temperature output in Noah-MP is defined as the average over the vegetated and non-vegetated tiles. Several other approaches to derive an effective 2-m temperature of a grid cell were tested but eventually we decided that the simple averaging method was the best option.

5.3   Model configuration and validation data

We used the WRF model version 3.4 (Skamarock et al., 2008) to carry out high resolution simulations over Denmark for the summer of 2006. The modeling configuration is shown in Figure 5.3.1 using grid spacings of 27 km, 9 km and 3 km in domain 1, 2 and 3, respectively. The selected physical parameterizations are shown in Table 5.3.1. The initial and lateral boundary conditions were provided by the 6-hourly Climate Forecast System Reanalysis (CFSR) data at 0.5° (Saha et al., 2010), while the sea surface temperatures were described by 1/12° daily sea surface temperatures (Gemmill et al., 2007). Grid nudging is applied exclusively in the outermost domain above the 10 lowest model levels for temperature, humidity and wind speed. Nudging, however, is not allowed within the PBL for

temperature and humidity. The model configuration is similar to the configuration used by Refslund et al. (2013b) to compare the Noah-MP simulations to control simulations using the Noah LSM with the AVHRR F_v climatology. The control simulations carried out in Refslund et al. (2013b) were named C9 and C3 for the 9 km and 3 km domains, respectively. However, in the following they are renamed to N9 and N3 to represent the Noah LSM. Results from the Noah-MP simulations using 9 km and 3 km grid spacings are referred to as NMP9 and NMP3, respectively. The Noah-MP initial soil moisture conditions was derived from the control simulations starting on the 1 of May 2006. The simulations ended on the 1 of September 2006. The month of May is considered as a spinup period and therefore excluded from the comparison, except for soil moisture in the top soil layer.

Table 5.3.1: *Physical parameterization schemes used in the simulations. *Only used in 27 km and 9 km resolutions.*

Parameterization	Reference
Noah-MP LSM	Niu et al. (2011)
MYJ PBL	Janjic (2002)
Eta surface layer	Janjic (1996)
WSM5 microphysics	Hong et al. (2004)
RRTM longwave radiation	Mlawer et al. (1997)
Dudhia shortwave radiation	Dudhia (1989)
Kain-Fritsch convection*	Kain (2004)

We adopt the approach used in Refslund et al. (2013b) for evaluation of the model performances. This include use of the high-quality gridded data produced by the Danish Meteorological Institute and the soil moisture product from the European Space Agency – Climate Change Initiative. Regridding of the simulations was carried out using the ESMF regridding software. For detailed descriptions of the modeling setup, the validation data and the applied software, refer Refslund et al. (2013b).

5.4 Results

5.4.1 Precipitation and soil moisture

Figure 5.4.1 shows the June, July and August (JJA) accumulated precipitation over Denmark during 2006 for the gridded DMI observations and the control simulations (N3 and N9) and Noah-MP (NMP3 and NMP9). Comparison of the
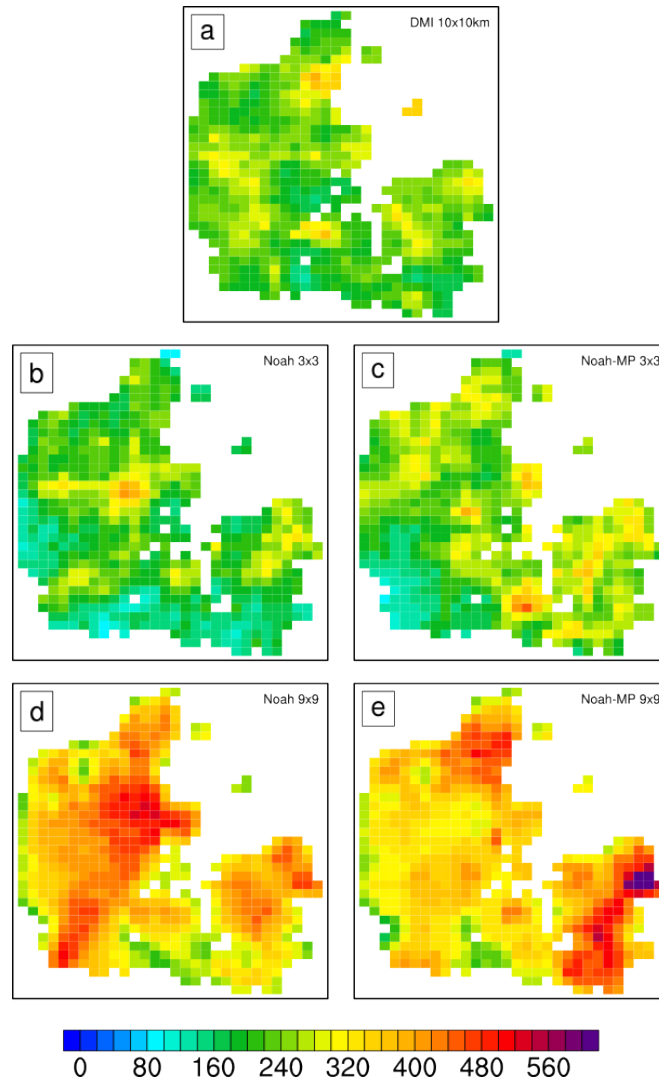
Figure 5.4.1: *Accumulated precipitation (mm) during June, July and August for (a) observations, (b) N3, (c) NMP3, (d) N9 and (e) NMP9.*

low resolution simulations (N9 and NMP9) shows that the horisontal distribution of rainfall is very different (Fig. 5.4.1d-e). They both overestimate precipitation compared to the observations, as expected from Refslund et al. (2013b). However, while NMP9 significantly overestimates precipitation over the eastern parts of Denmark, the western parts are greatly overestimated by N9. The high resolution simulations (Fig. 5.4.1b-c) show better agreement to the observations, although the south-western areas are underestimated. The rainfall patterns follow their parent domain such that NMP3 shows larger precipitation amounts over the eastern areas, while N3 shows larger amounts over the western parts.

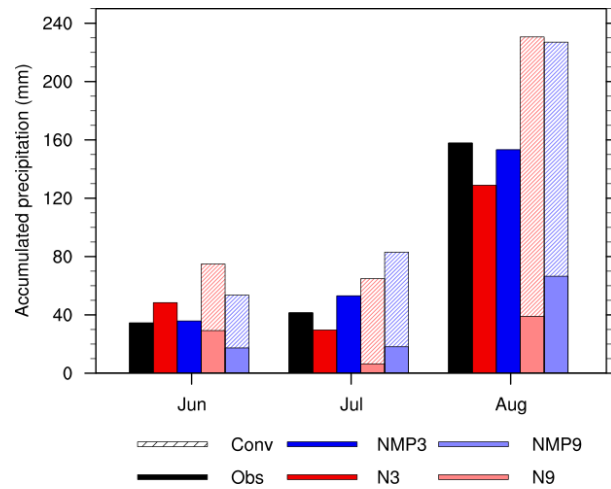The monthly average accumulated precipitation during JJA over Denmark

Figure 5.4.2: *Monthly accumulated precipitation (mm) averaged over Denmark during June, July and August for the DMI observations and Noah and Noah-MP simulations.*

is shown in Fig. 5.4.2. NMP3 shows better agreement with the observations than N3, especially during June and August. The observed average accumulated precipitation during JJA is 235 mm while N3 and NMP3 predict 207 mm and 242 mm, respectively. Thus, N3 underpredict precipitation with 0.3 mm per day, while NMP3 overpredicts precipitation with only 0.08 mm. The average monthly accumulation for N9 and NMP9 totals 371 mm and 364 mm, respectively, which corresponds to overestimations of 1.5 mm and 1.4 mm per day. NMP9 shows the best performance during June compared to N9, while the opposite occur during July.

The predicted soil moisture content of the upper soil layer during May, June, July and August is compared to the observed quantities derived from the ESA-CCI soil moisture data, shown in Fig 5.4.3a. The soil moisture field started too wet in all simulations suggesting that better soil moisture initialization should have been used. Similar soil moisture overestimations during May and June are shown by N3, NMP3 and NMP9, while higher values are obtained in N9. Good agreement to the observed quantity in July is shown by NMP3 while underestimation of soil moisture is found using N3. In August, the better agreement to observations is obtained using N3, while a slight overestimation is produced by NMP3. The low resolution simulations overestimates the soil moisture content in both July and August. Figure 5.4.3b shows the soil moisture content during JJA down to a depth of 1 m for the model simulations. The low resolution simulations show only minor differences during JJA, while large differences in soil moisture content are found between N3 and NMP3, with significantly drier soil moisture conditions in the N3 simulation. A clear difference in soil moisture content between Noah and Noah-MP was also observed during the dry-down experiment
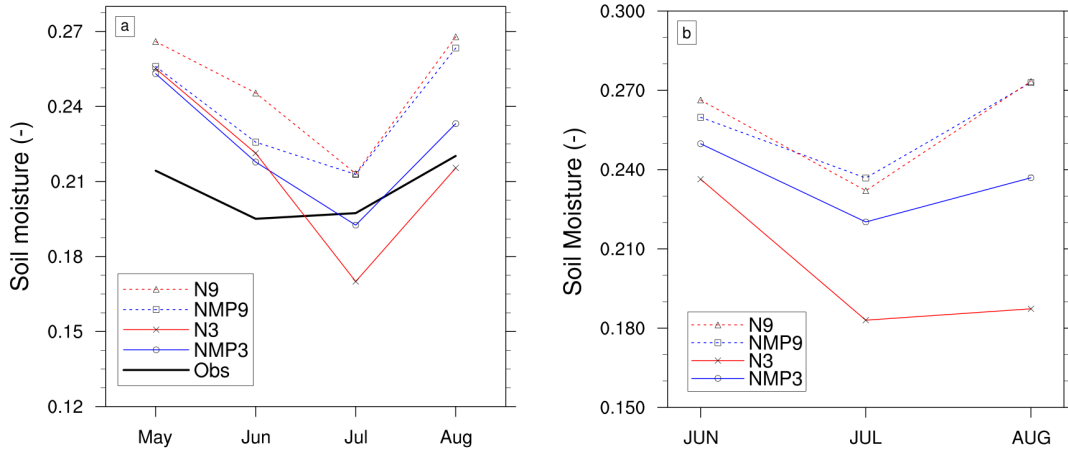
Figure 5.4.3: *(a): Monthly averaged soil moisture content over Denmark as a function of time for observations, N3, NMP3, N9 and NMP9. The observations are representative for the upper soil layer down to a depth of* 0.5-2 *cm, while the simulations represent a soil depth of* 10 *cm. (b): Monthly averaged soil moisture content over Denmark down to 1 m depth as function of time for the simulations N3, NMP3, N9 and NMP9.*

in Niu et al. (2011). The difference may be connected to the aquifer below the soil column that allows groundwater inflow in Noah-MP, a feature that is not implemented in the Noah LSM.

5.4.2 Surface fluxes

The average energy terms and latent heat flux terms over croplands for JJA are shown in Fig. 5.4.4 for N3 and NMP3. The low resolution simulations are neglected in this comparison due to the large overestimation of precipitation and soil moisture. The net radiation is similarly modeled by both N3 and NMP3 and therefore the results shown are mainly related to differences in the partitioning of the net surface energy.

In June, much higher ground heat fluxes are shown by NMP3 compared to N3 and therefore less surface energy goes into the sensible and latent heat fluxes. Niu et al. (2011) also reported larger variability in ground heat fluxes in Noah-MP compared to Noah and found better agreement with the observations in Noah-MP. The Bowen ratio (BR=SH/LH) is about 1.5 for NMP3, while N3 shows values lower than 0.7. The difference is mainly caused by the very low transpiration in NMP3 that is related to a relatively low LAI value ($\simeq 2$). However, the low transpiration in NMP3 is partly compensated by larger soil evaporation than in N3. The little dent in the canopy evaporation shown at 4–7 UTC in N3
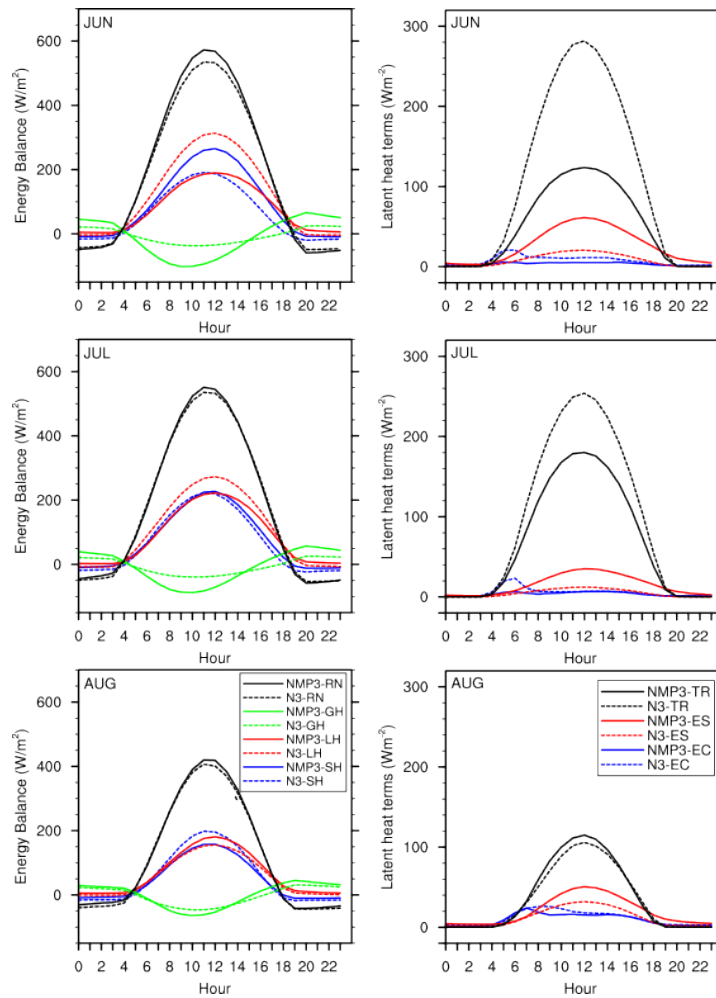
Figure 5.4.4: *The diurnal energy balance terms and latent heat flux terms averaged over Denmark during JJA for N3 and NMP3. Net radiation is represented by RN, sensible heat flux by SH, latent heat flux by LH, ground heat flux by GH, transpiration by TR, soil evaporation by ES and evaporation from the canopy by EC. Time in UTC.*

represents evaporation of dew from the canopy. In July, the ground heat flux is still larger in NMP3 than in N3 but the sensible and latent heat fluxes are more similar represented. The bowen ratio for NMP3 is reduced to about 1, due to increased transpiration compared to June (LAI in July is $\simeq 3$), while N3 shows Bowen ratios lower than 1. The surface energy partitioning during July shown by NMP3 agrees well with the high resolution experiment simulation in Refslund et al. (2013b) (Fig. 7) using concurrent vegetation fractions. In August, the differences between NMP3 and N3 is minor for all parameters of the surface energy balance. The Bowen ratio shown by NMP3 is lower than 1, while a slightly higher value are shown by N3. The difference in latent heat flux between the two
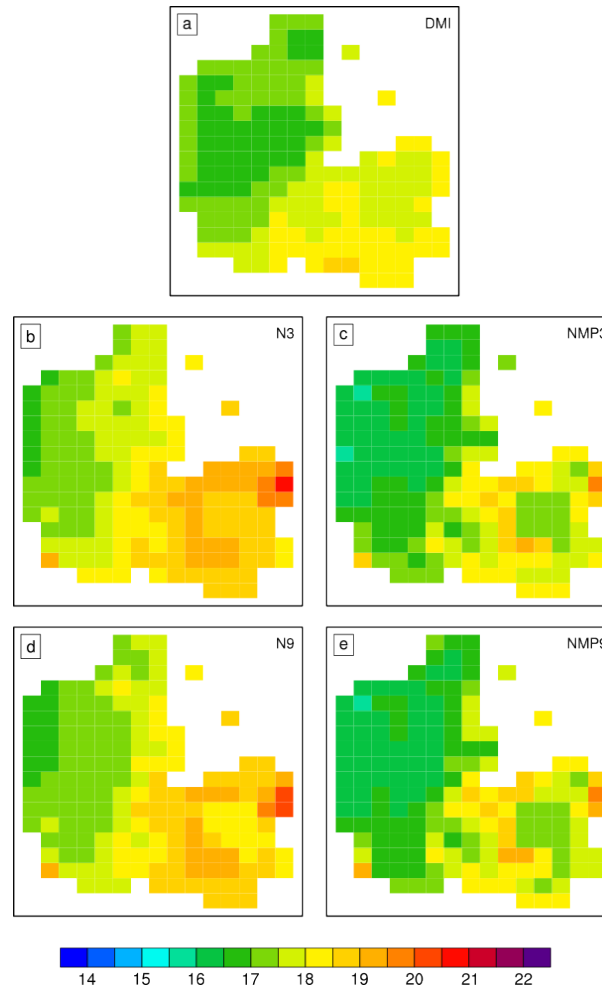
Figure 5.4.5: *Averaged gridded 2-m temperature during June, July and August for (a) the DMI observations, (b)N3, (c) NMP3, (d) N9 and (e) NMP9.*

simulations is mainly caused by different soil evaporation.

5.4.3   Surface temperature

The simulated 2 m temperatures during JJA are compared to the DMI gridded observations in Fig. 5.4.5. Generally, the result obtained from Noah-MP (Fig. 5.4.5c and e) are colder than the observations (Fig. 5.4.5a), while warmer when using the Noah LSM (Fig. 5.4.5b and d). The largest differences in temperature between the Noah LSM and Noah-MP simulations are found in the eastern regions of Denmark with differences of 2°–3°C. The clear east-west temperature gradient shown by the Noah LSM is not as clear in the Noah-MP simulations, which is in better agreement with the observations.

Figure 5.4.6: *Averaged gridded 2-m temperature bias (model–obs) over Denmark during June, July and August using Noah and Noah-MP at two spatial resolution.*

Gridded monthly 2-m temperature biases averaged over Denmark during JJA are shown in Figure 5.4.6. The Noah LSM shows positive temperature bias for all months, while the Noah-MP simulations tends to underestimate the observ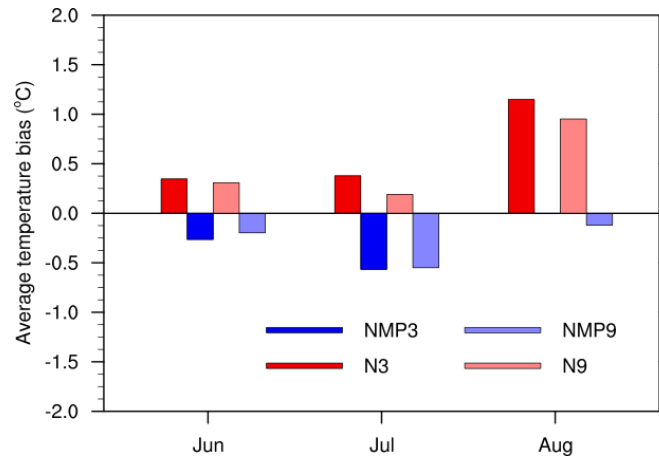ed temperatures. The absolute temperature biases in June and July are below 0.5°C for all simulations with Noah-MP showing better performance during June while worse performance is found in July compared to the Noah LSM. The Noah-MP simulations show almost zero bias in August while the corresponding biases for the Noah simulations are about 1°C. The temperature improvement in Noah-MP occurs despite of similar distribution of surface energy during August, shown in Fig. 5.4.4. Thus, the cause for this improvement could be related to differences in how the 2-m temperature is paramterized in Noah and Noah-MP (Equation 4.1.9 and 5.2.11).

5.5   Discussion and conclusion

This study shows that the Noah-MP LSM coupled to the WRF modeling framework is capable of producing good results. These were obtained despite that no tuning of the model to the summer conditions over Denmark 2006 was attempted. Being a complex model, the Noah-MP LSM includes many tunable parameters that demand careful consideration before good performance can be assumed. Conversely, the Noah LSM is a fairly simple model that typically shows good performance during the summer periods, while snow covered conditions are more problematic (Barlage et al., 2010). The results presented in this thesis shows that the performance of Noah-MP during a summer simulation over Denmark is better than the performance obtained using the Noah LSM, at least in relation to precipitation and 2 m temperature. Therefore, it is very likely that better

performance of Noah-MP is also found during winter simulations compared to the Noah LSM.

The monthly accumulated precipitation simulated by Noah-MP in high resolution showed excellent agreement with the gridded observations over Denmark and the temperature biases was below $0.5°C$ for all months. However, the results on the surface energy distribution using Noah and Noah-MP are hard to verify due to the lack of spatially distributed observations. It was shown in Refslund et al. (2013b) that the performance of Noah in representing the surface energy distribution is very dependent on the representation of F_v. Similarly, the results obtained using Noah-MP with recommended options (constant vegetation fraction), indicate that the monthly prescribed values of LAI needs special attention.

The weather during July 2006 over Denmark was exceptionally warm and dry. Thus, high Bowen ratios should be expected during this period. However, the NMP3 simulation shows lower Bowen ratios in July compared to June (Fig. 5.4.4), although June was both colder and wetter. The reason for this is the much higher transpiration shown by NMP3 during July compared to June. (Refslund et al., 2013b) found that observations at two FluxNet stations in Denmark showed Bowen ratios mostly below 1 during June, while Bowen ratios was above 1 during July. Therefore, it is likely that the prescribed LAI value of 2 in Noah-MP during June is too low for the region of Denmark, while the LAI value of 3 is more representative for the July conditions that prevailed in 2006. In comparison, the LAI values in Noah are closer to 5 for both June and July, since the vegetation fractions are at their maximum. To avoid these considerations, future updates of the Noah-MP code should include a possibility to use concurrent LAI from remote-sensing.

The soil moisture content down to a depth of 1 m showed large differences between NMP3 and N3, although the precipitation amounts were fairly similar predicted. This needs to be investigated more thoroughly using soil moisture measurement that covers the entire rootzone and should be combined with observations of the surface energy balance. As mentioned previously, similar differences in soil moisture was also observed in offline simulations by Niu et al. (2011) during a dry-down period, with the better performance shown by Noah-MP compared to Noah. Despite of higher soil moisture content, the offline Noah-MP simulations also showed lower latent heat fluxes when compared to the offline Noah simulation. This is in accordance with the coupled simulations for July shown in Fig. 5.4.4.

The Noah-MP LSM has great potential for improving weather and climate simulation due to its many advanced parameterization. However, a large effort by the modeling community is required to evaluate the performance of the model. As a starting point, evaluation should be based on the recommended options as was done in this study. This will ensure that critical updates are easier detected such as the addition of LAI from remote sensing. Furthermore, more validation of Noah-MP in offline settings is needed.

CHAPTER 6

Summary and Conclusions

This study concerned the importance of accurate representation of the land surface processes and their feedbacks with the atmosphere within the WRF model. These processes are critical for accurate prediction of near-surface variables and have significant influence on the temporal evolution of the atmospheric boundary layer. Therefore, this study has implications for weather prediction, wind energy forecasting, air pollution modeling and regional climate assessments, to name a few.

The WRF model investigations in this thesis were carried out using two LSMs with very different degrees of complexity. The Noah LSM combines parameterizations from both first and second generation LSM developments, while the Noah-MP LSM was configured to use parameterizations from second and third generation developments. The Noah LSM is a well proven model commonly used in the WRF model, while the Noah-MP LSM is recent and therefore has not been tested thoroughly in the WRF modeling framework. This study presents the first evaluation of the performance of Noah-MP during seasonal WRF simulations in high resolution, as far as we know.

The first part of this thesis studied the impacts of concurrent MODIS green vegetation fraction data in long-term WRF simulations over Europe and Denmark when using the Noah LSM. These investigations were motivated by previous studies, which had failed to identify the optimal method (linear or quadratic) for producing MODIS F_v data for use in the Noah LSM. Two studies were carried out to ensure a thorough evaluation of the performance of the new datasets. The second part was devoted to evaluation of the Noah-MP LSM coupled to the WRF model.

The first study (Refslund et al., 2013a) presented a new methodology for obtaining MODIS F_v products and tested their performance in low resolution WRF

simulations over Europe. A high resolution, high quality NDVI climatology was derived from 10 years of MODIS satellite images using novel data-processing techniques. Its main purpose was to provide an accurate method for gap filling of single-year NDVI data sets. The MODIS F_v products were derived using a land-use class dependent approach combined with both linear and quadratic NDVI to F_v relationships. The MODIS products were tested during a heat wave period to maximize the differences in F_v and were compared to a simulation using the default F_v climatology in WRF. The MODIS F_v products are an improvement over the default F_v climatology in WRF for several reasons: (1) the MODIS products are produced at much higher spatial and temporal resolution, (2) ecosystem-dependent gap filling was used instead of spatial averaging to preserve differences in seasonalities between various land cover types and (3) only high quality pixels were used in the process to avoid erroneous satellite retrievals. The results showed that the quadratic F_v product was the best performing product. It significantly improved temperature predictions during the heat wave period compared to the default F_v data. Large differences in the sensible and latent heat fluxes were observed, while differences in precipitation were minor.

The objective of the second study (Refslund et al., 2013b) was to investigate the performance of the quadratic MODIS F_v product in WRF simulation down to cloud-resolving scale over Denmark. The default F_v data in WRF was used as a control run, while an experiment was conducted with the quadratic MODIS F_v. Simulations at two different spatial resolutions were compared to also investigate the effects of parameterized and explicit (resolved) convection. The results showed that explicit convection improved the prediction of warm season precipitation significantly and resulted in good agreement with the soil moisture observations. The surface energy balance terms showed large differences, especially during the dry period of July. The quadratic F_v showed much better temporal agreement with station measurements of Bowen ratio compared to the default F_v data during June, July and August. The simulation of temperature and wind speed were slightly improved during the fall. The study showed that concurrent MODIS F_v data in the WRF model may improve the predictions but it does not always lead to more realistic simulations. However, the new MODIS F_v data is consistent with the LCC data in WRF and therefore, it can represent the heterogeneous land surface more accurately.

The second part of this thesis was devoted to coupling, debugging and testing the Noah-MP LSM in the WRF modeling framework. This task was very time-consumming due to the number of options implemented in the model. The work resulted in additional options being added, structural changes to the WRF model and correction of errors in Noah-MP. The many parameterizations and options provided by Noah-MP and the approach used for solving energy balance equations were presented in this thesis. The performance of Noah-MP in the WRF model was evaluated during a summer simulation over Denmark and compared to a control simulation using the Noah LSM. Only the recommended options in Noah-

MP were used for this purpose. Excellent agreement with observed precipitation and good agreement with observations of soil moisture measurements were found. 2-m temperatures was much better predicted using the Noah-MP LSM than using the Noah LSM. Overall, the performance of Noah-MP was satisfactory despite that no effort was spend on tuning the model beforehand. However, the study showed that further improvements in the representation of vegetation, through LAI and SAI, are needed. In general, the Noah-MP LSM has great potential for improving the predictions of the WRF model but significant evaluation of its performance is needed.

CHAPTER 7

Future research

This thesis suggest several interesting topics for future research using the WRF model. First of all, it would be very interesting to produce a near real-time vegetation product for the real-time weather prediction system setup at DTU Wind Energy. For this work, the NDVI climatology should be combined with daily (or weekly) observations of NDVI images to generate concurrent green vegetation fraction data. Although, such system might not have great effect on the average daily predictions, it could be very important during heat wave and drought conditions. The long-term effect of such system could be assessed by running a parallel real-time system using climatological vegetation data.

The studies presented in Appendix A and B should be expanded to a multi-year evaluation of the impact of concurrent vegetation fraction data in WRF. This would allow monthly and seasonal investigations of the impacts of concurrent vegetation data in a more statistically robust way, although it would require large amount of disk space if cloud-resolving scales where to be investigated.

The study in Appendix B suggest that the performance of the convective parameterization schemes must be improved. The Kain-Fritsch scheme is normally considered as one of the better performing schemes, however, this needs to be investigated more thoroughly in a sensitivity study. Such study is crucial for accurate predictions by the land surface models.

The Noah-MP offers many possibilities for both weather and climate research in the future. However, first of all extensive testing of the model is needed to ensure that accurate predictions are obtained. Such investigations should be carried out using the recommended options as reference simulations. Thus, the influence of various parameterization options can be evaluated. In addition, satellite observations of LAI and SAI should be allowed into the model structure to ensure that the surface energy balance is correctly simulated. Furthermore,

there has been no investigation of how Noah-MP influences wind speed and wind direction.

Bibliography

Allerup, P., H. Madsen, and F. Vejen, 1998: Standard values for precipitation correction (1961–90). Technical report, Danish Meteorological Institute, Copenhagen, Denmark, technical report 98-10.

Avissar, R. and R. A. Pielke, 1989: A parameterization of heterogeneous land surfaces for atmospheric numerical models and its impact on regional meteorology. *Mon. Wea. Rev.*, **117**, 2113–2136.

Ball, J., L. E. Woodrow, and J. A. Beny, 1987: *A model predicting stomatal conductance and its contribution to the control of photosynthesis under different environmental conditions*, volume 4 of *Progress in Photosynthesis research*. Nijhoff, Dordrecht, 221–224 pp.

Barlage, M., F. Chen, M. Tewari, K. Ikeda, D. Gochis, J. Dudhia, R. R., B. Livneh, M. Ek, and K. Mitchell, 2010: Noah Land Surface Model modifications to improve snowpack prediction in the Colorado Rocky Mountains. *J. Geophys. Res*, **115**, 15, doi:10.1029/2009JD013470.

Barstad, I., A. Sorteberg, F. Flatøy, and M. Déqué, 2009: Precipitation, temperature and wind in Norway: dynamical downscaling of ERA40. *Clim. Dyn.*, **33**, 769–776, doi:10.1007/s00382-008-0476-5.

Bonan, G., 2008: *Ecological Climatology: Concepts and Applications*. Cambridge University Press, second edition.

Bukovsky, M. and D. Karoly, 2009: Precipitation Simulations Using WRF as a Nested Regional Climate Model. *J. Appl. Meteor. Climatol.*, **48**, 2152–2159, doi:10.1175/2009jamc2186.1.

Chen, F. and J. Dudhia, 2001: Coupling an advanced land surface-hydrology model with the Penn State-NCAR MM5 modeling system. part ii: Preliminary model validation. *Mon. Wea. Rev.*, **129**, 587–604.

Chen, F., Z. Janjic, and K. Mitchell, 1997: Impact of atmospheric surface layer parameterization in the new land-surface scheme of the NCEP Mesoscale Eta numerical model. *Bound. Layer Meteor.*, **185**, 391–421.

Chen, F., K. Mitchell, J. Schaake, Y. Xue, H. Pan, V. Koren, Y. Duan, M. Ek, and A. Betts, 1996: Modeling of land-surface evaporation by four schemes and comparison with FIFE observations. *J. Geophys. Res.*, **101**, 7251–7268.

Collatz, G., M. Ribas-Carbo, and J. Berry, 1992: Coupled Photosynthesis-Stomatal Conductance Model for Leaves of C4 Plants. *Aust. J. Plant Physiol.*, **19**, 519–538.

Cotton, W. and R. Pielke, 2007: *Human impacts on weather and climate*. Cambridge University Press, 1–308 pp.

Deardorff, J. W., 1978: Efficient prediction of ground surface temperature and moisture, with inclusion of a layer of vegetation. *J. Geophys. Res.*, **83**, 1889–1904.

Della-Marta, P. M., M. R. Haylock, J. Luterbacher, and H. Wanner, 2007: Doubled length of western European summer heatwaves since 1880. *J. of Geophys. Res.*, **112**, D15103, doi:10.1029/2007JD008510.

Dickinson, R., 1983: Land surface processes and climate surface albedos and energy-balance. *Adv. Geophys.*, **25**, 305.

Dickinson, R., A. Henderson-Sellers, and P. Kennedy, 1993: Biosphere-atmosphere Transfer Scheme (BATS) Version 1e as Coupled to the NCAR Community Climate Model. Technical report, University Corporation for Atmospheric Research.

Dickinson, R., A. Henderson-Sellers, P. Kennedy, and M. Wilson, 1986: Biosphere-atmosphere Transfer Scheme (BATS) for the NCAR Community Climate Model. Technical report, University Corporation for Atmospheric Research.

Dickinson, R. E., M. Shaikh, R. Bryant, and L. Graumlich, 1998: Interactive Canopies for a Climate Model. *J. Climate*, **11**, 2823–2836.

Dirmeyer, P., 2001: Climate Drift in a Coupled Land–Atmosphere Model. *J. Hydrometeor.*, **2**, 89–100.

Dirmeyer, P. A., R. D. Koster, and Z. Guo, 2006: Do Global Models Properly Represent the Feedback between Land and Atmosphere?. *J. Hydrometeor*, **7**, 1177–1198.

Dudhia, J., 1989: Numerical Study of Convection Observed during the Winter Monsoon Experiment Using a Mesoscale Two-Dimensional Model. *J. Atmos. Sci.*, **46**, 3077–3107.

Durre, I. and J. M. Wallace, 2001: The Warm Season Dip in Diurnal Temperature Range over the Eastern United States. *J. Climate*, **14**, 354–360.

Ek, M. B., K. E. Mitchell, Y. Lin, E. Rogers, P. Grunmann, V. Koren, G. Gayno, and J. D. Tarpley, 2003: Implementation of Noah land surface model advances in the National Centers for Environmental Prediction operational mesoscale Eta model. *J. Geophys. Res.*, **108**, n/a–n/a, doi:10.1029/2002JD003296.

Farquhar, G. D., S. Caemmerer, and J. A. Berry, 1980: A biochemical model of photosynthetic CO2 assimilation in leaves of C3 species. *Planta*, **149**, 78–90, doi:10.1007/bf00386231.

Field, C., V. Barros, T. Stocker, D. Qin, D. Dokken, K. Ebi, M. Mastrandrea, K. Mach, G.-K. Plattner, S. Allen, M. Tignor, and P. M. (Eds.), 2012: Managing the Risks of Extreme Events and Disasters to Advance Climate Change Adaptation. *Cambridge University Press*, 582pp.

Fischer, E. M., S. I. Seneviratne, D. Lüthi, and C. Schär, 2007: Contribution of land-atmosphere coupling to recent European summer heat waves. *Geophys. Res. Lett.*, **34**, doi:10.1029/2006GL029068.

Floors, R., C. Vincent, S.-E. Gryning, A. Peña, and E. Batchvarova, 2013: The Wind Profile in the Coastal Boundary Layer: Wind Lidar Measurements and Numerical Modelling. *Bound.-Layer Meteorol.*, 1–23, doi:10.1007/s10546-012-9791-9.

Friedl, M. A., D. K. McIver, J. C. F. Hodges, X. Y. Zhang, D. Muchoney, A. H. Strahler, C. E. Woodcock, S. Gopal, A. Schneider, A. Cooper, A. Baccini, F. Gao, and C. Schaaf, 2002: Global land cover mapping from MODIS: algorithms and early results. *Remote Sens. Environ*, **83**, 287–302.

García-Díez, M., J. Fernández, L. Fita, and C. Yague, 2012: Seasonal dependence of WRF model biases and sensitivity to PBL schemes over Europe. *Q.J.R Meteorol. Soc.*, doi:10.1002/qj.1976.

Gemmill, W., B. Katz, and X. Li, 2007: Daily Real-Time Global Sea Surface Temperature - High Resolution Analysis at NOAA/NCEP. Office note nr. 260, 39 pp, NOAA/NWS/NCEP/MMAB.

Gulden, L. E., E. Rosero, Z.-L. Yang, T. Wagener, and G.-Y. Niu, 2008: Model performance, model robustness, and model fitness scores: A new method for identifying good land-surface models. *Geophys. Res. Lett.*, **35**, doi:10.1029/2008*GL*033721.

Guo, Z. and P. A. Dirmeyer, 2006: Evaluation of the Second Global Soil Wetness Project soil moisture simulations: 1. Intermodel comparison. *J. Geophys. Res.*, **111**, n/a–n/a, doi:10.1029/2006JD007233.

Gutman, G. and A. Ignatov, 1998: The derivation of the green vegetation fraction from NOAA/AVHRR data for use in numerical weather prediction models. *Int. J. Rem. Sens.*, **19**, 1533–1543, doi:10.1080/014311698215333.

Guttorp, P. and J. Xu, 2011: Climate change, trends in extremes, and model assessment for a long temperature time series from Sweden. *Environmetrics*, **22**, 456–463, doi:10.1002/env.1099.

Hahmann, A. N. and R. E. Dickinson, 1997: RCCM2–BATS Model over Tropical South America: Applications to Tropical Deforestation. *J. Climate*, **10**, 1944–1964.

Hirschi, M., S. Seneviratne, V. Alexandrov, F. Boberg, C. Boroneant, O. B. Christensen, H. Formayer, B. Orlowsky, and P. Stepanek, 2010: Observational evidence for soil-moisture impact on hot extremes in southeastern Europe. *Nature Geosci.*, **4**, 17–21, doi:10.1038/ngeo1032.

Hofstra, N., M. Haylock, M. New, and P. Jones, 2009: Testing E-OBS European high-resolution gridded data set of daily precipitation and surface temperature. *J. Geophys. Res*, **114**, D21101, doi:10.1029/009JD011799.

Hofstra, N., M. New, and C. McSweeney, 2010: The influence of interpolation and station network density on the distributions and trends of climate variables in gridded daily data. *Clim. Dyn.*, **35**, 841–858.

Hong, S., V. Lakshmi, E. Small, F. Chen, M. Tewari, and K. Manning, 2009: Effects of vegetation and soil moisture on the simulated land surface processes from the coupled WRF/Noah model. *J. Geophys. Res*, **114**, doi:10.1029/208JD011249.

Hong, S.-Y., J. Dudhia, and S.-H. Chen, 2004: A revised approach to ice-microphysical processes for the bulk parameterization of cloud and precipitation. *Mon. Wea. Rev.*, **132**, 103–120.

Janjic, Z. I., 1996: The Surface Layer in the NCEP Eta Model. *Am. Met. Soc.*, 354–355.

— 2002: Nonsingular Implementation of the Mellor-Yamada Level 2.5 Scheme in the NCEP Meso model. Office Note 437, NCEP.

Jarvis, P. G., 1976: The Interpretation of the Variations in Leaf Water Potential and Stomatal Conductance Found in Canopies in the Field. *Phil. Trans. R. Soc. Lond. B.*, **273**, 593–610, doi:10.1098/rstb.1976.0035.

Jiang, L., F. Kogan, W. Guo, J. D. Tarpley, K. Mitchell, M. Ek, Y. Tian, W. Zheng, C. Zou, and B. Ramsay, 2010: Real-time weekly global green vegetation fraction derived from advanced very high resolution radiometer-based NOAA operational global vegetation index (GVI) system. *J. Geophys. Res*, **115**, doi:10.1029/2009JD013204.

Kain, J. S., 2004: The Kain Fritsch Convective Parameterization: An Update. *J. Appl. Meteorol.*, **43**, 170–181.

Koren, V., J. Schaake, K. Mitchell, Q.-Y. Duan, F. Chen, and J. M. Baker, 1999: A parameterization of snowpack and frozen ground intended for NCEP weather and climate models. *J. Geophys. Res.*, **104**, 19569–19585, doi:10.1029/1999JD900232.

Kyselý, J. and E. Plavcová, 2010: A critical remark on the applicability of E-OBS European gridded temperature data set for validating control climate simulations. *J. Geophys. Res*, **115**, doi:10.1029/2010JD014123.

Lakshmi, V., S. Hong, E. Small, and F. Chen, 2011: The influence of the land surface on hydrometeorology and ecology: New advances from modeling and satellite remote sensing. *Hydrol. Res.*, **42**, 95–112, doi:10.2166/nh.211.071.

Leuning, R., 1990: Modeling Stomatal Behavior and Photosynthesis of EucalyptusGrandis. *Aust. J. Plant Physiol.*, **17**, 159–175.

Loveland, T., B. Reed, J. Brown, D. Ohlen, J. Zhu, Y. L., and J. Merchant, 2000: Development of a Global Land Cover Characteristics Database and IGBP DISCover from 1-km AVHRR Data. *Int. J. Rem. Sens.*, **21**, 1303–1330.

Mahrt, L. and H. Pan, 1984: A two-layer model of soil hydrology. *Bound.-Layer Meteorol.*, **29**, 1–20.

Manabe, S., 1969: Climate and the Ocean Circulation I. *Mon. Wea. Rev.*, **97**, 739–774.

Miller, D. and R. White, 1998: A conterminous United States multilayer soil characteristics dataset for regional climate and hydrology modeling. *Earth Interact.*, **2**, 1–26.

Miller, J., M. Barlage, X. Zeng, H. Wei, K. Mitchell, and D. Tarpley, 2006: Sensitiviy of the NCEP/Noah land surface model to the MODIS green vegetation fraction data set. *Geophys. Res. Lett.*, **33**, doi:10.1029/2006L026636.

Mlawer, E. J., S. J. Taubman, P. D. Brown, M. J. Iacono, and S. A. Clough, 1997: Radiative transfer for inhomogeneous atmospheres: RRTM, a validated correlated-k model for the longwave. *J. Geophys. Res*, **102**, 16663–16682, doi:10.1029/97JD00237.

Mooney, P. A., F. J. Mulligan, and R. Fealy, 2013: Evaluation of the sensitivity of the weather research and forecasting model to parameterization schemes for regional climates of europe over the period 1990–95. *J. Climate*, **26**, 1002–1017.

Niu, G.-Y. and Z.-L. Yang, 2004: Effects of vegetation canopy processes on snow surface energy and mass balances. *J. Geophys. Res.*, **109**, n/a–n/a, doi:10.1029/2004JD004884.

Niu, G.-Y. and Z.-L. Yang, 2006: Effects of Frozen Soil on Snowmelt Runoff and Soil Water Storage at a Continental Scale. *J. Hydrometeor*, **7**, 937–952, doi:10.1175/JHM538.1.

Niu, G.-Y., Z.-L. Yang, R. E. Dickinson, and L. E. Gulden, 2005: A simple TOPMODEL-based runoff parameterization (SIMTOP) for use in global climate models. *J. Geophys. Res.*, **110**, n/a–n/a, doi:10.1029/2005JD006111.

Niu, G.-Y., Z.-L. Yang, R. E. Dickinson, L. E. Gulden, and H. Su, 2007: Development of a simple groundwater model for use in climate models and evaluation with Gravity Recovery and Climate Experiment data. *J. Geophys. Res.*, **112**, n/a–n/a, doi:10.1029/2006JD007522.

Niu, G.-Y., Z.-L. Yang, K. E. Mitchell, F. Chen, M. B. Ek, M. Barlage, A. Kumar, K. Manning, D. Niyogi, E. Rosero, M. Tewari, and Y. Xia, 2011: The community Noah land surface model with multiparameterization options (Noah-MP): 1. Model description and evaluation with local-scale measurements. *J. Geophys. Res.*, **116**, doi:10.1029/2010*JD*015139.

Pan, H.-L. and L. Mahrt, 1987: Interaction between soil hydrology and boundary-layer development. *Bound.-Layer Meteorol.*, **38**, 185–202.

Pielke, R., 2001: Influence of the spatial distribution of vegetation and soils on the prediction of cumulus convective rainfall. *Rev. Geophys*, 151–177.

Pitman, A. J., 2003: The evolution of, and revolution in, land surface schemes designed for climate models. *Int. J. Clim.*, **23**, 479–510, doi:10.1002/joc.893.

Polcher, J., B. McAvaney, P. Viterbo, M.-A. Gaertner, A. Hahmann, J.-F. Mah-fouf, J. Noilhan, T. Phillips, A. Pitman, C. Schlosser, J.-P. Schulz, B. Timbal, D. Verseghy, and Y. Xue, 1998: A proposal for a general interface between land surface schemes and general circulation models. *Global Planet. Change*, **19**, 261 –276, doi:10.1016/S0921-8181(98)00052-6.

Rauscher, S., E. Coppola, C. Piani, and F. Giorgi, 2009: Resolution effects on regional climate model simulations of seasonal precipitation over Europe. *Clim. Dyn.*, **35**, 685–711.

Rebetez, M., O. Dupont, and M. Giroud, 2009: An analysis of the July 2006 heatwave extent in Europe compared to the record year of 2003. *Theor. Appl. Climatol.*, **95**, 1–7, doi:10.1007/s00704-007-0370-9.

Refslund, J., E. Dellwik, A. Hahmann, M. Barlage, and E. Boegh, 2013a: Impacts of green vegetation fraction data in WRF simulations. *Theor. Appl. Climatol.*, **In review**.

— 2013b: The interplay of vegetation and precipitation processes in high resolution WRF simulations. *J. Geophys. Res.*, **submitted**.

Robine, J.-M., S. Cheung, S. L. Roy, H. Oyen, C. Griffiths, J.-P. Michel, and F. R. Herrmann, 2008: Death toll exceeded 70,000 in Europe during the summer of 2003. *C. R. Biol.*, **331**, 171–178.

Saha, S., S. Moorthi, H.-L. Pan, X. Wu, J. Wang, S. Nadiga, P. Tripp, and R. Kistler, 2010: The NCEP Climate Forecast System Reanalysis. *Bull. Amer. Meterol. Soc.*, **91**, 1015–1057.

Schaake, J. C., V. I. Koren, Q.-Y. Duan, K. Mitchell, and F. Chen, 1996: Simple water balance model for estimating runoff at different spatial and temporal scales. *J. Geophys. Res.*, **101**, 7461–7475, doi:10.1029/95JD02892.

Schär, C., P. Vidale, D. Lüthi, C. Frei, C. Háberli, M. Liniger, and C. Appelzeller, 2004: The role of increasing temperature variability in European summer heat-waves. *Nature*, **427**, 332–336, doi:0.1038/nature02300.

Scharling, M., 2012: Climate Grid Denmark. Technical report, Danish Meteoro-logical Institute, (in english).
URL www.dmi.dk/dmi/tr12-10.pdf

Schwartz, M. D. and T. R. Karl, 1990: Spring Phenology: Nature's Experiment to Detect the Effect of "Green-Up" on Surface Maximum Temperatures. *Mon. Wea. Rev.*, **118**, 883–890.

Sellers, P. J., 1985: Canopy reflectance, photosynthesis and transpiration. *Int. J. Rem. Sens.*, **6**, 1335–1372, doi:10.1080/01431168508948283.

Sellers, P. J., Y. C. S. Y. Mintz, and A. Dalcher, 1986: A Simple Biosphere Model (SiB) for Use within General Circulation Models. *J. Atmos. Sci.*, **43**, 505–531.

Seneviratne, S., T. Corti, E. L. Davin, M. Hirschi, E. Jaeger, I. Lehner, B. Orlowsky, and A. Teuling, 2010: Investigating soil moisture–climate interactions in a changing climate: A review. *Earth-Sci. Rev.*, **99**, 125 – 161, doi:10.1016/j.earscirev.2010.02.004.

Seneviratne, S., D. Luethi, M. Litschi, and C. Schär, 2006: Land-atmosphere coupling and climate change in Europe. *Nature*, **443**, 205–209.

Sertel, E., A. Robock, and C. Ormeci, 2010: Impacts of land cover data quality on regional climate simulations. *Int. J. Climatol.*, **30**, 1942–1953, doi:10.1002/joc.2036.

Skamarock, W. C., J. B. Klemp, J. Dudhia, D. O. Gill, M. Barker, K. G. Duda, X. Y. Huang, W. Wang, and J. G. Powers, 2008: A description of the Advanced Research WRF Version 3. Technical report, National Center for Atmospheric Research.

Soares, P., R. Cardoso, P. Miranda, J. Medeiros, M. Belo-Pereira, and F. Espirito-Santo, 2012: WRF high resolution dynamical downscaling of ERA-Interim for Portugal. *Clim. Dyn.*, **39**, 2497–2522, doi:10.1007/s00382-012-1315-2.

Teuling, A., S. Seneviratne, R. Stöckli, M. Reichstein, E. Moors, P. Ciais, S. Luyssaert, S. van den Hurk, C. Ammann, C. Bernhofer, E. Dellwik, D. Gianelle, B. Gielen, T. Grünwald, K. Klumpp, L. Montagnani, C. Moureaux, M. Sottocornola, and G. Wohlfahrt, 2010: Contrasting response of European forest and grassland energy exchange to heatwaves. *Nat. Geosci.*, **3**, 722–727.

Verhoef, A., C. Ottle, B. Cappelaere, T. Murray, S. Saux-Picart, M. Zribi, F. Maignan, N. Boulain, J. Demarty, and D. Ramier, 2012: Spatio-temporal surface soil heat flux estimates from satellite data: results for the AMMA experiment at the Fakara (Niger) supersite. *Agr. Forest Meteorol.*, **154–155**, 55–66.

Verseghy, D. L., 1991: CLASS–A Canadian land surface scheme for GCMS. I. Soil model. *Int. J. Climatol.*, **11**, 111–133, doi:10.1002/joc.3370110202.

Vidale, P., D. Lüthi, R. Wegmann, and C. Schär, 2007: European summer climate variability in a heterogeneous multi-model ensemble. *Climatic Change*, **81**, 209–232.

Wagner, W., W. Dorigo, R. de Jeu, D. Fernandez, J. Benveniste, E. Haas, and M. Ertl, 2012: Fusion of Active and Passive Microwave Observations to Create an Essential Climate Variable Data Record on Soil Moisture. *ISPRS Annals*

of Photogrammetry, Remote Sensing and Spatial Information Sciences, **I-7**, 315–321, doi:10.5194/isprsannals-I-7-315-2012.

Warrach-Sagi, K., T. Schwitalla, V. Wulfmeyer, and H.-S. Bauer, 2013: Evaluation of a climate simulation in Europe based on the WRF–NOAH model system: precipitation in Germany. *Clim. Dyn.*, 1–20, doi:10.1007/s00382-013-1727-7.

Yang, R. and M. A. Friedl, 2003: Modeling the effects of three-dimensional vegetation structure on surface radiation and energy balance in boreal forests. *J. Geophys. Res.*, **108**, n/a–n/a, doi:10.1029/2002JD003109.

Yang, Z.-L., 2004: *Modeling land surface processes in short-term weather and climate studies, in Observation, Theory and Modeling of Atmospheric Variability*. World Scientific Series on Meteorology of East Asia, World Scientific, New Jersey.

Yang, Z.-L., G.-Y. Niu, K. E. Mitchell, F. Chen, M. B. Ek, M. Barlage, L. Longuevergne, K. Manning, D. Niyogi, M. Tewari, and Y. Xia, 2011: The community Noah land surface model with multiparameterization options (Noah-MP): 2. Evaluation over global river basins. *J. Geophys. Res.*, **116**, n/a–n/a, doi:10.1029/2010JD015140.

Ylhäisi, J. S., H. Tietäväinen, P. Peltonen-Sainio, A. Venäläinen, J. Eklund, J. Räisänen, and K. Jylhä, 2010: Growing season precipitation in Finland under recent and projected climate. *Nat. Hazard Earth Sys.*, **10**, 1563–1574.

Zaitchik, B. F., A. K. Macalady, L. R. Bonneau, and R. B. Smith, 2006: Europe's 2003 heat wave: a satellite view of impacts and land–atmosphere feedbacks. *Int. J. Clim.*, **26**, 743–769, doi:10.1002/joc.1280.

Zeng, X., R. E. Dickinson, A. Walker, M. Shaikh, R. S. DeFries, and J. Qi, 2000: Derivation and Evaluation of Global 1-km Fractional Vegetation Cover Data for Land Modeling. *J. Appl. Meteorol.*, **39**, 826–839.

Appendix - Development and application of concurrent green vegetation fraction in mesoscale models

Authors: Joakim Refslund, Ebba Dellwik, Andrea N. Hahmann, Michael J. Barlage and Eva Bøgh (2013), Theor. Appl. Climatol., in review.

Development and application of concurrent green vegetation fraction in mesoscale models

Joakim Refslund · **Ebba Dellwik** · **Andrea N. Hahmann** · **Michael J. Barlage** · **Eva Boegh**

Abstract Climate change studies suggest increases in heat wave frequencies over Europe in the coming decades. Excessive heat and droughts impact vegetation seasonalities and lead to alterations in surface energy partitioning. In this study, the atmospheric conditions during the 2006 heat wave over Europe were simulated using the Weather Research and Forecasting (WRF) model. To account for changed vegetation phenology, new high-resolution green vegetation fraction (GVF) datasets were derived using only high-quality satellite retrievals. WRF simulations were compared to daily gridded temperature observations. The simulation using a quadratic normalized difference vegetation index to GVF relationship resulted in consistent improvements of modeled temperatures. The model mean temperature cold bias was reduced by 10% for the whole domain and by 20-45% in areas affected by the heat wave. Model simulations during heat waves and droughts, when vegetation conditions deviates from the climatology, require updated land surface properties in order to obtain accurate results.

Keywords Green Vegetation Fraction · WRF · Heat wave · NDVI · MODIS

1 Introduction

The presence of vegetation influences weather and climate through its modification of the energy and water exchange across the land-atmosphere boundary. Partitioning of net solar radiative energy into sensible, latent and ground heat fluxes affects moisture and temperature fields which in turn can alter the structure of the planetary boundary layer (PBL) leading to changes in cloud cover, rainfall and to the development of thunderstorms (Stull 1988; Pielke 2001; Pielke et al 2007; Montandon et al 2011). Conversely, longer-term meteorological conditions and persistent climatic changes influence the distribution of vegetation; for example by exposing them to stresses related to excessive heat and drought.

For Europe, climate change studies show that the occurrence of heat waves and above-average high temperatures in the summer months will increase during the coming decades leading to dryer summer conditions (Teuling et al 2010; Seneviratne et al 2006) and, consequently, to changes in land cover characteristics through altered vegetation seasonalities. The predictions have been supported by at least three summer heat waves during the last decade, in August 2003, July 2006 and in June and July 2010. The periods were associated with widespread impact on human mortality, ecosystem damages and crop failures, water shortages and severe thunderstorm development (Teuling et al 2010; Della-Marta et al 2007).

The land cover characteristics in regional weather prediction and climate models can be represented and derived in several ways. The Noah land surface model coupled to the WRF model uses GVF as a tool to represent vegetation seasonalities (Skamarock et al 2008). The horizontal distribution of vegetation canopies are directly represented by the GVF, whereas the leaf area index (LAI), that is linearly scaled within a certain range using GVF, describes its vertical thickness in each grid cell. The values of surface albedo, emissivity and roughness are scaled in a similar fashion. Thus, the surface energy calculations in Noah are critically dependent on the GVF data.

J. Refslund · E. Dellwik · A.N. Hahmann
DTU Wind Energy, Technical University of Denmark, Frederiksborgvej 399, Roskilde, 4000, DK
E-mail: jref@dtu.dk

M. J. Barlage
Research Application Lab, NCAR, Boulder, CO, US.

E. Boegh
Roskilde University, Denmark

The GVF climatology typically used in Noah was derived from normalized difference vegetation index (NDVI) composites obtained by the Advanced Very High Resolution Radiometer (AVHRR) during 1985-1991. Monthly global NDVI images with grid spacing of $0.144°$, produced from averaged weekly composites subjected to spatial smoothing for cloud reduction and for gap filling purposes, were converted into GVF using a linear approach (Jiang et al 2010; Gutman and Ignatov 1998). The default climatology has been successfully applied in forecast and climate studies but possess obvious limitations. For instance, the inherent low spatial resolution may reduce accuracy of high resolution simulations while land cover alterations of weekly or biweekly scale are not captured by the temporal resolution (Hong et al 2009; Jiang et al 2010). Additionally, impacts from recent changes in management and climate are not reflected in the data.

Updated land cover information derived from Moderate Resolution Imaging Spectroradiometer (MODIS) NDVI data has recently been applied in studies using Noah. Miller et al (2006) used a linear method (Zeng et al 2000) to compute monthly GVF data from a quality improved 2002 NDVI product (Moody et al 2005). They compared vegetation seasonalities to the AVHRR GVF climatology for the continental United States and found improved seasonality for evergreen needleleaf forest and more realistic summer values for grassland. However, too high GVF values were found during the wintertime for deciduous and mixed forests, grasslands and croplands. Others, investigated high resolution short-term coupled WRF/Noah simulations at 1 km^2 grid spacing to quantify the modeled energy and water response to different MODIS 2002 GVF representations (Hong et al 2009; Lakshmi et al 2011). They derived NDVI from 8-day MODIS reflectance data, replacing cloud contaminated pixels with a null value, and assumed both linear and quadratic NDVI relationships to GVF. Numerical predictions were compared to observations obtained during the 2002 International H$_2$O Project (Weckwerth et al 2004) but did not result in clear recommendations to whether the linear or quadratic relation should be used for future studies.

Short-term simulations, with high spatial resolution, are not sufficient to evaluate the performance of a new high resolution GVF product in WRF. Evaluation must be done across spatial scales, due to the nesting capability of WRF, and during different periods in the annual cycle. A spatially high resolution GVF product with poor performance at low resolution simulations is not desirable. Thus, an initial test of a high resolution GVF product in WRF should be carried out in a long-term simulation at low spatial resolution.

The objective of this study is twofold: (1) to investigate the importance of updated land cover information in WRF/Noah simulations both during heat wave events, where changes are expected to be significant, and during periods where impacts are expected to be minor, (2) to quantify whether a linear or a quadratic MODIS NDVI to GVF relation is more suitable for WRF/Noah simulations. These aims are achieved in three steps. First, we develop a new statistically robust filled MODIS NDVI climatology, reflecting impacts from recent landuse and climatic changes over Europe. High quality is ensured through an extensive post-processing procedure that include a combination of existing methods and novel data-processing ideas. Second, a comparison of the annual variation of GVF for various landuse classes is carried out at a grid spacing that is close to the best resolution offered by the AVHRR GVF data. Third, four climate simulations using different GVF representations in WRF/Noah, including the AVHRR GVF data, are compared to gridded data of temperature to assess model performances.

The paper is structured as follows. In section 2 we introduce the NDVI climatology procedure and the methods used to obtain the final MODIS GVF products. Model setup and verification data are described in section 3 followed by comparisons of the different vegetation seasonalities in section 4. Results from climate simulations are presented in section 5 and, finally, we discuss and conclude our findings in section 6 and 7.

2 Green vegetation fraction data

2.1 Input data

We selected the MODIS instrument aboard the polar-orbiting *Aqua* and *Terra* satelittes as our data source. The NDVI level-3 products (MOD13A2 and MYD13A2, Version-5) are composited every 16 days at 1 km^2 resolution on a tiled Integerized Sinusoidal (IS) $10°$ grid, with each tile covering 1200×1200 km^2. The data sets are produced with an offset of 8 days to improve the temporal frequency, such that the starting period is day 001 and 009 of *Terra* and *Aqua*, respectively. We use ten years of data from *Terra*, 2001–2010, and nine years from *Aqua* starting from year 2002 day 185 and ending at year 2011 day 169. To cover the majority of Europe, we gathered nine tiles for each 8-day period and reprojected the data into geographic coordinates using the MODIS reprojection Tool developed by NASA Land Processes Distributed Active Archive Center (LP DAAC). The resultant latitudinal coverage ranges from $40°$N to $70°$N whereas the longitudinal coverage ranges from $13°$W to $26°$E in the south and from $29°$W to $58.5°$E in the north. The quality control (QC) information for each pixel is stored as 16 bits data that can easily be accessed. We use the MODIS land cover product (MOD12Q1, Type 1) containing the IGBP land cover classification, including 11 natural vegetation classes, 3 developed and mosaicked land classes, and 3 non-vegetated land classes (Friedl et al 2002), to assign each pixel with a landuse class. The southern regions are usually

well represented in the NDVI images even during wintertime, except for the Alps and the Pyrenees, while the most northern areas, approximately above 60°N, only have valid retrievals a few months during the summer. The entire domain consist of 49.2% water and 50.8% land pixels with more than 75% represented in four major land classes: croplands (28.5%), evergreen needleleaf forest (21.4%), mixed forest (16.4%) and open shrubland (10.8%).

2.2 Method

Although algorithms to retrieve high quality MODIS NDVI data have improved over the recent years, noise related to clouds, snow cover and aerosols still remain (Didan and Huete 2006). Typically, noise generates significantly lower NDVI values which lead to unrealistic time series, inconsistent with the relatively slow growth and decay of the vegetation. Several noise-reduction methods have been suggested in the literature to derive high-quality smooth NDVI time series (Viovy et al 1992; Verhoef et al 1996; Roerink et al 2000; Lovell and Graetz 2001; P. and Eklundh 2002; Chen et al 2004; Moody et al 2005; Ma and Veroustraete 2004; Gu et al 2009), but the optimal approach depends on the use of the data since every method has its advantages and drawbacks.

We chose to use only the highest quality NDVI data to minimize noise in the time series. Therefore, a filled NDVI climatology was assessed as an optimal method for gap filling of single-year time series. To derive a filled NDVI climatology, we adopted the idea of ecosystem-dependent filling (ECF) (Moody et al 2005) but combined our procedure with (1) a multi-year averaged background field, (2) a local minimum and maximum correction filter to remove unrealistic average values and (3) a simple three-point smoothing technique also applied by Gu et al (2009). Additionally, we applied a cyclic condition filter to avoid large jumps at the December–January transition. The climatology process is described in the next four sections and additionally depicted in the flowchart on Figure 1.

2.2.1 Multi-year average

A multi-year average for each 16 day composite was calculated from *Aqua* and *Terra* data inspired by Yuan et al (2011). The procedure counts the number of available values in each pixel during the 9 or 10 years and compute the mean value if two conditions are met. First, only pixel values with the highest quality flag (QC= 0) are considered and, second, at least three pixel values are available for the averaging, otherwise the mean is represented by a missing value. The conditions ensure that each mean value represents a "true" background value with minimal influence from noise-affected values.
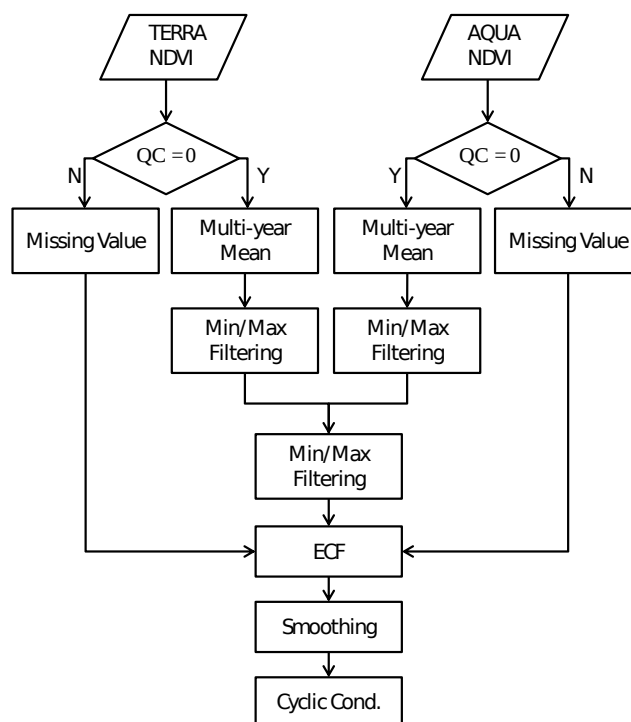

Fig. 1 Flowchart outlining the reconstruction process of the multi-year MODIS NDVI climatology

2.2.2 Local minimum/maximum filter

The above approach does not prevent noise in the discontinous multi-year averages, especially in northern latitudes and during the winter months. Thus, we applied an intelligent local minimum/maximum filter to remove unrealistic values in the time series. Initially, the filter identifies local minimum/maximum values associated with gradients larger than 0.2. Then gradients between four adjacent data points, centered around the local minimum/maximum value, are examined and a decision on which value to remove is made. This decision is based on two conditions: (1) the value of the data point has to be a local minimum or maximum, and, (2) the gradients must have the highest combined absolute gradient. The gradient threshold of 0.2 was selected after careful heuristic considerations.

Initially, the *Aqua* and *Terra* time series were processed seperately to minimize the impacts from mistakes done by the filter that potentially could be compensated for by combining the time series as shown in Figure 1. By mistakes, we here refer to errors which are obvious to the human eye but invisible to the filter. The procedure was repeated on the combined *Aqua* and *Terra* time series using a threshold of 0.1. An example is shown in Figure 2. The filter recognizes the encircled values as unrealistic and remove these before filling and smoothing algorithms are applied to the time series.
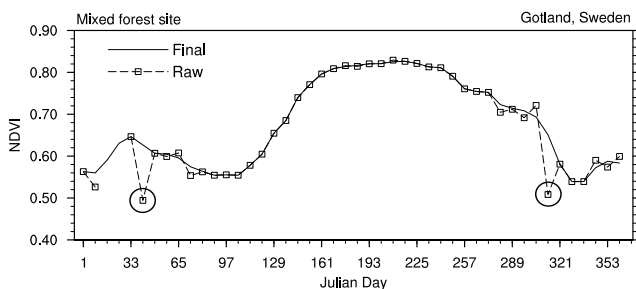
Fig. 2 Time series of NDVI from a pixel located on the island of Got-land, Sweden. The raw multi-year average is indicated by the dashed marked line and the final NDVI climatology by solid line. Enclosed circles are identified as unrealistic values

2.2.3 Filling and smoothing

We applied a simple ecosystem-dependent filling technique to remove missing values in the climatological time series. The method represents the ensemble phenological behavior for each landuse class as the median of all available values for each temporal period within three zonal regions spanning 10 degrees ($40°$–$50°$, $50°$–$60°$ and $60°$–$70°$). The relatively large zones ensure that the phenology curves are produced from enough values while allowing significant latitudinal variations for each vegetation class.

The derived ensemble phenology curves are subsequently smoothed with a simple three-point smoothing algorithm

$$N_{se}(t) = 0.5N_e(t) + 0.25\left[N_e(t-1) + N_e(t+1)\right] \tag{1}$$

to avoid jigsaw-like features especially during the winter months. The subscripts "se" and "e" indicate smoothed and raw ensemble values, respectively, while t indicates time and N is short for NDVI.

For gap filling of the multi-year average time series, we applied the smoothed, ensemble phenology curve trends instead of actual values, assuming that the majority of pixels within the same landuse class and region show the same phenological pattern. The method requires that at least one value in the individual time series exist. The filling is done in several steps. Initially, both backward and forward filling are attempted starting from day 201 towards either day 001 or 361. Afterwards, filling from day 001 to day 361 and backwards is done to fill values that were not filled in the first pass. The method ensures that potential jumps from filling only occur during the December–January transition and that areas with very little information about the vegetation seasonality, such as the mountainous regions in the Alps and Pyrenees and northern Scandinavia, obtain full phenology curves based on the ensemble mean seasonalities. After the filling, we applied the smoothing procedure on all of the pixel time series. The final appearance of a randomly selected climatological curve (solid) after filling and smooth-

ing has been applied to the initially discountinous NDVI multi-year average (dashed) is shown in Figure 2.

2.2.4 Cyclic conditions

We used a linear algorithm to ensure cyclic conditions at the December–January transition only allowing gradients less or equal to 0.1. The cyclic filter was particularly in use above $60°$N where vegetation impacts on modeling results anyway are minimal due to low radiation and persistent snow cover conditions. If a gradient larger than 0.1 and less than 0.2 was detected, a linear interpolation between day 361 and day 33 replaced the original phenology curve. For intervals larger than 0.2, we set the December-January transition to 0.1 and scaled the remaining values linearly between day 1 and 33. The procedure was selected in order to maintain the curve minimum in the February-March period, as is typically observed for the region. Finally, pixels solely consisting of missing values were assigned with smoothed ensemble phenology curves matching the pixel landuse class and zone. Less than 0.0002% of the pixels was filled in this manner.

2.2.5 Single-year representation

Since we can exploit the added pixel-level information provided by the climatology, the procedure to obtain an explicit filled 2006 NDVI time series is much simpler than for the multi-year climatology. As before, we only use good quality data (QC= 0) from 2006 but neglect the local correction as applied for the climatology. Gap filling is performed with trends from the climatological time series and is thus primarily based on pixel-level phenology curves and not on zonally averaged ecosystem-dependent curves. Finally, the smoothing algorithm was applied to the specific 2006 NDVI values.

2.2.6 Derivation of green vegetation fraction

The NDVI climatology or the annually filled representation of NDVI can be converted into GVF in several ways using

$$\text{GVF} = \left(\frac{N - N_s}{N_v - N_s}\right)^p \tag{2}$$

where N represents the time-varying NDVI value at each grid cell, N_v and N_s represent NDVI values at full green vegetation cover and at bare soil, respectively, and p is a constant. We use the method described by Zeng et al (2000) where N_v is considered a function of vegetation type and both N_v and N_s are varying within each year. Since we consider a limited area, N_s is regionally defined and computed to $N_s \approx 0.05$ for all data sets. N_v was found to vary between 0.75 and 0.90 with slightly higher values in the 2006 specific NDVI time series. The calculated values are close to what others have found (Montandon and Small 2008).
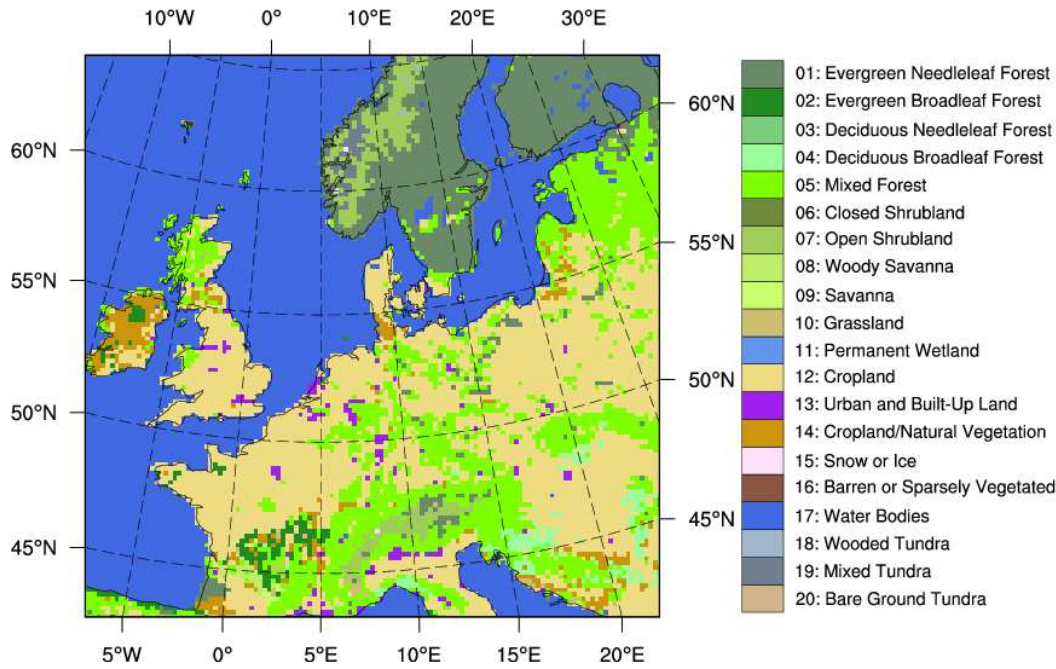
Fig. 3 IGBP landuse classes in the 18km WRF domain

The AVHRR GVF data was obtained using the linear approach and by assuming N_v and N_s as spatially and temporally constant values. The NDVI values were globally defined and estimated to $N_v = 0.52$ and $N_s = 0.04$ (Gutman and Ignatov 1998). We decided to test both the linear and the quadratic formulation for our single-year representations.

3 Model and verification data

3.1 Numerical model

We used the WRF ARW model version 3.3.1 maintained by the National Center for Atmospheric Research (NCAR) for our numerical simulations (Skamarock et al 2008). An overview of the selected physical parameterizations as well as forcing data are given in Table 1.

Sea surface temperature is described by the Optimum Interpolation Sea Surface Temperature (OISST) at $0.25°$ grid spacing and daily resolution. Initial and lateral boundary conditions are obtained from the Climate Forecast System Reanalysis (CFSR) data at $0.5°$ horizontal resolution made available by National Centers for Environmental Prediction (NCEP). Grid-nudging from the Four-Dimensional Data Assimilation (FDDA) system is used on temperature, moisture and wind components above the lowest 15 model levels, but excluded within the PBL for temperature and moisture. The nudging technique ensures that upper-air model predictions do not drift too far away from the reanalysis conditions. We use 41 vertical levels and horizontal grid intervals of 18 km and create continuous.

The High-Resolution Land Data Assimilation (HRLDAS) system was used for initial spinup of soil moisture and soil temperature. The HRLDAS system was adapted to use 3-hourly Global Land Data Assimilation System (GLDAS) data and ran for a period of two years prior to simulation start, on 1 January 2006. The HRLDAS system used the Noah LSM with the AVHRR GVF data and all runs were initialized with the predicted soil state.

The IGBP land cover distribution and the extent of our computational domain are shown in Figure 3. The 1 km grid spacing of the land cover data was interpolated by the WRF Preprocessing System (WPS version 3.3) (Skamarock et al 2008) to 18 km using the dominant vegetation type to determine the classification at each pixel. Thus, 91.47% of all pixels belong in four land cover classes; 39.58% Water, 26.35% Croplands, 15.12% Mixed Forest (MF) and 10.42% Evergreen Needleleaf Forest (ENF). ENFs are mainly defined to northern areas such as Sweden, Norway and Finland while MFs are found in areas such as the Baltics, Scotland, Germany, Slovakia and near the Alps. Croplands mainly exists south of $58°N$.

The MODIS GVF data, which were described in section 2, were linearly interpolated into daily files and, additionally, fields with yearly minimum and maximum vegetation fractions were computed. The latter files are important for correct scaling of LAI, roughness, emissivity and albedo and are different for each version of the GVF data. The WPS system horisontally interpolated all fields to 18 km grid spacing to preserve consistency with the interpolated IGBP land

Table 1 Overview of the physical packages and forcing data used in our simulations.

Parameterization	Name	Reference
Land surface	Noah	Chen and Dudhia (2001)
Surface layer	Eta	Janjic (1996)
Planetary Boundary Layer	MYJ	Janjic (2002)
Longwave radiation	RRTM	Mlawer et al (1997)
Shortwave radiation	Duhia	Dudhia (1989)
Microphysics	WSM5	Hong et al (2004)
Cumulus	Kain-Fritsch	Kain (2004)
Forcing data	Name	Reference
Initial and Boundary	CFSR	Saha et al (2010)
Land surface spinup	GLDAS	Chen et al (2007)
Sea surface state	OISST	Reynolds et al (2007)
Grid nudging	q,T,u,v	Stauffer and Seaman (1990)

cover data. Minor changes to the WRF model were required to include the new GVF files.

3.2 E-OBS and GPS data

To validate the model performances, we used the European daily high-resolution gridded dataset (E-OBS, v5.0) developed for climate change studies and for validation of regional climate models (Haylock et al 2008). It is based on the European Climate Assessment and Data network of measuring stations (ECA&D) and include minimum, maximum and mean daily 2m temperature, as well as daily precipitation. The mean daily 2m temperature in E-OBS is calculated as $(T_{min}+T_{max})/2$ where T_{min} and T_{max} are obtained as being the most extreme values at hour 00, 06, 12 or 18. About 2000 stations were used for developing E-OBS with the highest station densities found in the UK, Benelux and the Alps.

Several issues with E-OBS have been identified by comparison to observational data sets with higher station density (Hofstra et al 2009; Kyselý and Plavcová 2010). The main problems are related to interpolation of station measurements in areas with limited station density or in complex terrains, where the station measurements are not representative of their surroundings. For instance, Kyselý and Plavcová (2010) found that temperature extremes in the Czech Republic was substantially understimated in E-OBS with cold extremes being too warm and warm extremes being too cold. The interpolation results in regional biases in both temperature and precipitation but is particularly severe for extreme values. Despite of these problems, E-OBS was considered the best solution for verification of our numerical simulations.

In addition to E-OBS, we use precipitable water data measured by a permanent GPS station, PTBB, located in central Germany (Braunschweig, Neidersachsen) to verify

temporal variations in water vapor in the WRF model simulations (Bruyninx 2004).

4 Seasonality comparison

Vegetation seasonalities for forest types represented in the WRF domain are shown in Figure 4. In addition to ENF and MF which were defined in section 3.1, we use EBF and DBF as abbreviations for evergreen broadleaf forest and deciduous broadleaf forest, respectively. The AVHRR GVF climatology and the MODIS GVF climatology are indicated by Clim-A and Clim-M, respectively, while the linear and quadratic single-year MODIS GVF products are indicated by 2006-L and 2006-Q, respectively.

Large differences in the representations of vegetation fraction for ENF are shown in Figure 4a. Clim-M, 2006-L and 2006-Q show higher vegetation fractions during the whole annual cycle compared to Clim-A, with the highest values indicated by the linear methods. The vegetation fraction of Clim-M and 2006-L range between 50–90% while Clim-A and 2006-Q range between 5–70% and 25–85%, respectively. The intraannual variability between all representations is similar indicating that figures with LAI, roughness, emissivity and albedo will be very similar as well (not shown).

Vegetation fractions for EBF are shown in Figure 4b. Clim-M and 2006-L show little annual variation ranging from 70–90% while Clim-A and 2006-Q indicate larger variations between 40–90% and 50–85%, respectively. A decrease in GVF during June–July followed by an increasing trend during August–September for all MODIS data is not observed in Clim-A. The majority of EBF sites are located in southern France (see Figure 3), a region that was also severly affected by the heat wave 2003 (Rebetez et al 2009). The difference in intraannual variability reflect stresses on EBF due to heat and drought conditions. This is also reflected in LAI where Clim-A show higher summer values compared
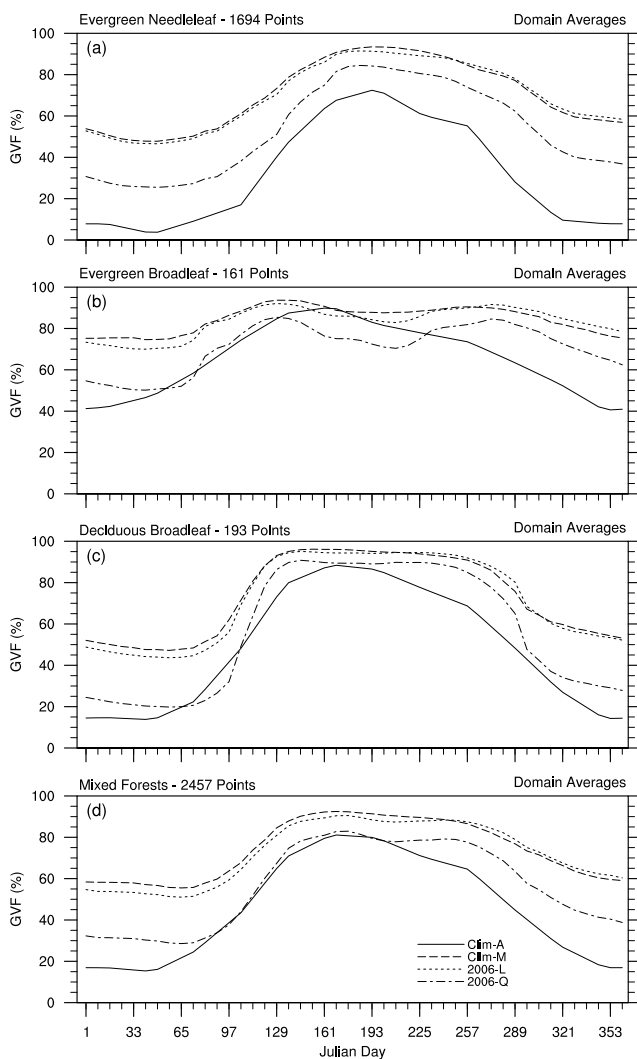
Fig. 4 Comparison of domain averaged GVF (%) for (a) ENF, (b) EBF, (c) DBF and (d) MF at 18 km resolution. Solid lines represent Clim-A, the long dashed, short dashed and long-short dashed lines represent Clim-M, 2006-L and 2006-Q, respectively

to those derived from the MODIS data. The opposite occur in the autumn where lower LAI values are found in Clim-A (not shown).

Figure 4c-d show vegetation seasonalities for DBF and MF. Clim-M and 2006-L show the highest values while Clim-A and 2006-Q compare well in terms of maximum and minimum vegetation fraction. Summer values range between 75–95% while winter and late autumn values range between 15–60%, with lowest values shown by Clim-A and 2006-Q. Clim-A shows slowly evolving vegetation cover for DBF while more rapid growth and decaying trends are shown by Clim-M, 2006-L and 2006-Q. Additionally, a prolonged growth period (April–October) for both DBF and MF is indicated in the GVF data derived from MODIS compared to Clim-A.
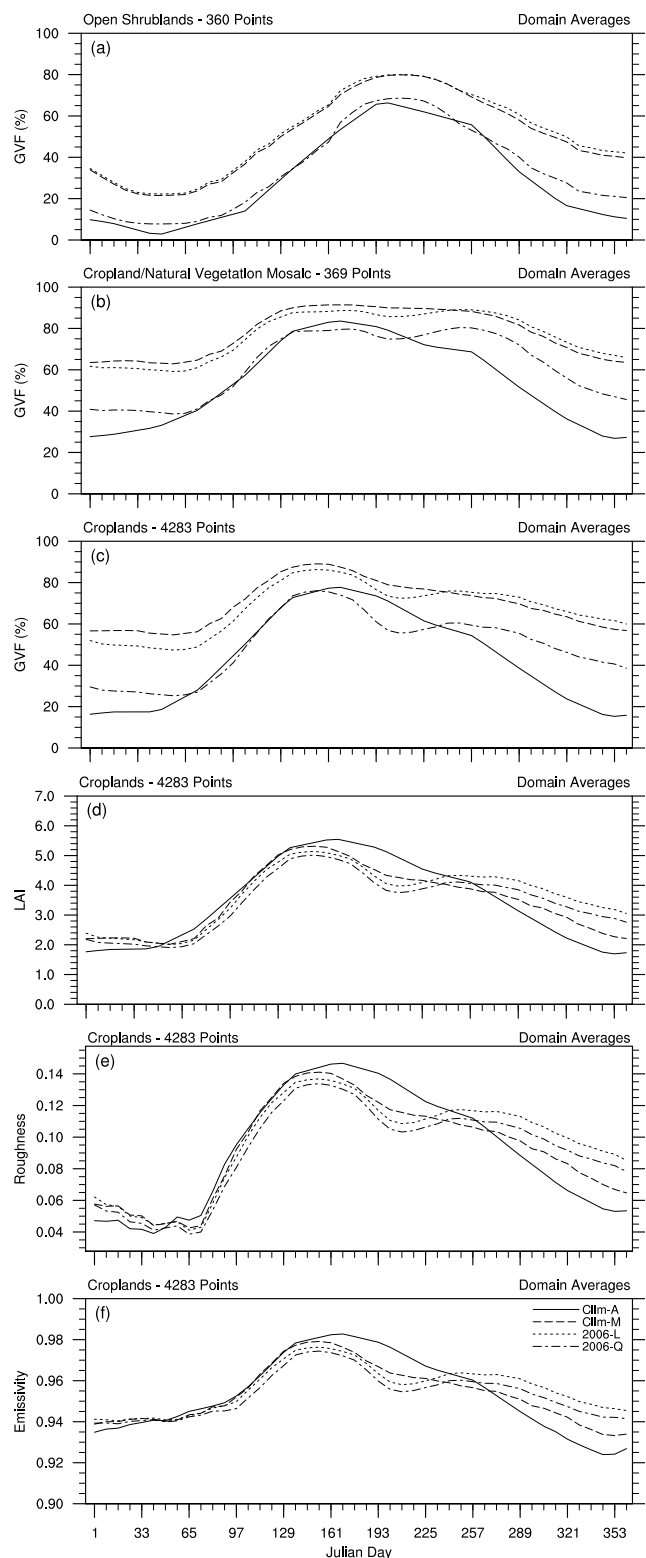
Fig. 5 Comparison of domain averaged GVF (%) for (a) open shrublands, (b) cropland/natural vegetation and (c) croplands. In addition, domain averaged LAI (d), roughness (e) and emissivity (f) for croplands sites are shown. Otherwise similar to Figure 4

The seasonal evolution of GVF for open shrublands (OS), cropland/natural vegetation (CN) and croplands (CL) together with LAI, roughness and emissivity for CL is shown in Figure 5a-f. The intraannual variability for OS is very similar between all GVF representations with the highest fractions shown by Clim-M and 2006-L, Figure 5a. This is somewhat misleading since OS show significant latitudinal dependency. GVF from MODIS data results in higher vegetation fractions over Scandinavia compared to Clim-A during the entire annual cycle while Clim-A show higher summer vegetation fraction over the Alps and slightly lower during the winter (not shown).

Figure 5b show vegetation fractions representing CN but indicate very similar development to MF shown in Figure 4d. It reflects that the majority of CN sites is located in the vicinity of MFs while points classified as CN but surrounded by CL resemble the vegetation seasonality of CL better (not shown).

Vegetation fractions indicating CL seasonalities are shown in Figure 5c. Higher values are consistently shown by Clim-M and 2006-L compared to Clim-A and 2006-Q and range between 50–90% while a range of 15–75% is shown by Clim-A and 2006-Q. Clim-A and 2006-Q compare well during the first half seasonal cycle but show significant difference in seasonal development during the last part of the year. A large decrease in GVF during June–July is shown by 2006-Q compared to the climatologies indicating either early harvesting or stresses related to drought and heat. 2006-Q show a decrease in GVF from about 75% to 50% but zonal averages between 50°–60°N reveal even larger decreases (not shown). A similar decrease, although smaller in magnitude, is observed for 2006-L.

LAI, roughness and emissivity for CL are shown in Figure 5d-f to show how differences in intraannual variability is transferred to the scaled parameters in WRF. Almost identical values are found for the parameters until June while large differences are found during summer and autumn. The low summer vegetation fraction accompanied by lowering the LAI value, as shown by 2006-Q, significantly reduces the potential for transpiration in WRF over croplands.

The spatial distribution of GVF during the heat wave event in July 2006 is investigated in Figure 6. The squares (represented by letters "**a**" and "**b**") indicate areas selected for statistical comparison between the numerical simulations and observed values represented by E-OBS (see section 5). As expected, Clim-M and 2006-L show much higher vegetation fractions, especially in forested areas, compared to Clim-A while croplands sites are more varied. 2006-Q show much lower vegetation fractions for croplands sites compared to the other GVF representations, especially within the squares over France and Poland and in the UK. The colors indicate differences of the order of 50% in some areas between Clim-A and 2006-Q. Considering that 2006-Q
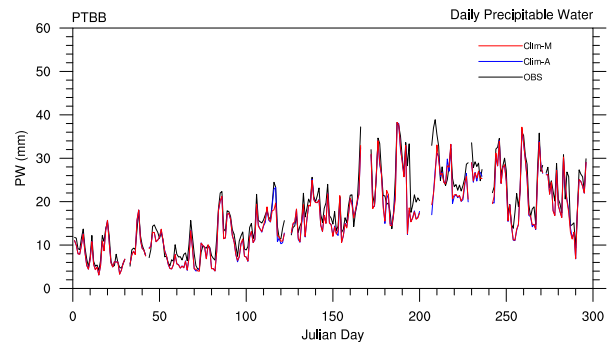

Fig. 7 Comparison of the precipitable water (PW) at station PTBB located in central Germany (52.30°N, 10.46°E). Observed PW is represented in black while predicted PW is indicated in blue and red for Clim-A and Clim-M, respectively.

show similar seasonal development during springtime compared to Clim-A, see Figure 5, it is clearly seen how extreme events or changes in management pratice can alter the appearance of GVF.

5 Numerical results

To check the validity of our modeling setup, numerical results of precipitable water (PW), a vertically integrated variable, was compared to observed data obtained from a GPS station in central Germany. The location is close to the center of our domain at 52.30°N, 10.46°E and thus not influenced by the boundary conditions. Only observed and predicted PW from numerical simulations with Clim-A and Clim-M are shown since nearly identical results are obtained using 2006-L and 2006-Q. A very good correspondance between modeled and observed PW during the whole year is seen (Figure 7). The differences between the modeled PWs are small and indicate that our simulations describe the atmospheric moisture conditions equally well.

The accumulated precipitation fields during March, April and May obtained from Clim-A and Clim-M are compared to observed precipitation from E-OBS in Figure 8. 2006-L and 2006-Q are excluded in the comparison since their precipitation fields only deviate slightly from those obtained by the climatologies. Almost identical accumulated precipitation amounts are found comparing Clim-A and Clim-M and the precipitation patterns compare well to E-OBS, although many regions show higher predicted accumulated values. Other periods of the annual cycle show similar trends (not shown), thus precipitation is largely controlled by the grid nudging technique and not influenced by changes in GVF.

Mean 2m temperature fields during March, April and May are shown in Figure 9 for Clim-A, Clim-M and E-OBS. Again, 2006-L and 2006-Q are excluded from the comparison due to their similarity with the climatologies. Clim-A and Clim-M show very similar temperature patterns with
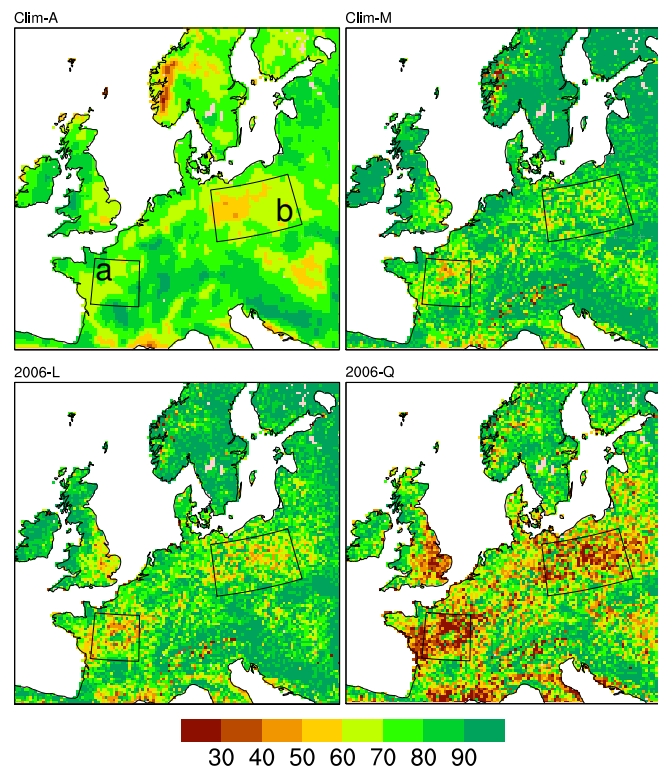
Fig. 6 Comparison of averaged GVF (%) from Clim-A, Clim-M, 2006-L and 2006-Q during July 2006. The areas indicated with squares over (**a**) France and (**b**) Poland are used for error statistics in Table 2.
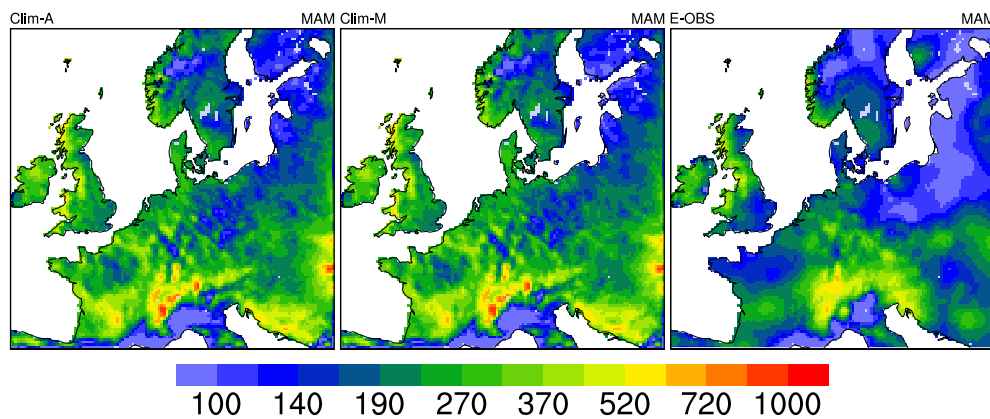

Fig. 8 Accumulated precipitation (mm) for Clim-A, Clim-M and E-OBS during March, April and May, 2006

only minor differences over the UK, France and Germany. The patterns are consistent with E-OBS although cold biases of 1–4K are observed throughout the domain. The largest biases are found in the northern regions, especially over Finland, but decrease towards the south. Minimum and maximum 2m temperature show similar spatial trends and biases (not shown).

Instead of showing similar figures as above for the summer period, the following investigations are restricted to the heat wave period in July. Figure 10 shows averaged mean 2m temperatures (K) for all simulations and E-OBS. The

largest differences between the simulated temperatures are seen in areas containing mostly croplands, hence, the northern regions with mainly forest show uniform temperatures. Clim-A shows higher temperatures over Poland and Hungary while lower temperatures are found in central France compared to Clim-M. 2006-L compare well with Clim-M as expected but show higher temperatures over Poland. The warmest temperatures are shown by 2006-Q compared to the other simulations, especially in central France. All simulations still indicate a cold bias compared to E-OBS.
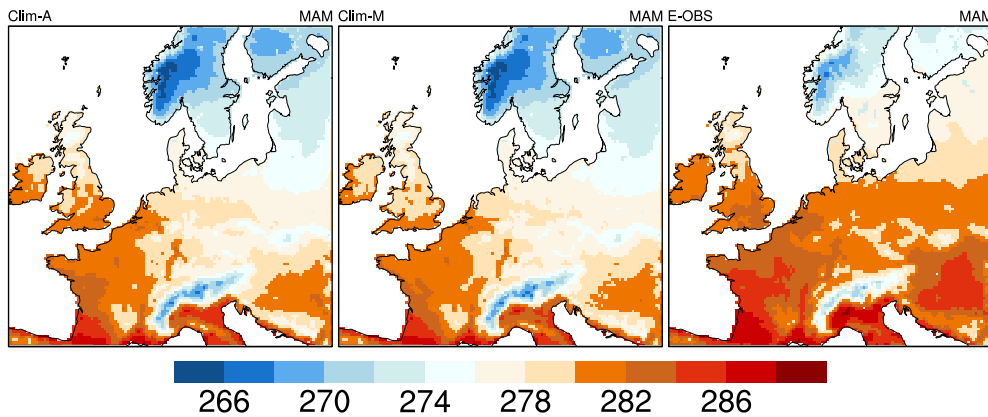
Fig. 9 Mean 2m temperature (K) for Clim-A, Clim-M and E-OBS during March, April and May, 2006. Mean temperatures are calculated from $(T_{min}+T_{max})/2$
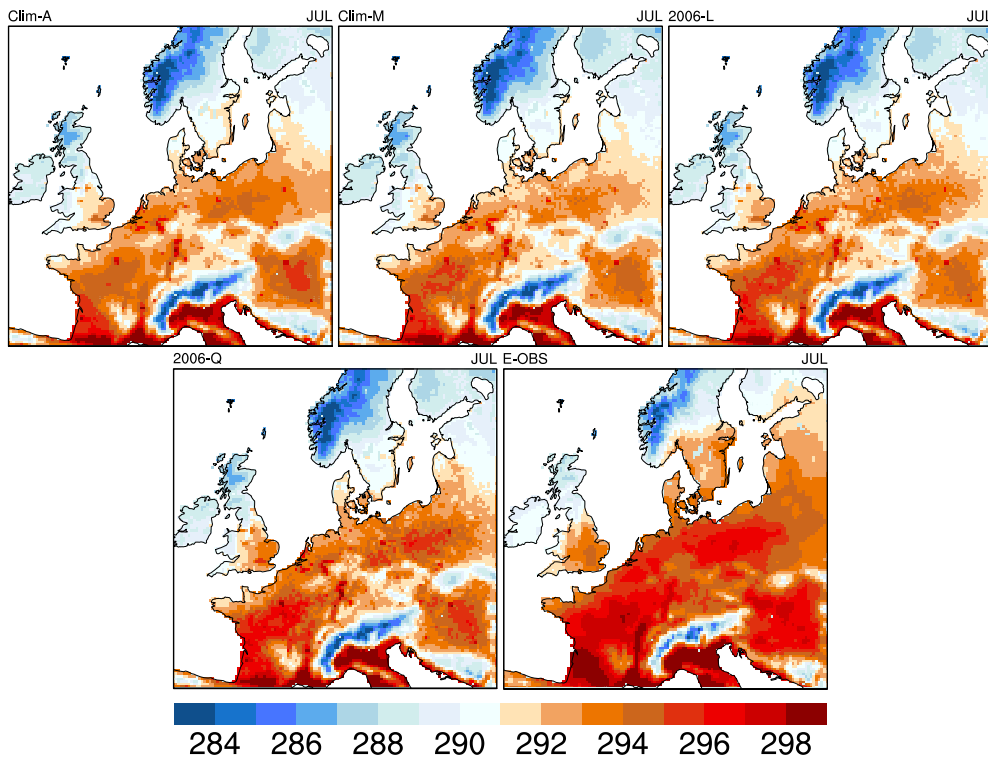

Fig. 10 Mean 2m temperature (K) during July 2006 for Clim-A, Clim-M, 2006-L (upper panel), 2006-Q and Eobs (lower panel). Temperatures are calculated from $(T_{min}+T_{max})/2$

Differences between the simulated mean 2m temperatures during July reflect changes in their minimum and maximum 2m temperatures as well. The differences are shown in Figure 11 for the 2006 specific simulations and Clim-A. We did not include Clim-M since the appearance was very similar to the difference shown between 2006-L and Clim-A. 2006-L results in warmer minimum and maximum temperatures over France and southern UK compared to Clim-A, while mostly lower temperatures are indicated in the northern and eastern regions. The differences range between 0–

2K. Much larger temperature differences are shown by 2006-Q compared to Clim-A. The northern forested regions show slightly lower temperatures for both minimum and maximum temperature while the remaining areas show higher temperatures. In some cases more than 2K.

Coefficients of determination (R^2), biases and root mean square errors (RMSEs) of simulated daily mean, maximum and minimum temperatures against E-OBS values, shown in Table 2, were calculated. The statistics are derived separately in the areas indicated in Figure 6 by letters "**a**" and
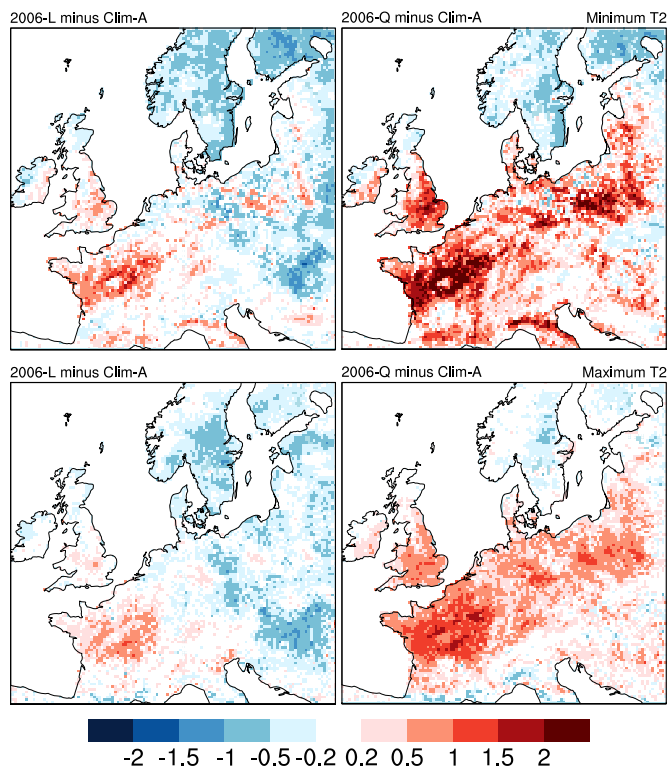
Fig. 11 Difference plots of 2006-L (left column), 2006-Q (right column) minus Clim-A for averaged daily minimum 2m temperature (upper row) and maximum daily 2m temperature (lower row) during July 2006. Units in kelvin

Table 2 Coefficients of determination, Bias and RMSE of 2006 July daily mean, maximum and minimum temperatures from Clim-A, Clim-M, 2006-L and 2006-Q against E-OBS values over the areas enclosed by squares in Figure 6 and for the whole domain. The squares are named after their location over France and Poland. The best errror statistics for each area are indicated in bold. Units are in Kelvin

France	Mean			Max			Min		
	R^2	Bias	RMSE	R^2	Bias	RMSE	R^2	Bias	RMSE
Clim-A	0.77	−2.78	2.97	0.82	−3.45	3.73	0.62	−2.17	2.55
Clim-M	0.80	−2.57	2.75	0.84	−3.30	3.56	0.64	−1.88	2.31
2006-L	0.81	−2.32	2.53	0.84	−3.06	3.34	**0.66**	−1.63	2.12
2006-Q	**0.82**	**−1.53**	**1.88**	**0.86**	**−2.37**	**2.69**	0.64	**−0.75**	**1.71**
Poland	R^2	Bias	RMSE	R^2	Bias	RMSE	R^2	Bias	RMSE
Clim-A	0.75	−2.51	2.85	0.70	−3.56	3.99	**0.58**	−1.43	2.37
Clim-M	0.75	−3.17	3.44	0.70	−4.22	4.59	0.57	−2.09	2.84
2006-L	0.75	−2.73	3.05	0.70	−3.80	4.20	0.57	−1.63	2.55
2006-Q	**0.78**	**−1.91**	**2.33**	**0.73**	**−3.04**	**3.49**	0.57	**−0.75**	**2.14**
Domain	R^2	Bias	RMSE	R^2	Bias	RMSE	R^2	Bias	RMSE
Clim-A	0.82	−2.14	2.13	0.82	−2.75	2.69	0.67	−1.52	2.11
Clim-M	0.80	−2.41	2.33	0.80	−3.02	2.89	0.66	−1.79	2.29
2006-L	0.81	−2.28	2.24	0.81	−2.90	2.80	0.67	−1.66	2.21
2006-Q	**0.83**	**−1.87**	**1.95**	**0.83**	**−2.50**	**2.50**	**0.69**	**−1.22**	**2.01**

"**b**", and over the entire model domain. The areas were selected because they show the largest change in GVF between the different data sets. All GVF representations show similar R^2 values with lower values found for minimum temperature. Both bias and RMSEs are significantly improved by 2006-Q compared to Clim-A showing improvements between 20%–45% for mean temperature over Poland and France. Similarly, maximum temperature biases are reduced by 14%–31% while minimum temperature biases are reduced with more than 45%. Both Clim-M and 2006-L show lower biases and RMSEs compared to Clim-A over France while poorer performance are obtained over Poland. The statistics show that consistent improvements are obtained using the quadratic method to derive GVF while the linear approach show mixed results. Simulated precipitation patterns did not show any sensitivity to changes in vegetation fractions and only small differences in accumulated amounts were found.

Temperature results during fall showed similar performances between the model simulations, still with lower temperatures compared to E-OBS. The best performance was shown by Clim-A although the difference to 2006-Q was small.

6 Discussion

Although the newly created GVF products show significant differences throughout the year, cf. Figure 4 and 5, there is little difference between the temperature predictions during the winter due to low radiation conditions. The low vegetation fractions shown by Clim-A for ENF are not realistic since more constant seasonality is expected (Miller et al 2006). With this in mind, it is therefore possible that the MODIS-derived GVF products are closer to reality (though 2006-Q possibly still indicates too low values). A comparison of the zonal medians between 50°N–60°N and 60°N–70°N for the new GVF products reveals higher winter vegetation fractions for the southern area, suggesting that the ecosystem-dependent filling, mainly used above 60°N, may play a major role in further improvement of the winter vegetation values.

The temperature differences among the simulations, indicated by Table 2, are related to changes in the surface energy distribution. Figure 12 shows the differences in sensible and latent heat fluxes between the 2006 specific GVF products and Clim-A during July. Many of the areas covered by croplands show 30 Wm^{-2} less latent heat flux for 2006-Q compared to Clim-A, while sensible heat flux is 20 Wm^{-2} higher. The residual energy was largely converted into soil heat fluxes (not shown). Similar patterns are seen between 2006-L and Clim-A though the differences are smaller in magnitude. The higher daytime temperatures, specifically shown by 2006-Q, are directly related to the increased sensible heat flux while higher nighttime temperatures occur

due to increased soil temperature leading to higher nighttime ground heat flux into the atmosphere. Since we neither observed large differences in the rootzone soil moisture availability, precipitation nor cloud cover, the altered surface energy distribution is mainly due to direct changes in GVF.

The quadratic MODIS NDVI to GVF relation clearly shows the best performance in terms of temperature simulation compared to the linear relationship at low resolution WRF simulations. However, this does not necessarily ensure better results at high resolution. The very similar range in vegetation fractions shown by the low resolution AVHRR data and the high resolution quadratic GVF data, aggregated to low resolution through WPS, is encouraging. It suggests that good performance across spatial scales might be expected. Furthermore, the quadratic NDVI to GVF relation was recently recommended to avoid large overestimations of GVF due to underestimation of bare soil NDVI (Montandon and Small 2008). They showed that the maximum error would occur for NDVI values in the range of $0.2 \leq N \leq 0.4$ which typically are found during winter or spring e.g. for croplands. This critical range was also reached during the 2006 summer heat wave for croplands; thus overestimation of vegetation fraction during this period is minimized with the quadratic relationship. The use of local scenes was also recommended to minimize underestimation of N_s as was done in this study. Therefore, the results presented here combined with their findings suggest that the quadratic equation should be used for both spatially low and high resolution simulations in WRF.

The cold bias shown by the WRF model compared to E-OBS was also reported in a recent study (García-Díez et al 2012). The atmospheric conditions during 2002 were simulated using the ERA-Interim reanalysis data as boundary and initial conditions and by applying different PBL schemes. The simulations were done in a reforecast mode using 12 hours of spin-up. This study ruled out the CFSR data and the MYJ PBL scheme as causes of the overall temperature bias in our study. The main problem could very well be related to the radiative balance (García-Díez et al 2012; Manning et al 2010) which was only slightly changed by updating the GVF data. However, some of the biases found in García-Díez et al (2012) might be related to inadequate description of vegetation during the summer period and to the soil moisture reinitialization. We propose that future investigations of the impact of remotely sensed albedo in WRF/Noah should be carried out using our approach. The advantages are that the grid nudging technique minimize changes in precipitation and cloud cover and the continuous simulation avoid reinitialization of soil moisture that is important for the surface energy balance.

The longer growing season indicated by the new GVF data is perhaps a result of higher autumn temperatures over the northern latitudes during the last two decades which, ad-
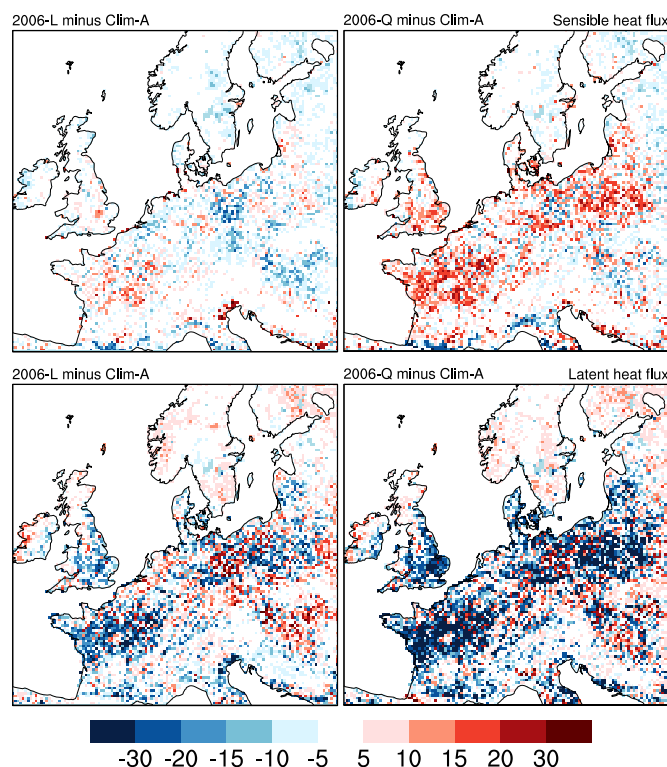
Fig. 12 Difference plots of 2006-L (left column), 2006-Q (right column) minus Clim-A for July 2006 averaged sensible heat fluxes (upper row) and latent heat fluxes (lower row). The fluxes are defined as positive upwards in units of Wm^{-2}

ditionally, have lead to increases in photosynthesis and respiration (Piao et al 2008). However, the increased climate variability predicted by climate models (Seneviratne et al 2006), could significantly alter the interannual variability of GVF suggesting that updated land cover characteristics will be more important for climate predictions in the future. A key process in the approach presented in this paper, is the development of a NDVI climatology. Besides introducing a robust way of treating missing data and bad pixel values, it offers attractive perspectives for future studies. The new NDVI climatology ensures an efficient way to fill annual GVF data sets. Furthermore, the approach applied in this study could be expanded to a near real-time GVF product that would improve temperature predictions during future extreme heat wave events.

7 Conclusion

A statistically robust MODIS-derived NDVI climatology, reflecting recent landuse and climatic changes, was derived to enable computation of updated GVF information. Existing and novel data-processing techniques were applied on 10 years of NDVI composites to ensure high quality of the climatology. A GVF climatology and two single-year representations of GVF, using both linear and quadratic NDVI to

GVF relations, were derived and used in WRF model simulations over Europe during the 2006 heat wave year at 18 km grid spacing.

Comparison of annual GVF timeseries for the most common land use classes in the domain showed that linearly derived GVF products generally result in higher vegetation fractions compared to the AVHRR GVF data. Wintertime vegetation fractions for deciduous broadleaf forest, mixed forest and croplands are likely overestimated while high vegetation fractions for evergreen needleleaf forests are realistic due to their "evergreen" classification. The 2006 quadratic GVF product shows very good agreement with the magnitude and annual range of the AVHRR data while showing higher vegetation fractions for evergreen needleleaf forest during the winter. Vegetation stresses related to the 2006 heat wave or changes in management practice for croplands are clearly indicated by the 2006 specific GVF products. Additionally, prolonged autumnal growth periods are indicated by the new GVF products for mainly deciduous forests types.

The output from the numerical simulations was compared to E-OBS daily gridded observational data. Verification included mean, minimum and maximum 2 m temperatures. Comparison during the spring showed that all simulations produced equally good results. However, temperatures during July were consistently improved by the 2006

quadratic GVF product compared to E-OBS, reducing the mean temperature bias by 20–45% in areas severely affected by the heat wave. The reduction in bias over the whole domain was 10%. Improvements for minimum temperature were larger than those obtained for maximum temperature. The linearly derived GVF products showed varying results and did not perform as good as the quadratic GVF product during the heat wave period. This study shows that updated land cover information during heat wave events or droughts is required to reproduce the extreme temperature predictions using the WRF model and, in addition, that land cover information from MODIS NDVI should be produced using the quadratic equation.

References

Bruyninx C (2004) The EUREF Permanent Network: a multidisciplinary network serving surveyors as well as scientists. Geoinformatics 5(7):D21,101

Chen F, Dudhia J (2001) Coupling an advanced land surface-hydrology model with the Penn State-NCAR MM5 modeling system. part ii: Preliminary model validation. Mon Weather Rev 129(4):587–604

Chen F, Manning K, Lemone M, Trier S, Alfieri J, Roberts R, Tewari M, Niyogi D, Horst T, Oncley S, Basara J, Blanken P (2007) Descripton and Evaluation of the Characteristics of the NCAR High-Resolution Land Data Assimilation System. J App Meteorol and Climatology 46:694–713

Chen J, Jonsson P, Tamura M, Gu Z, Matsushita B, Eklundh L (2004) A simple method for reconstructing a high-quality NDVI time-series data set based on the Savitzky-Golay filter. Remote Sens Environ 91(3-4):332–34

Della-Marta PM, Haylock MR, Luterbacher J, Wanner H (2007) Doubled length of western European summer heatwaves since 1880. J of Geophys Res 112:D15,103, DOI 10.1029/2007JD008510

Didan K, Huete A (2006) Modis Vegetation Index Product Series: Collection 5 Change Summary. Tech. rep.

Dudhia J (1989) Numerical Study of Convection Observed during the Winter Monsoon Experiment Using a Mesoscale Two-Dimensional Model. J Atmos Sci 46(20):3077–3107

Friedl MA, McIver DK, Hodges JCF, Zhang XY, Muchoney D, Strahler AH, Woodcock CE, Gopal S, Schneider A, Cooper A, Baccini A, Gao F, Schaaf C (2002) Global land cover mapping from MODIS: algorithms and early results. Remote Sens Environ 83:287–302

García-Díez M, Fernández J, Fita L, Yague C (2012) Seasonal dependence of WRF model biases and sensitivity to PBL schemes over Europe. QJR Meteorol Soc DOI 10.1002/qj.1976

Gu J, Li X, Huang C, Okin G (2009) A simlified data assimilation method for reconstructing time-series MODIS NDVI data. Adv Space Res 44(4):501–59

Gutman G, Ignatov A (1998) The derivation of the green vegetation fraction from NOAA/AVHRR data for use in numerical weather prediction models. International Journal of Remote Sensing 19(8):1533–1543, DOI 10.1080/014311698215333

Haylock MR, Hofstra N, Klein Tank AMG, Klok EJ, Jones PD, New M (2008) A Europen daily high-resolution gridded data set of surface temperature and precipitation for 1950-2006. J Geohys Res 113(D20):D20,119

Hofstra N, Haylock M, New M, Jones P (2009) Testing E-OBS European high-resolution gridded data set of daily precipitation and surface temperature. J Geophys Res 114(D21):D21,101, DOI 10.1029/009JD011799

Hong S, Lakshmi V, Small E, Chen F, Tewari M, Manning K (2009) Effects of vegetation and soil moisture on the simulated land surface processes from the coupled WRF/Noah model. J Geophys Res 114, DOI 10.1029/208JD011249

Hong SY, Dudhia J, Chen SH (2004) A revised approach to ice-microphysical processes for the bulk parameterization of cloud and precipitation. Mon Weather Rev 132(1):103–120

Janjic ZI (1996) The Surface Layer in the NCEP Eta Model. Am Met Soc pp 354–355

Janjic ZI (2002) Nonsingular implementation of the Mellor-Yamada level 2.5 scheme in the NCEP Meso model. Office Note 437, NCEP

Jiang L, Kogan F, Guo W, Tarpley JD, Mitchell K, Ek M, Tian Y, Zheng W, Zou C, Ramsay B (2010) Real-time weekly global green vegetation fraction derived from advanced very high resolution radiometer-based NOAA operational global vegetation index (GVI) system. J Geophys Res 115, DOI 10.1029/2009JD013204

Kain JS (2004) The Kain Fritsch Convective Parameterization: An Update. J Appl Meteorol 43(1):170–181

Kyselý J, Plavcová E (2010) A critical remark on the applicability of E-OBS European gridded temperature data set for validating control climate simulations. J Geophys Res 115, DOI 10.1029/2010JD014123

Lakshmi V, Hong S, Small E, Chen F (2011) The influence of the land surface on hydrometeorology and ecology: New advances from modeling and satellite remote sensing. Hydrology Research 42(2-3):95–112, DOI 10.2166/nh.211.071

Lovell J, Graetz R (2001) Filtering the pathfinder AVHRR Land NDVI data for Australia. Int J Rem Sens 13(22):2649–2654

Ma M, Veroustraete F (2004) Reconstructing pathfinder AVHRR Land NDVI time series data for the Northwest of China. AdvSpace Res 37(3-4):835–80

Manning K, Tewari M, Barlage M, Chen F, Salamanca F, Martill A (2010) Updates to the Noah LSM in WRF version 3.2. In *11th WRF Users' Workshop*, NCAR, Boulder, CO

Miller J, Barlage M, Zeng X, Wei H, Mitchell K, Tarpley D (2006) Sensitiviy of the NCEP/Noah land surface model to the MODIS green vegetation fraction data set. Geophys Res Lett 33, DOI 10.1029/2006L026636

Mlawer EJ, Taubman SJ, Brown PD, Iacono MJ, Clough SA (1997) Radiative transfer for inhomogeneous atmospheres: RRTM, a validated correlated-k model for the longwave. J Geophys Res 102(D14):16,663–16,682, DOI 10.1029/97JD00237

Montandon L, Small E (2008) The impact on soil reflectance on the quantification of the green vegetation fraction from NDVI. Rem Sens of Environ 112:1835–1845

Montandon L, Fall S, Pielke, RASr, Niyogi D (2011) Distribution Of Landscape Types In The Global Historical Climatology Network. Earth Interactions 15:1–22

Moody EG, King MD, Platnick S, Schaaf C, Gao F (2005) Spatial complete global spectral surface albedos: value-added datasets de-

rived from Terra MODIS land products. IEEE Trans Geosci Remote Sens 43(1):144–158

P J, Eklundh L (2002) Seasonalty extraction by function fitting to time-series of satellite sensor data. IEEE Trans Geosci Remote Sens 40(8):1824–183

Piao S, Ciais P, Friedlingstein P, Peylin P, Reichstein M, Luyssaert S, Margolis H, Fang J, Barr A, Chen A, Grelle A, Hollinger DY, Laurila T, Lindroth A, Richardson AD, Vesala T (2008) Net carbon dioxide losses of northern ecosystems in response to autumn warming. Nature 451(7174):49–52, DOI 10.1038/nature06444

Pielke R (2001) Influence of the spatial distribution of vegetation and soils on the prediction of cumulus convective rainfall. Rev Geophys pp 151–177

Pielke R, Adegoke J, Beltran-Przekurat A, Hiemstra C, Lin J, Nair U, Niyogi D, Nobis T (2007) An overview of regional land use and cover impacts on rainfall. Tellus 59B:587–601

Rebetez M, Dupont O, Giroud M (2009) An analysis of the July 2006 heatwave extent in Europe compared to the record year of 2003. Theor Appl Climatol 95:1–7, DOI 10.1007/s00704-007-0370-9

Reynolds RW, Smith T, Liu C, Chelton D, Casey K, Schlax M (2007) Daily high-resolution blended analyses for sea surface temperature. J Climate 20:5473–549

Roerink G, Menenti M, Verhoef W (2000) Reconstructing cloud-free NDVI composites using Fourier analysis of time series. Int J Rem Sens 21(9):1911–1917

Saha S, Moorthi S, Pan HL, Wu X, Wang J, Nadiga S, Tripp P, Kistler R, Woollen J, Behringer D, Liu H, Stokes D, Grumbine R, Gayno G, Wang J, Hou YT, ya Chuang H, Juang HMH, Iredell M, Treadon R, Kleist D, Delst PV, Keyser D, Derber J, Ek M, Meng J, Wei H, Yang R, Lord S, van den Dool H, Kumar A, Wang W, Long C, Chelliah M, Xue Y, Huang B, Schemm JK, Ebisuzaki W, Lin R, Xie P, Chen M, Zhou S, Higgins W, Zou CZ, Liu Q, Chen Y, Han Y, Cucurull L, Reynolds RW, Rutledge G, Goldberg M (2010) The NCEP Climate Forecast System Reanalysis. Bull Amer Meterol Soc 91:1015–1057

Seneviratne S, Luethi D, Litschi M, Schr C (2006) Land-atmosphere coupling and climate change in Europe. Nature 443:205–209

Skamarock WC, Klemp JB, Dudhia J, Gill DO, Barker M, Duda KG, Huang XY, Wang W, Powers JG (2008) A description of the Advanced Research WRF Version 3. Tech. rep., National Center for Atmospheric Research

Stauffer D, Seaman N (1990) Use of Four-Dimensional Data Assimilation in a Limited-Area Mesoscale Model. Part I: Experiments with Synoptic-Scale Data. Mon Weather Rev 110:1250–1277

Stull RB (1988) An Introduction to Boundary Layer Meteorology. Kluwer Acad. Publ., Dordrecht, Boston, London

Teuling A, Seneviratne S, Stckli R, Reichstein M, Moors E, Ciais P, Luyssaert S, van den Hurk S, Ammann C, Bernhofer C, Dellwik E, Gianelle D, Gielen B, Grnwald T, Klumpp K, Montagnani L, Moureaux C, Sottocornola M, Wohlfahrt G (2010) Contrasting response of European forest and grassland energy exchange to heatwaves. Nature Geoscience 3:722–727

Verhoef W, Menenti M, Azzall S (1996) A color composite of NOAA-AVHRR based on time series (1981-1992). Int J Rem Sens 17:231–25

Viovy N, Arino O, Belward A (1992) The Best Indx Slope Extraction (BISE) : A method for reducing noise in NDVI time-series. Int J Reote Sens 13:1585–1590, DOI 10.1080/0143119208904212

Weckwerth T, Parsons D, Koch S, Moore J, Lemone M, Demoz B, Flamant C, Geerts B, Wang J, Feltz W (2004) An overview of the International H2O Project (IHOP2002) and some preliminary highlights. Bulletin of the American Meteorological Society 85(2):253–277, DOI 10.1175/BAMS85-2-253

Yuan H, Dai Y, Xiao Z, Ji D, Shangguan W (2011) Reprocessing the MODIS Leaf Area Index products for land surface and climate modelling. Remote Sens Environ 115(5):1171 – 1187, DOI 10.1016/j.rse.2011.01.001

Zeng X, Dickinson RE, Walker A, Shaikh M, DeFries RS, Qi J (2000) Derivation and Evaluation of Global 1-km Fractional Vegetation Cover Data for Land Modeling. J Appl Meteorol 39:826–839

Appendix - The effects of spatial resolution in vegetation and precipitation processes in seasonal WRF simulations over Denmark

Authors: Joakim Refslund, Ebba Dellwik, Andrea N. Hahmann and Eva Bøgh (2013), J. Geosphys. Res., submitted.

The Effects of Spatial Resolution in Vegetation and Precipitation Processes in Seasonal WRF Simulations over Denmark

Joakim Refslund,[1] Ebba Dellwik,[1] Andrea N. Hahmann,[1] and Eva Boegh[2]

[1]Department of Wind Energy, Technical

University of Denmark, Roskilde, Denmark

[2]ENSPAC, Roskilde University, Roskilde,

Denmark

Abstract.   The impact of concurrent green vegetation fraction (GVF) de-

rived from Moderate Resolution Imaging Spectroradiometer (MODIS) ob-

servations is evaluated in year-long downscaling simulations using the Weather

Research and Forecasting (WRF) model at high resolution (9 and 3 km) by

comparing to simulations using climatological low-resolution GVFs. The WRF

simulations are also compared to gridded observational data of precipitation,

2-m temperature, 10-m wind speed and satellite-derived soil moisture, as well

as to local measurements of temperature, wind speed and Bowen ratio. When

the GVF differences were the largest, its use resulted in improved agreement

of the model simulations with temperature and wind observations. However,

during the summer months the highest resolution simulations using concur-

rent GVF underestimated precipitation and soil moisture and overestimated

the temperature compared to gridded observations. The 9 km resolution sim-

ulations, which ran using the convective precipitation scheme, showed large

overestimation of precipitation from May to September. The comparison with

FluxNet stations showed a better temporal evolution of Bowen ratios in the

simulations using concurrent GVF. This study shows that long-term high-

resolution simulations using the WRF model can describe the land surface

conditions accurately in a year with large variability. The use of concurrent

vegetation in the WRF model provides a more realistic and equally robust

way for model evaluation as compared to using the standard climatology.

1. Introduction

The principal task of a land surface model (LSM) in a numerical weather prediction (NWP) model is to accurately partition the available net radiation into soil, latent and sensible heat flux, the last two which exchange heat with the atmosphere, and influence the structure of the planetary boundary layer (PBL). This partition is critically dependent on the vegetation cover. Although this fact is well accepted, the vegetation description in many mesoscale models is based on a fairly coarse background vegetation climatology. In the Weather, Research and Forecasting (WRF) model, for example, this vegetation climatology is derived from satellite Normalized Difference Vegetation Index (NDVI) images from the period of 1985–1991 [*Gutman and Ignatov*, 1998]. The resultant green vegetation fraction (GVF) climatology varies throughout the year from monthly values, but is invariant from year to year. Several studies have investigated the effect of using concurrent GVF, as opposed to the climatology, WRF in simulations; however, mostly for time periods limited to a few months [*Hong et al.*, 2009; *Lakshmi et al.*, 2011] or tested in off-line simulations [*Miller et al.*, 2006]. *Refslund et al.* [2013] presented a method to use concurrent Moderate Resolution Imaging Spectro-radiometer (MODIS) data for longer simulations, by creating a new NDVI background climatology using 10 recent years of data, from which any single year of GVF data can be extracted. The first coupled simulation using the new MODIS vegetation description in the WRF model, was evaluated in a 18 × 18 km grid spacing over Europe for the heat wave year of 2006, and an improvement in the simulated surface temperature was demonstrated. This study concerns

a more extensive evaluation of the method using a higher resolution simulation for the area of Denmark [*Refslund et al.*, 2013].

Another critical parameter for correct simulation of the surface fluxes is the soil moisture content, which in turn is tightly linked to the precipitation input. The simulation of precipitation is an area of intense research in the regional climate modeling community (e.g., *Randall and Co-authors* [2007]; *Christensen and Co-autors* [2007]) in the context of climate change and its regional impact. *Vidale et al.* [2003] and *Rauscher et al.* [2010] pointed out the challenges of the correct estimation of warm season (WS) precipitation. The uncertainty concerning WS precipitation prediction is mainly connected with the use of convective parameterization schemes [*Castro et al.*, 2005], although other physical process schemes also impact it [*Jankov et al.*, 2005; *Brockhaus et al.*, 2008; *Mooney et al.*, 2013]. A promising, but computational expensive, solution for the problem of reduction of the errors in WS precipitation, is the use of models at cloud-resolving grid scales, which commonly are used for the purpose of NWP [*Mass et al.*, 2002; *Jankov et al.*, 2005], while still rarely applied in regional climate studies. A few short-term [*Hohenegger et al.*, 2008; *Warrach-Sagi et al.*, 2013] and one multi-year model integration [*Kendon et al.*, 2012] at cloud-resolving scales have shown promising results with reduced precipitation biases and more realistic precipitation patterns without using a convective scheme. However, the resolution limit at which the convection scheme should be turned off is under debate (i.e. *Weisman et al.* [1997]; *Kain* [2004]; *Gilliland and Rowe* [2007]). Therefore, for the high-resolution simulations in this study we also evaluate the effect of applying (or not) a convective scheme in WRF.

67   Despite of recent advances in remote-sensed products, validation of LSMs is compli-

68 cated by the lack of spatially distributed observational data of soil moisture and surface

69 fluxes. The most reliable option for model verification remains gridded surface data of

70 temperature and precipitation constructed from meteorological observations. Especially

71 concerning precipitation, very high-density networks are required for a correct quantifi-

72 cation [*Haylock et al.*, 2008]. This issue is extra critical in areas with complex terrain,

73 where the local orography and its representation in the model simulations can give rise

74 to very local precipitation patterns [*Grell et al.*, 2000; *Hahmann et al.*, 2010]. In addi-

75 tion, precipitation measurements suffer from lack of representativeness in complex terrain

76 [*Chen et al.*, 1996]. For the relatively flat area of Denmark, uncertainties concerning

77 orography are minimal and, more importantly, the precipitation measurement network is

78 comparatively dense, leading to an excellent dataset for model validation.

79   In high-resolution simulations, the surface energy balance can be directly validated

80 against flux measurements of sensible and latent heat using for example FluxNet stations

81 [*Baldocchi*, 2003]. This validation is however complicated by the lack of energy balance

82 closure apparent in the measurements [*Foken*, 2008], microscale effects [*Finnigan*, 1999;

83 *Sogachev et al.*, 2008], as well as a mismatch of scales. Such a validation is nevertheless

84 attempted in the present study, where uncertainties related to the flux measurements were

85 carefully examined.

86   The default GVF climatology in the WRF model is on a relatively coarse resolution

87 ($0.15° \times 0.15°$ and monthly time sampling), whereas the land-use classification is based

88 on a 1 km $\times$ 1 km dataset. This mismatch in resolution blurs the modeled combined

89 effects of the land-use characteristics and time-varying vegetation phenology. The MODIS-

based concurrent vegetation product by *Refslund et al.* [2013] has a spatial resolution that matches that of the land-use classification, and therefore has the potential for forcing the full effect of enhanced spatial and temporal resolution. Here, we therefore make a first evaluation of the increased resolution in the vegetation description on the near surface climate simulated by the WRF model.

This study is organized as follows. In section 2, the modeling setup and the new MODIS green vegetation fraction data are presented, followed by a description of the observational data used for validation. Section 3 presents the results, which is followed by a discussion of observational errors and improvements from altered vegetation phenology in section 4, where also the conclusions are draw.

2. Experimental setup

2.1. Model configuration

This study uses the non-hydrostatic WRF model version 3.4 [*Skamarock et al.*, 2008] to carry out high-resolution year-long simulations. A one-way nested domain configuration was selected to zoom in on the area of Denmark (Fig. 1) with horizontal grid spacings of 27 km, 9 km and 3 km, respectively. Figure 1 also shows the dominant land use classes over Denmark for domain 3 where the most common land use clases are: croplands (CL), mixed forests (MF), cropland/natural vegetation (CN) and urban areas. Domain 1 represents Denmark entirely by CL, while small patches with MF and CN are present in domain 2 (not shown).

The physical parameterizations chosen for the simulations are shown in Table 1. In principle, the processes and scales represented by the convective parameterization scheme (CPS) become inconsistent within the range of 1–10 km [*Kain*, 2004]. However, studies

have shown that even very high-resolution simulations sometimes need a CPS to accurately represent small sub-grid scale processes [*Gilliland and Rowe*, 2007]. Furthermore, as resolution decreases towards the lower end of this range, explicit simulation of convective features may be delayed and evolution degraded [*Weisman et al.*, 1997]. The KF-CPS is used in domain 1 and 2, although the resolution in domain 2 was within the critical range of 1–10 km, while in domain 3 the convection is simulated explicitly without a CPS (Table 1). This approach was also applied by *Soares et al.* [2012] in their 9 km simulations with good results for Portugal.

Initial and lateral boundary conditions were provided by the 6-hourly Climate Forecast System Reanalysis (CFSR; *Saha et al.* [2010]) at $0.5° \times 0.5°$ horizontal grid spacing, while the sea surface temperatures were described by $1/12° \times 1/12°$ daily sea surface temperatures [*Gemmill et al.*, 2007]. The dynamical downscaling technique (Type 2 in *Castro et al.* [2005]) uses grid nudging in the outermost domain only. Nudging was applied above level 15 for the wind speed components (u and v), water vapor mixing ratio (q) and potential temperature (T_θ). Grid nudging within the PBL was applied only to u and v, while not to q and T_θ. A total of 41 levels were used in the vertical.

Accurate description of the surface climate in models typically requires an initial spin-up simulation for the soil state variables and several methods exist [*Rodell et al.*, 2005]. Full model integrations single or multiple years are carried out until equilibrium of soil moisture is reached. However, a single-year loop can accumulate regional meteorological anomalies creating an unnatural equilibrium [*Schlosser and Coauthors*, 2000]. *Mooney et al.* [2013] found that results using spin-up periods of 1–4 years were not significantly different from results obtained without any spin-up. Therefore, in the simulations presented here, no

spin-up was used and the simulations start on 1 January 2006 using the soil moisture from

the reanalysis.

2.2. Weather conditions during 2006

The weather conditions over Denmark during 2006 deviated considerably from the long-term climatology. Colder than normal weather dominated until late March when spring-like temperatures were first observed. April and May were wetter than normal, while June was dry and warm. July was exceptionally warm with more than 4°C above normal. Only half of the normal precipitation amount was recorded with the majority falling at the very end of the month. This was contrasted in August with more than double the amount of normal precipitation, which mostly fell as heavy rain showers. The last four months of the year were all record-warm with temperatures of 3.0–5.4°C above normal and snowfall was restricted to a couple of days in early November [*Cappelen*, 2006].

2.3. Green vegetation fraction data

This study uses two GVF datasets in the WRF simulations: the standard 1985–1991 climatology [*Gutman and Ignatov*, 1998], and a new product derived from Moderate Resolution Imaging Spectro-radiometer (MODIS) NDVI images during 2001–2011, which is described in *Refslund et al.* [2013]. The data was derived using a land use class dependent method that converts the high-quality MODIS NDVI into GVF using a quadratic relationship. The grid spacing is $0.0083° \times 0.0083°$ (~ 1 km), while the temporal sampling is 8 days. Two simulations, summarised in Table 2, were carried out: one with the standard GVF climatology (named "control", C9 and C3 for 9 and 3 km grid spacing, respectively) and one using the new GVF product (named "experiment", analogously E9 and E3).

₁₅₄   Figure 2 shows GVF and seasonalities as represented in C3 and E3 for the land use

₁₅₅ classes CL, MF and CN. The seasonality of LAI is obtained through linear scaling between

₁₅₆ predefined minimum and maximum values in snow-free conditions using GVF as the

₁₅₇ scaling parameter. The surface roughness length (z_0), surface albedo (α) and emissivity

₁₅₈ (ϵ) are scaled in the same manner. The extreme values used in the scaling process for CL,

₁₅₉ MF and CN are shown in Table 3. The seasonalities of C9 and E9 are similar to C3 and E3.

₁₆₀ The differences in vegetation phenology are mainly concentrated in the second half of the

₁₆₁ year. Comparison of MF for C3 and E3 shows that a prolonged growing season occurred

₁₆₂ due to the anomalous warm autumn in 2006 (Fig. 2a and b). The GVF for croplands

₁₆₃ in E3 shows a double peak indicating sowing of winter seeds after harvest in July and

₁₆₄ August, while only one peak is represented in C3 (Fig. 2c and d). Since CL is the largest

₁₆₅ represented land use class in Denmark, the largest differences between the control and

₁₆₆ experiment simulations should be expected when the CL seasonalities deviates the most.

₁₆₇ The seasonality of CN shown in Fig. 2e and f show a mixture between the seasonality of

₁₆₈ MF and CL, as expected. Figure 3 shows an example of the spatial variability of GVF

₁₆₉ over Denmark as represented in C3 and E3 for 1 September 2006. The new GVF product

₁₇₀ show large spatial variability with clear differences between CL and MF in certain areas

₁₇₁ (compare Fig. 3b to Fig. 1), while almost uniform appearance is found in C3 simulations.

2.4. Gridded data

₁₇₂   A gridded dataset of daily mean 2-m temperature, 10-m wind speed and daily accumu-

₁₇₃ lated precipitation for Denmark [*Scharling*, 2012] produced by the Danish Meteorological

₁₇₄ Institute (DMI) is used for model validation. The dataset is referred to as the "DMI

₁₇₅ Climate Grid" in the following. It uses the UTM 32 coordinate system to represent 2-m

₁₇₆ temperature and 10-m wind speed on a 20 × 20 km grid and precipitation on a 10 ×

₁₇₇ 10 km grid. The temperature and wind speed data were derived from 78 synoptic and

₁₇₈ climate stations. The station network for precipitation consists of about 500 stations

₁₇₉ widely distributed throughout Denmark (total area of Denmark is 43,090 km^2). A double

₁₈₀ interpolation technique was applied to derive temperature and wind speeds to account

₁₈₁ for interpolation differences between inland and near-coast stations, while only one in-

₁₈₂ terpolation step was used for precipitation. The gridded precipitation was subsequently

₁₈₃ corrected for wetting and sheltering effects according to the recommendations of DMI

₁₈₄ [*Allerup et al.*, 1998], which cause precipitation to increase by 10% to 42%.

₁₈₅ Soil moisture data from satellite measurements of the upper soil layer (0.5–2 cm) was

₁₈₆ obtained from the European Space Agency — Climate Change Initiative (ESA-CCI) soil

₁₈₇ moisture project [*Wagner et al.*, 2012]. The data was generated by merging active and

₁₈₈ passive microwave observations of soil moisture into a single long-term dataset. The

₁₈₉ measurements over Denmark during winter and spring 2006 are limited, while the coverage

₁₉₀ during summer and fall is good. Denmark is represented on a latitude-longitude grid with

₁₉₁ a spatial grid of 0.25° × 0.25° and temporal sampling of about every third or fourth day.

₁₉₂ For verification, the WRF model output over domains 2 and 3 is regridded to the DMI

₁₉₃ climate grid or the ESA-CCI grid.

2.5. Station data

₁₉₄ From the DMI network of measuring stations, hourly observations of 2-m temperature

₁₉₅ and 10-m wind speeds during 2006 at 10 cropland sites were obtained . The sites mainly

₁₉₆ represent inland points widely spread throughout western Denmark as indicated by the

₁₉₇ black circles in Fig. 1. Careful quality control was performed before using the data

198 and only observed wind speeds above 1 m s^{-1} were used in the validation of the model

199 simulations. In addition, two FluxNet stations were selected for comparison with the

200 WRF-derived Bowen ratios during the summer months (locations indicated by red stars

201 in Fig. 1). The data used here showed an energy balance closure near 100%. The nearest

202 land point to a station location in the WRF model grid was used for the comparisons.

3. Results

3.1. Precipitation

203 Figure 4 shows the differences in WS precipitation between the WRF simulations and

204 the DMI gridded observations. Table 4 shows the BIAS (WRF minus observations) and

205 RMSE for seasonal precipitation, 2-m temperature and 10-m wind speed. Here the RMSE

206 is computed as the spatial RMSE of the seasonal means. The WS is defined from May

207 to September because of the warm conditions during 2006 over Denmark. Overall, the

208 precipitation from the high resolution simulations agrees well with the observed precipita-

209 tion amounts (Fig. 4a-b and Table 4). The observed spatially averaged WS precipitation

210 during the WS of 2006 is 358 mm, with the corrections for wetting and sheltering effects

211 accounting for 11% (35 mm). The spatially averaged WS precipitation derived from C3

212 and E3 is 345 mm and 326 mm, respectively, which represent an underestimate of 0.08

213 and 0.20 mm day^{-1} (4–9%). The BIAS and RMSE in Table 4 indicate that the precip-

214 itation simulated in C3 is closer to observations than that in E3. However, the smaller

215 biases in C3 are a consequence of localized regions of large precipitation that partially

216 compensate underestimates elsewhere. The simulated rainfall in the low resolution sim-

217 ulations (Fig. 4c-d) is significantly overestimated in nearly all areas of Denmark, but in

218 particular over western Denmark. The spatially averaged WS precipitation for C9 and E9

²¹⁹ is 573 mm and 536 mm, respectively, resulting in an average daily overestimate of 1.41

²²⁰ and 1.16 mm day⁻¹ (60% and 50%).

²²¹ The monthly precipitation spatially averaged over Denmark during 2006 for the ob-

²²² servations and the simulations is shown in Fig. 5. The partition between convective

²²³ (striped) and the non-convective (solid) precipitation is shown for the simulations using

²²⁴ the KF-CPS. All simulations show good agreement with the observations from January

²²⁵ to April. During the WS, the high resolution simulations generally show no systematic

²²⁶ errors and better agreement with the observations compared to the low resolution re-

²²⁷ sults. The largest difference in monthly accumulated precipitation between C3 and E3 is

²²⁸ found in July (10 mm), corresponding to about 25% of the observed rainfall during that

²²⁹ month. The low resolution simulations predict too much rainfall most of the WS, with

²³⁰ the largest overestimation occurring in August (about 70 mm). Good agreement with

²³¹ the observations is found for rainfall simulated by E9 during July, while C9 significantly

²³² overestimates the rainfall in July. During October–December, the simulated precipitation

²³³ is mostly underestimated except for C9 and E9, which show good agreement with the

²³⁴ observations. However, the correction for wetting and sheltering effects applied to the

²³⁵ observed precipitation during these three months are very large and contain significant

²³⁶ uncertainty, as will be discussed in section 4.

3.2. Soil moisture and surface energy balance

²³⁷ The biases of precipitation in the simulations will affect the soil moisture content in all

²³⁸ soil layers in the root zone, not just the surface. However, soil moisture measurements

²³⁹ that cover the depth of the root zone are spatially sparse, which limits their use for

²⁴⁰ spatial verification. Therefore, we evaluate the model simulations in two stages. First, we

compare the simulated top layer soil moisture against satellite observations (Fig. 6a) and later we compare the root-zone soil moisture among the various simulations (Fig. 6b). Comparison to observations during January–March is not shown because of the small sample size. In general, the soil moisture from the high resolution simulations show better agreement with the observations than that from the lower resolution. The soils are too wet in all simulations in May and June, despite of the good agreement in precipitation shown by C3 and E3 in May (Fig. 5). The high resolution simulations show soils that are too dry compared to observations in July, while C9 is too dry and E9 matches well with the observations. The findings agree with the underestimated precipitation by the high resolution runs and overestimated precipitation by low resolution runs (Fig 5). The high resolution simulations show good agreement with the observations from August and onwards, while the low resolution simulations significantly overestimate the soil moisture content from August to November.

Figure 6b shows the simulated soil moisture content in the top 1 m. Only minor differences exist between simulations using similar grid spacing. The low resolution simulations show significantly higher soil moisture content during the WS compared to the high resolution simulation, as expected from the results in Fig. 4 and 5. The largest difference occurs in August with soil moisture values of about 0.18 and 0.26 in the high and low resolution simulations, respectively. The lower precipitation in July simulated by E3, compared to C3 (Fig. 5), results in lower simulated soil moisture of the top soil layer (Fig. 6a) while the soil moisture in the top 1 m is slightly higher than in C3 (Fig. 6b). This result is probably linked to the generally lower LAI values in E3, compared to C3

263 (see Fig. 3b, d, f), which lead to less transpiration and higher soil wetness in the root

264 zone.

265   To explain how errors in soil moisture content and vegetation phenology affect the model

266 surface energy budget, two months (one dry and one wet) with significant differences in

267 MODIS versus climatological GVF, are investigated for CL. The experiment simulations

268 show lower GVF and LAI values compared to the control simulations during the dry

269 period (July), while the opposite occur during the wet period (September; Fig. 2c–d).

270 The energy balance terms, net radiation (RN), sensible heat (SH), latent heat (LH),

271 and ground heat (GH) flux, and the contributions to the latent heat flux averaged over

272 all cropland grid points from transpiration (TR), direct soil evaporation (ES) and from

273 evaporation of intercepted water by the canopy (EC) are shown in Figure 7.

274   During the dry period, the lower GVF caused E3 and E9 to show lower LH fluxes,

275 higher SH fluxes and similar GH fluxes at noon compared to the results from C3 and

276 C9, respectively. The difference in LH and SH flux between the experiment and control

277 simulations is about 60 and 40 $\mathrm{W\,m^{-2}}$, respectively. The LH fluxes are dominated by

278 transpiration (Fig. 7c–d) and therefore E3 and E9 show lower transpiration compared

279 to C3 and C9, respectively, due to the lower LAI during July (Fig. 3c–d). However,

280 the lower transpiration shown by the high resolution simulations, compared to their low

281 resolution counterparts, is a result of the lower precipitation and soil moisture. This can

282 be verified by comparing the surface energy balance and the transpiration for C9 and C3

283 during June and July (not shown). The noon Bowen ratios (BR = SH/LH) simulated by

284 C9 and E9 are in the range 0.50–0.75, while BR for C3 and E3 are between 0.75–1.15,

respectively. The differences in transpiration between C3 and E3 impact the root zone soil moisture content and reflect the differences in soil moisture in Figure Fig. 6b.

During the wet period, the energy balance terms show only minor differences between simulations at the same resolution (Fig. 7e-f), while the LH flux components are larger in the experiment than the control (Fig. 7g-h). Noon Bowen ratios for C9 and E9 are close to 0.50, while close to 1.0 for C3 and E3. Lower transpiration in C3 and C9 compared to E3 and E9 is compensated by higher evaporation of intercepted water and higher soil evaporation. The differences in precipitation between the high and low resolution simulations during August (Fig. 5) only affected canopy evaporation and soil evaporation, whereas transpiration was similar in all simulations.

The analysis above shows how differences in soil moisture content (not shown) and vegetation information impact the modeled surface energy balance. During the wet period, the influence of altered vegetation information on the surface energy balance components is hidden by the changes in the soil moisture content (Fig. 7e–f) and precipitation. This is not the case during the dry period (Fig. 7a–b). However, the analysis does not clarify whether concurrent vegetation information improved the partitioning of the available surface energy over the climatological vegetation data during the drier period.

To investigate this we used data from the Lille Valby (Dk-LVa) and Risbyholm (Dk-Ris) cropland flux stations (locations indicated in Fig 1), and compared the observed Bowen ratios to those in simulated by C3 and E3 (Fig. 8). The measurements are based on half-hourly averages. For both simulated and measured flux data, only cases with energy fluxes exceeding $50 \, \mathrm{W \, m^{-2}}$ and the net radiation exceeding $100 \, \mathrm{W \, m^{-2}}$ were considered. The

307 selected data were grouped into 3-day intervals and then averaged. Averages including

308 less than five half-hourly measurements were discarded.

309   The observed temporal evolution of the Bowen ratio at Risbyholm in Fig. 8a is best

310 simulated by E3, although the double peak values are overestimated. The overestimation

311 in the Bowen ratio can be explained by too low soil moisture conditions from late July

312 until the middle of August due to underestimation of precipitation, as indicated in Fig 5

313 and 6, or by a mismatch in footprint as the measurement height was too low to represent

314 a whole model grid cell. C3 shows too low Bowen ratios and does not represent the

315 double peak structure seen in the observations. At Lille Valby (Fig. 8b), the Bowen

316 ratios simulated by C3 and E3 in June and the first half of July are very similar but

317 too low compared to the observations. E3 shows good agreement with the observations

318 during the last part of July but do not represent the sharp decline in Bowen ratio in

319 August, as shown by the observations. Instead, a slowly decreasing trend is simulated

320 such that the difference in Bowen ratio between E3 and the observations is minor towards

321 September. C3 shows the highest Bowen ratios in the beginning and end of August, which

322 do not match the temporal evolution in the observed Bowen ratio. In fact, the temporal

323 evolution in Bowen ratio shown by C3 is very similar at both stations, which is related

324 to the low spatial resolution of the climatological GVF data applied in C3. Figure 8

325 clearly shows the advantage of using the concurrent, high resolution GVF data in WRF

326 to improve the temporal evolution of Bowen ratios on larger spatial scale.

3.3. Surface air temperature

327   The differences in soil moisture and vegetation phenology modify the surface energy

328 balance and should in turn lead to differences in 2-m temperature between the simulations,

³²⁹ which are investigated next. A comparison of the gridded mean 2-m temperature biases

³³⁰ are shown in Table 4. C3 and C9 are closer to the observations during winter and spring

³³¹ (DJF and MAM) compared to E3 and E9. The differences are small and the biases

³³² obtained during February and March dominate. and the biases obtained during February

³³³ and March dominate. The summer (JJA) statistics show smaller biases by C9 and E9,

³³⁴ despite of the overestimation of precipitation and soil moisture, while E9 and E3 are closer

³³⁵ to the observations during the fall (SON). The largest difference in seasonal temperature

³³⁶ bias between the experiment (E3 and E9) and control (C3 and C9) simulations occur in

³³⁷ SON. For this period, both C3 and E3 show excellent comparison with the soil moisture

³³⁸ data (Fig. 6a) while large differences in GVF exist (Fig. 3a, c, e).

³³⁹   The spatial variability of daily mean 2-m temperature was examined by comparing

³⁴⁰ monthly averages of temperature on the gridded data. An example is shown in Fig. 9

³⁴¹ for September. Generally, inland grid cells are better predicted than those closer to the

³⁴² coast. Areas near the inner Danish waters show large positive biases during the WS, also

³⁴³ visible in Fig. 9. In addition, the urban area of Copenhagen (Fig. 9b and c) show positive

³⁴⁴ biases between 2–4 K for C3 and E3. An east-west temperature gradient during the WS

³⁴⁵ results in positive biases to the east, especially in JJA, while the western areas show good

³⁴⁶ comparison to the observations. The winter months tend to be too warm near the western

³⁴⁷ coast by 0–2 K, while the eastern areas are 0–3 K too cold (not shown).

³⁴⁸   The diurnal temperature range (DTR) for C3 and E3 is examined by comparison to

³⁴⁹ hourly temperature data from ten measuring stations (Fig. 1). The stations were selected

³⁵⁰ due to their good coverage in Jutland (western Denmark) and mainly inland stations.

³⁵¹ The DTR (left) and a Q-Q plot (right) of the temperature distributions during SON is

shown in Figure 10. The differences between C3 and E3 are not large, however, the E3

simulation improves the simulation of both nighttime and daytime temperatures showing

excellent agreement with the observations. The Q-Q plot confirms that both the lower

and higher end of the temperature distribution are improved, although the differences are

small. The DTR during JJA (not shown) did not indicate any differences between C3

and E3, which is consistent with the seasonal biases shown in Table 4.

3.4. Winds

Finally, the simulations were examined for differences in 10-m wind speed. The MYJ

surface layer scheme in WRF computes the 10-m wind speed using a corrected roughness

to approximate local shelter readings according to the WMO standards. This approach

might not be representative for a grid box average and, in some cases, results in higher

10-m wind speeds compared to the lowest model level [*Draxl et al.*, 2012]. A logarithmic

function is used instead to calculate the 10-m wind speed from the lowest model level

output [*Mass et al.*, 2002]:

$$U_{10m} = U_r \frac{\ln(10/z_0)}{\ln(z_r/z_0)}, \tag{1}$$

where U_{10m} is the 10-m wind speed, U_r is the lowest model level wind speed, z_0 is the

time-varying surface roughness length and z_r is the height of the lowest model level ($\simeq 20$

m). Wind speeds for both the 9 and 3 km grid spacings were computed and regridded

to match the DMI climate grid at 20×20 km resolution. The seasonal biases based on

daily mean 10-m wind speeds are shown in Table 4. The statistics show that mean 10-m

wind speeds are overestimated throughout the year except during MAM for C3 and E3,

which show a slight underestimation of the wind speeds. Larger overestimations occur in

coastal areas (not shown). Simulated wind speeds decrease as resolution increases due to

larger land surface variability, which result in higher surface roughnesses, and generally

C3 and E3 compare better to the observations than C9 and E9.

Diurnal wind speeds at the 10 measuring stations and the Q-Q plot of the wind speed

distributions during SON are shown in Fig. 11. The hourly wind speeds and Q-Q diagram

indicate that mainly the low wind speeds during nighttime are overestimated, while day-

time wind speeds agree well with the observations. The results from E3 compare better

to the observed diurnal variation in hourly wind speeds than those from C3. However, the

Q-Q plot indicates that the high end ($U_{10m} > 8\,\mathrm{m\,s^{-1}}$) of the wind speed distribution is

underestimated, while the lower end is overestimated. The underestimation of the higher

tail of the distribution is worse in E3 than in C3.

4. Discussion and conclusions

Given that the model simulations were only forced to follow the 2006 weather conditions

using grid nudging on the upper levels, their results are in remarkably good agreement

with the observations, and the errors do not grow as the simulation progresses through

the year (Table 4). The use of grid nudging has been discussed in previous work (e.g.

Miguez-Macho et al. [2004]; *Bowden et al.* [2012]). In general, the simulations with con-

current vegetation (E3 and E9) show equally good results as the ones using climatological

vegetation conditions (C3 and C9). Together with the results presented in *Refslund et al.*

[2013] for lower resolution, but for a larger area with stronger land-atmosphere coupling

of lower oceanic influences, we consider the use of concurrent MODIS-based vegetation

input to be a reliable and promising method for simulations using the WRF-Noah model.

Especially, multi-year studies concerning vegetation feed-backs and long-term seasonal weather prediction could benefit from using the presented approach for model evaluation.

High-resolution (i.e., a few kilometers), long-term (i.e., a year or longer) simulations are still rare in the scientific literature and mostly focus solely on the validation of precipitation [*Grell et al.*, 2000; *Kendon et al.*, 2012] or precipitation and temperature extremes [*Gao et al.*, 2012], whereas we have attempted verification for many surface parameters. Also, the mentioned precipitation studies have concerned high-resolution effects in more complex orography, where the effect of the convective parameterization scheme is mixed with that of better-resolved terrain.

During the WS, the precipitation simulated in the coarser resolution grids (C9 and E9) was overestimated, whereas precipitation in the high-resolution simulations (C3 and E3) was closer to the observed amounts (Fig. 4 and Table 4). This result underlines the previous findings by *Hohenegger et al.* [2008] and *Kendon et al.* [2012], that the cloud-resolving resolution simulations significantly enhance model performance during the WS even on flat terrain. It is often thought that the correct simulation of precipitation over flat terrain is easier than over more complex terrain. However, in the lack of strong topographic forcing, the details of model parameterizations and how they interact with each other are critical for correct simulation of the WS precipitation field. This justifies the location of the current study added to the availability of an excellent dataset for validation.

In July, however, both E3 and C3 underestimated the precipitation, which is consistent with the underestimation of soil moisture demonstrated in Fig. 6 and the highest overestimation of temperature. In October to December, both the E9 and C9 precipitation

simulations were closer to the observations than E3 and C3. However, the observations during this period are more uncertain than during the rest of the year due to the anomalous autumn. The precipitation corrections are based on mean meteorological data from the period 1961–1990. Whereas the corrections amount to 10% during the WS, they constitute as much as 40% in the winter months, because of the large corrections associated with the measurement of snowfall. The period from October to December 2006 showed record-breaking warm temperatures and snowfall was nearly absent. Thus, it is very likely that the applied corrections are too large during the period from October to December. By applying the September correction to October–December, the observed precipitation is reduced by 36 mm, which would reduce the dry bias of all simulations in Fig. 5. Despite the poorer precipitation prediction, the E3 and C3 soil moisture shows a closer agreement with observations during the whole autumnal period than E9 and C9 (Fig.6).

The uncorrected observed accumulated precipitation in 2006 was 777 mm, whereas the corrected amount was 905–941 mm, depending on whether the September correction is used for October to December or not. *Refslund* [2013] calculated the accumulated precipitation in the widely used E-OBS dataset version 5 [*Haylock et al.*, 2008] for Denmark, which showed a significantly lower precipitation of 690 mm for 2006. The large increase of more than 30% associated with the gridded data from DMI is still smaller than previously observed when comparing to higher-density networks [*Hofstra et al.*, 2009] and underlines the importance of dense precipitation networks. Especially for a windy, cold climate, the results illustrate the need of reliable precipitation corrections, as also discussed by *Rauscher et al.* [2010].

In the anomalous year of 2006, the differences in GVF between the synchronous and climatological datasets occur mainly during autumn (SON), with larger vegetation fractions in the concurrent dataset than in the climatology. Because of the GVF-based scaling of surface parameters in the Noah LSM, there are also significant changes mainly in July in LAI, albedo, surface roughness length and emissivity.

In July, the difference in precipitation between E3 and C3 is probably a consequence of the low soil moisture, where the reduced E3 evapotranspiration leads to a too warm and dry atmosphere. The use of the new and more realistic GVF therefore enhances the warm bias for E3 relative to C3. In general all simulations show a warm bias during the summer, and the effects of both the decreased soil moisture (E3 versus E9 or C3 versus C9) and vegetation (E3 versus C3 or E9 versus C9) are equally small. The reason for this bias could either be a small systematic error in the net radiation or in the soil process parameterizations. The too shallow soil column in Noah LSM, which could lead to a too fast drying of the soil, has indeed been recognized as one of the weaknesses of the model (e.g. *Niu et al.* [2011]). In the recent Noah MP, an unconfined aquifer has been added which results in significantly wetter soils (see Fig. 4 in *Niu et al.* [2011] and *Refslund* [2013]).

During SON, the enhanced GVF in E9 and E3 improves the agreement with the observations in terms of temperature and wind speed compared to C9 and C3, respectively (Table 4). Whereas the effects of using concurrent GVF were small for temperature, wind speed and precipitation, it had a strong impact to improve the surface energy balance simulation (Fig. 7) and the Bowen ratio during JJA (Fig. 8). However, as also demonstrated in Fig. 7, the effect of deficiencies in soil moisture is equally important.

454 Finally, we return to the issue of resolution of the GVF datasets and its importance

455 for determining the effect of different land use classes that was raised in the Introduction.

456 Figure 12 shows the July mean evapotranspiration for the zoomed in area of eastern

457 Denmark together with the land use classification. It is obvious that the effect of the

458 different land uses in the evaporation is blurred using the *Gutman and Ignatov* [1998]

459 low-resolution GVF, whereas the high-resolution vegetation dataset clarifies the land use

460 influence. To properly evaluate the effect of increasing resolution in mesoscale model

461 simulations, it is important that consistent high-resolution land surface products are used.

462 The importance of the matching resolution in land use and GVF will probably be quite

463 evident if the output from the simulation was used to drive hydrological models or if a

464 LSM model that includes dynamic vegetation was being used.

References

Allerup, P., H. Madsen, and F. Vejen (1998), Standard values for precipitation correction (1961–90), *Technical report 98-10*, Danish Meteorological Institute, Copenhagen, Denmark.

Baldocchi, D. (2003), Assessing the eddy covariance technique for evaluating carbon dioxide exchange rates of ecosystems: past, present and future, *Global Change Biology*, *9*, 479–492.

Bowden, J. H., T. Otte, C. Nolte, and M. Otte (2012), Examining interior grid nudging techniques using two-way nesting in the WRF model for regional climate modeling, *J. Climate*, *25*, 2805–2823, doi:10.1175/JCLI-D-11-00167.1.

Brockhaus, P., D. Lúthi, and C. Schär (2008), Aspects of the diurnal cycle in a regional climate model, *Meteorologische Zeitschrift*, *17*(4), 433–443.

Cappelen, J. (2006), Danmarks Klima 2006 med Tórshavn, Færøerne og Nuuk, Grønland: With english translations, *Teknisk rapport 07-01*, Danish Meteorological Institute.

Castro, C. L., R. A. Pielke Sr., and G. Leoncini (2005), Dynamical downscaling: Assessment of value retained and added using the Regional Atmospheric Modeling System (RAMS), *J. Geophys. Res.*, *110*(D05108), 1–21, doi:10.1029/2004JD004721.

Chen, F., and J. Dudhia (2001), Coupling an advanced land surface-hydrology model with the Penn State-NCAR MM5 modeling system. part II: Preliminary model validation, *Mon. Wea. Rev.*, *129*(4), 587–604.

Chen, M. X., R. E. Dickinson, X. B. Zeng, and A. N. Hahmann (1996), Comparison of precipitation observed over the continental United States to that simulated by a climate model, *J. Climate*, *9*, 2233–2249.

Christensen, J., and Co-autors (2007), Regional climate projections, in *Climate Change 2007: The Physical Science Basis. Contribution of Working Group I to the Fourth Assessment Report of the Intergovernmental Panel on Climate Change*, edited by S. Solomon, D. Qin, M. Manning, Z. Chen, M. Marquis, K. Averyt, M. Tignor, and H. Miller, Cambridge University Press, Cambridge, USA.

Draxl, C., A. Hahmann, A. Peña, and G. Giebel (2012), Evaluating winds and vertical wind shear from Weather Research and Forecasting model forecasts using seven planetary boundary layer schemes, *Wind Energy*, doi:10.1002/we.1555.

Dudhia, J. (1989), Numerical study of convection observed during the winter monsoon experiment using a mesoscale two-dimensional model, *J. Atmos. Sci.*, *46*(20), 3077–3107.

Finnigan, J. (1999), A comment on the paper by lee (1998): On micrometeorological observations of surface-air exchange over tall vegetation, *Agric. For. Meteorol.*, *97*, 55–64.

Foken, T. (2008), The energy balance problem: An overview, *Ecological Applications*, *18*(6), 1351–1367.

Gao, Y., J. S. Fu, J. B. Drake, Y. Liu, and J.-F. Lamarque (2012), Projected changes of extreme weather events in the eastern United States based on a high resolution climate modeling system, *Environ. Res. Lett.*, doi:10.1088/1748-9326/7/4/044025.

Gemmill, W., B. Katz, and X. Li (2007), Daily real-time global sea surface temperature — High resolution analysis at NOAA/NCEP, *Office Note Nr. 260, 39 pp*, NOAA/NWS/NCEP/MMAB.

Gilliland, E. K., and C. M. Rowe (2007), A comparison of cumulus parameterization scheme in the WRF model, presented at 87th AMS Annual Meeting & 21th Conference on Hydrology, San Antonio, Texas, USA.

Grell, G., L. Schade, R. Knoche, A. Pfeiffer, and J. Egger (2000), Nonhydrostatic climate simulations of precipitation over complex terrain, *J. Geophys. Res.*, *105*(D24), 29,595–29,608, doi:10.1029/2000JD900445.

Gutman, G., and A. Ignatov (1998), The derivation of the green vegetation fraction from NOAA/AVHRR data for use in numerical weather prediction models, *International Journal of Remote Sensing*, *19*(8), 1533–1543, doi:10.1080/014311698215333.

Hahmann, A. N., D. Rostkier-Edelstein, T. T. Warner, F. Vandenberghe, Y. Liu, R. Babarsky, and S. P. Swerdlin (2010), A reanalysis system for the generation of mesoscale climatographies, *J. Appl. Meteorol. Clim.*, *49*(5), 954–972, doi:10.1175/2009JAMC2351.1.

Haylock, M. R., N. Hofstra, A. M. G. K. Tank, E. J. Klok, P. D. Jones, and M. New (2008), A European daily high-resolution gridded data set of surface temperature and precipitation for 19502006, *J. Geophys. Res.*, *113*(D20119), doi:10.1029/2008JD010201.

Hofstra, N., M. Haylock, M. New, and P. Jones (2009), Testing E-OBS European high-resolution gridded data set of daily precipitation and surface temperature, *J. Geophys. Res.*, *114*(D21), D21,101, doi:10.1029/009JD011799.

Hohenegger, C., P. Brockhaus, and C. Schär (2008), Towards climate simulations at cloud-resolving scales, *Meteorologische Zeitschrift*, *17*(4), 383–394, doi:10.1127/0941-2948/2008/0303.

540   Hong, S., V. Lakshmi, E. Small, M. F. Chen, Tewari, and K. Manning (2009), Effects of

541   vegetation and soil moisture on the simulated land surface processes from the coupled

542   WRF/Noah model, *J. Geophys. Res.*, *114*, doi:10.1029/208JD011249.

543   Hong, S.-Y., J. Dudhia, and S.-H. Chen (2004), A revised approach to ice-microphysical

544   processes for the bulk parameterization of cloud and precipitation, *Mon. Wea. Rev.*,

545   *132*(1), 103–120.

546   Janjic, Z. I. (1996), The surface layer in the NCEP Eta Model, presented at 11th Conf.

547   on Numerical Weather Prediction, Norfolk, VA, 19-23 August.

548   Janjic, Z. I. (2002), Nonsingular implementation of the Mellor-Yamada level 2.5 scheme

549   in the NCEP Meso model, *Office Note 437*, NCEP.

550   Jankov, I., W. Gallus Jr., M. Segal, B. Shaw, and S. Koch (2005), The impact of different

551   WRF model physical parameterizations and their interactions on warm season MCS

552   rainfall, *Weather Forecasting*, *20*, 1048–1060.

553   Kain, J. S. (2004), The Kain-Fritsch convective parameterization: An update, *J. Appl.*

554   *Meteorol. Clim.*, *43*(1), 170–181.

555   Kendon, E., N. Roberts, C. A. Senior, and M. Roberts (2012), Realism of rainfall in a very

556   high-resolution regional climate model, *J. Climate*, *25*, 5791–5806, doi:10.1175/JCLI-

557   D-11-00562.1.

558   Lakshmi, V., S. Hong, E. Small, and F. Chen (2011), The influence of the land surface

559   on hydrometeorology and ecology: New advances from modeling and satellite remote

560   sensing, *Hydrology Research*, *42*, 95–112, doi:10.2166/nh.211.071.

561   Mass, C. F., D. Ovens, K. Westrick, and B. Colle (2002), Does increasing horizontal

562   resolution produce more skillful forecasts?, *Bull. Amer. Meteor. Soc.*, *83*(3), 407–430.

Miguez-Macho, G., G. L. Stenchikov, and A. Robock (2004), Spectral nudging to eliminate the effects of domain position and geometry in regional climate model simulations, *J. Geophys. Res.*, *109*(D13).

Miller, J., M. Barlage, X. Zeng, H. Wei, K. Mitchell, and D. Tarpley (2006), Sensitivity of the NCEP/Noah land surface model to the MODIS green vegetation fraction data set, *J. Geophys. Res.*, *33*(13), doi:10.1029/2006GL026636.

Mlawer, E. J., S. J. Taubman, P. D. Brown, M. J. Iacono, and S. A. Clough (1997), Radiative transfer for inhomogeneous atmospheres: RRTM, a validated correlated-k model for the longwave, *J. Geophys. Res.*, *102*(D14), 16,663–16,682, doi:10.1029/97JD00237.

Mooney, P. A., F. J. Mulligan, and R. Fealy (2013), Evaluation of the sensitivity of the Weather Research and Forecasting model to parameterization schemes for regional climates of Europe over the period 1990-95, *J. Climate*, *26*, 1002–1017.

NCL (2013), The NCAR Command Language (version 6.1.1) [software]., doi: 10.5065/D6WD3XH5.

Niu, G.-Y., Z.-L. Yang, K. E. Mitchell, F. Chen, M. B. Ek, M. Barlage, A. Kumar, K. Manning, D. Niyogi, E. Rosero, et al. (2011), The community Noah land surface model with multiparameterization options (Noah-MP): 1. Model description and evaluation with local-scale measurements, *J. Geophys. Res.*, *116*(D12).

Randall, D., and Co-authors (2007), Climate models and their evaluation, in *Climate Change 2007: The Physical Science Basis. Contribution of Working Group I to the Fourth Assessment Report of the Intergovernmental Panel on Climate Change*, edited by S. Solomon, D. Qin, M. Manning, Z. Chen, M. Marquis, K. Averyt, M. Tignor, and H. Miller, Cambridge University Press, Cambridge, USA.

Rauscher, S., E. Coppola, C. Piani, and F. Giorgi (2010), Resolution effects on regional climate model simulations of seasonal precipitation over Europe, *Clim. Dyn.*, *35*(4), 685–711, doi:10.1007/s00382-009-0607-7.

Refslund, J. (2013), Representing vegetation processes in hydrometeorological simulations using the WRF model, Ph.D. thesis, DTU Wind Energy, Roskilde, Denmark.

Refslund, J., E. Dellwik, A. Hahmann, M. Barlage, and E. Boegh (2013), Impacts of green vegetation fraction data in WRF simulations, *Theor. Appl. Climatol.*, *submitted.*

Rodell, M., P. R. Houser, A. Berg, and J. S. Famiglietti (2005), Evaluation of 10 methods for initializing a land surface model, *J. Hydrometeorol.*, *6*, 146–155, doi: 10.1175/JHM414.1.

Saha, S., S. Moorthi, H.-L. Pan, X. Wu, J. Wang, S. Nadiga, P. Tripp, and R. Kistler (2010), The NCEP climate forecast system reanalysis, *Bull. Am. Meteorol. Soc.*, *91*, 1015–1057.

Scharling, M. (2012), Guide to Climate Data and Information from the Danish Meteorological Institute, *Technical Report 12-08*, Danish Meteorological Institute, Copenhagen, Denmark.

Schlosser, C., and Coauthors (2000), Simulations of a boreal grassland hydrology at Valdai, Russia: PILPS Phase 2(d), *Mon. Wea. Rev.*, *128*, 301–321.

Skamarock, W. C., J. B. Klemp, J. Dudhia, D. O. Gill, M. Barker, K. G. Duda, X. Y. Huang, W. Wang, and J. G. Powers (2008), A description of the Advanced Research WRF Version 3, *Tech. Report. NCAR/TN–475+STR*, National Center for Atmospheric Research, Boulder, Colorado.

Soares, P., R. Cardoso, P. Miranda, J. Medeiros, M. Belo-Pereira, and F. Espirito-Santo (2012), WRF high resolution dynamical downscaling of ERA-Interim for Portugal, *Clim. Dyn.*, *39*, doi:10.1007/s00382-012-1315-2.

Sogachev, A., M. Leclerc, G. Zhang, U. Rannik, and T. Vesala (2008), Co2 fluxes near a forest edge: a numerical study, *Ecol. Appl.*, *18*(6), 1454–1469.

Vidale, P. L., D. Lthi, C. Frei, S. I. Seneviratne, and C. Schr (2003), Predictability and uncertainty in a regional climate model, *J. Geophys. Res.*, *108*(D18), 2156–2202, doi: 10.1029/2002JD002810.

Wagner, W., W. Dorigo, R. de Jeu, D. Fernandez, J. Benveniste, E. Haas, and M. Ertl (2012), Fusion of active and passive microwave observations to create an essential climate variable data record on soil moisture, *ISPRS Annals of Photogrammetry, Remote Sensing and Spatial Information Sciences*, *I-7*, 315–321, doi:10.5194/isprsannals-I-7-315-2012.

Warrach-Sagi, K., T. Schwitalla, V. Wulfmeyer, and H.-S. Bauer (2013), Evaluation of a climate simulation in Europe based on the WRF-NOAH model system: precipitation in Germany, *Clim. Dyn.*, pp. 1–20, doi:10.1007/s00382-013-1727-7.

Weisman, M., W. Skamarock, and J. Klemp (1997), The resolution dependence of explicitly modeled convective systems, *Mon. Wea. Rev.*, *125*, 527–548.

Table 1. Physical parameterization schemes used in the simulations.

Physics Scheme (Abrev)	Reference
Noah Land Surface Model (Noah LSM)	*Chen and Dudhia* [2001]
Mellor-Yamada-Janic (MYJ) PBL	*Janjic* [2002]
Monin-Obukhov (Janjic Eta) scheme	*Janjic* [1996]
WRF Single-Moment 5-class scheme (WSM5) microphys.	*Hong et al.* [2004]
Rapid Radiative Transfer Model (RRTM) longwave	*Mlawer et al.* [1997]
Dudhia shortwave	*Dudhia* [1989]
Kain-Fritsch (KF) convection[a]	*Kain* [2004]

[a] Only used in the 27 and 9 km grid spacing domains.

Table 2. Summary of the model experiments.

	Name	Grid spacing	Vegetation data	Convection
Control	C3	3 km	AVHRR	Explicit
	C9	9 km	AVHRR	Kain-Fritsch
Experiment	E3	3 km	MODIS	Explicit
	E9	9 km	MODIS	Kain-Fritsch

Table 3. Minimum and maximum values of LAI, surface roughness length (z_0), emissivity (ϵ) and albedo (α) for the three most common land use classes over Denmark.

Land use classes	LAI [-]		z_0 [m]		ϵ [-]		α [-]	
	min	max	min	max	min	max	min	max
Mixed Forest	2.80	5.50	0.20	0.50	0.930	0.970	0.17	0.25
Croplands	1.56	5.68	0.05	0.15	0.920	0.985	0.17	0.23
Cropland/Natural Vegetation	2.29	4.29	0.05	0.14	0.920	0.980	0.18	0.23

Table 4.   BIAS (WRF minus observations) and RMSE of the seasonally averaged precipitation

(mm day^{-1}), 2-m temperature (K) and 10-m wind speed (m s^{-1}).

Season	C3	E3	C9	E9	C3	E3	C9	E9
	BIAS precipitation				*RMSE precipitation*			
DJF	−0.44	−0.40	−0.36	−0.31	2.20	2.18	2.12	2.19
MAM	0.00	0.01	0.60	0.61	2.69	2.69	2.84	2.84
JJA	−0.20	−0.42	1.58	1.15	4.96	4.84	5.47	4.96
SON	−0.40	−0.36	0.13	0.23	3.13	3.14	3.09	3.10
	BIAS 2-m temperature				*RMSE 2-m temperature*			
DJF	−0.69	−0.77	−0.71	−0.79	1.17	1.20	1.15	1.18
MAM	−0.77	−0.80	−0.72	−0.77	1.23	1.21	1.21	1.19
JJA	0.63	0.64	0.49	0.48	0.98	0.97	0.92	0.91
SON	0.25	0.07	0.13	−0.05	0.69	0.68	0.69	0.71
	BIAS 10-m wind speed				*RMSE 10-m wind speed*			
DJF	0.31	0.21	0.51	0.41	0.96	0.98	1.00	1.01
MAM	−0.12	−0.07	0.03	0.08	0.88	0.89	0.89	0.90
JJA	0.32	0.41	0.42	0.50	1.00	1.03	1.05	1.09
SON	0.35	0.20	0.52	0.36	0.96	0.96	1.01	0.99
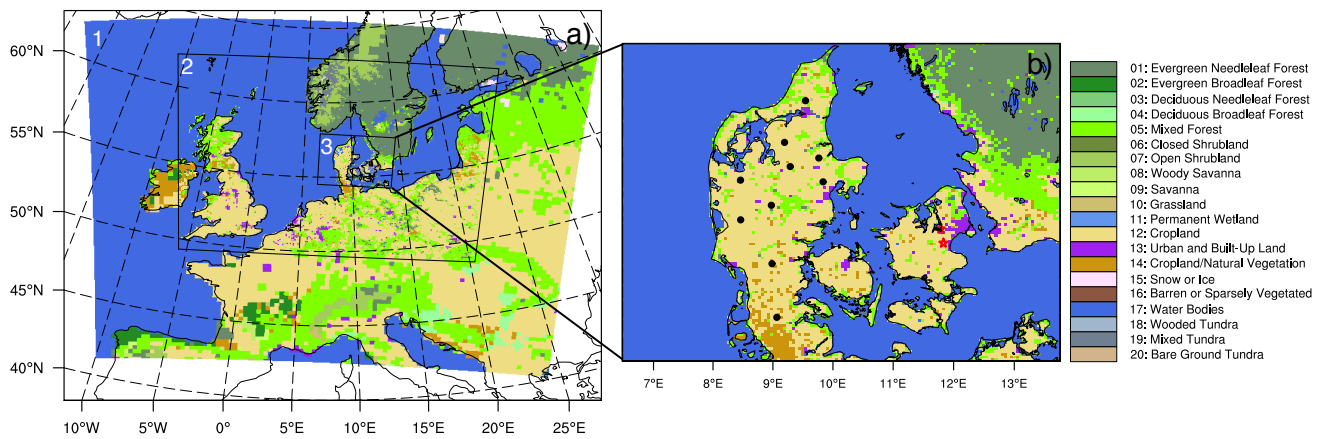
Figure 1. Nested domain configuration of the WRF model simulations with horizontal grid spacing of 27 km (domain 1), 9 km (domain 2) and 3 km (domain 3). The colors indicate the dominant landuse classes in the domains. The location of the stations used for the temperature and winds analysis are represented by black circles, while flux stations are indicated by red stars.
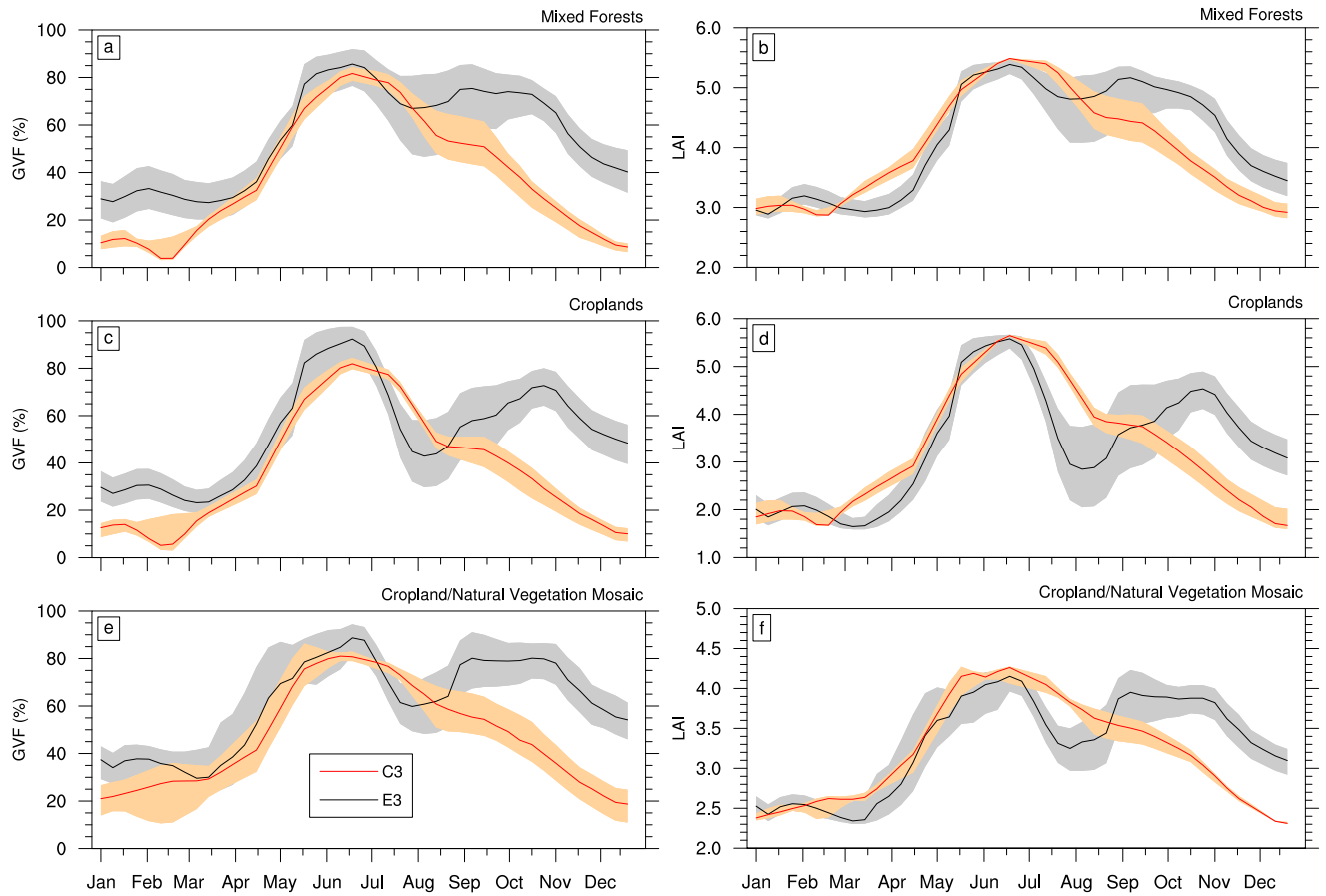
Figure 2.   Annual evolution of GVF (a, c, e) and LAI (b, d, f) during 2006 in the innermost domain for C3 and E3. The solid lines represent the median values, while the shaded areas show the 25th and 75th percentiles for: mixed forest (a, b), croplands (c, d) and cropland/natural vegetation mosaic (e, f).
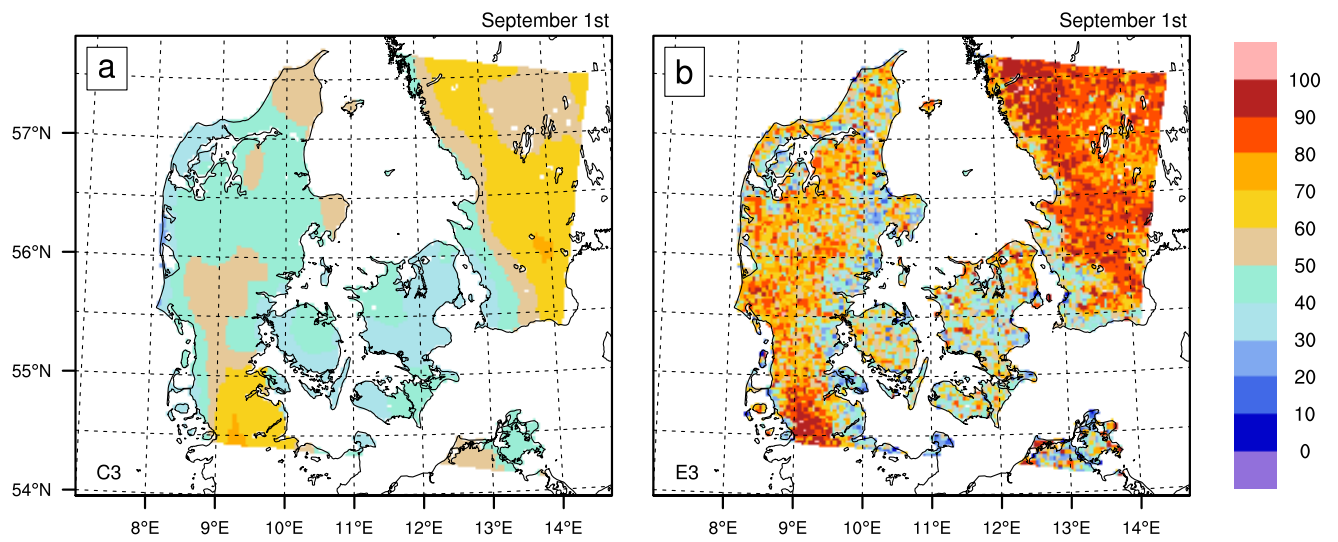
Figure 3. Comparison of GVF (%) on 1 September 2006 for C3 (a) and E3 (b).
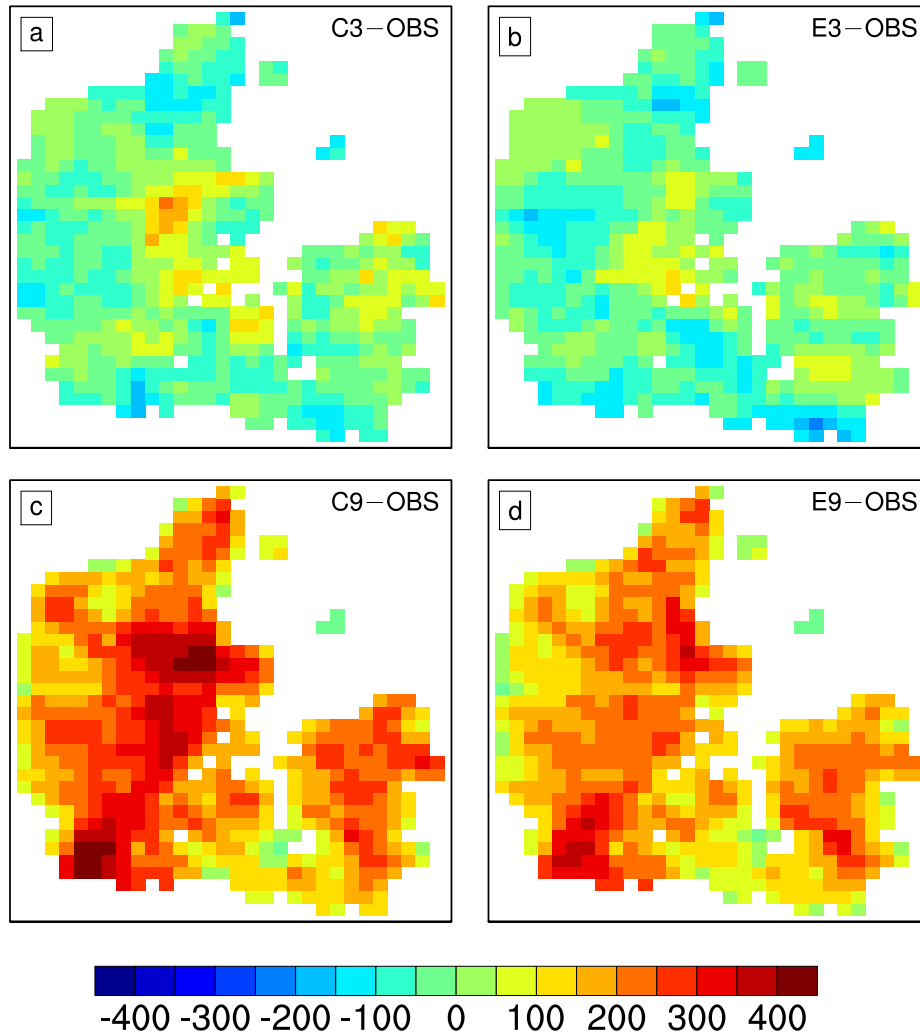
Figure 4.   Differences (WRF minus observations) in WS (May–September) accumulated precipitation (mm) over Denmark during 2006 on the 10×10 km grid for: (a) C3, (b) E3, (c) C9, and (d) E9.
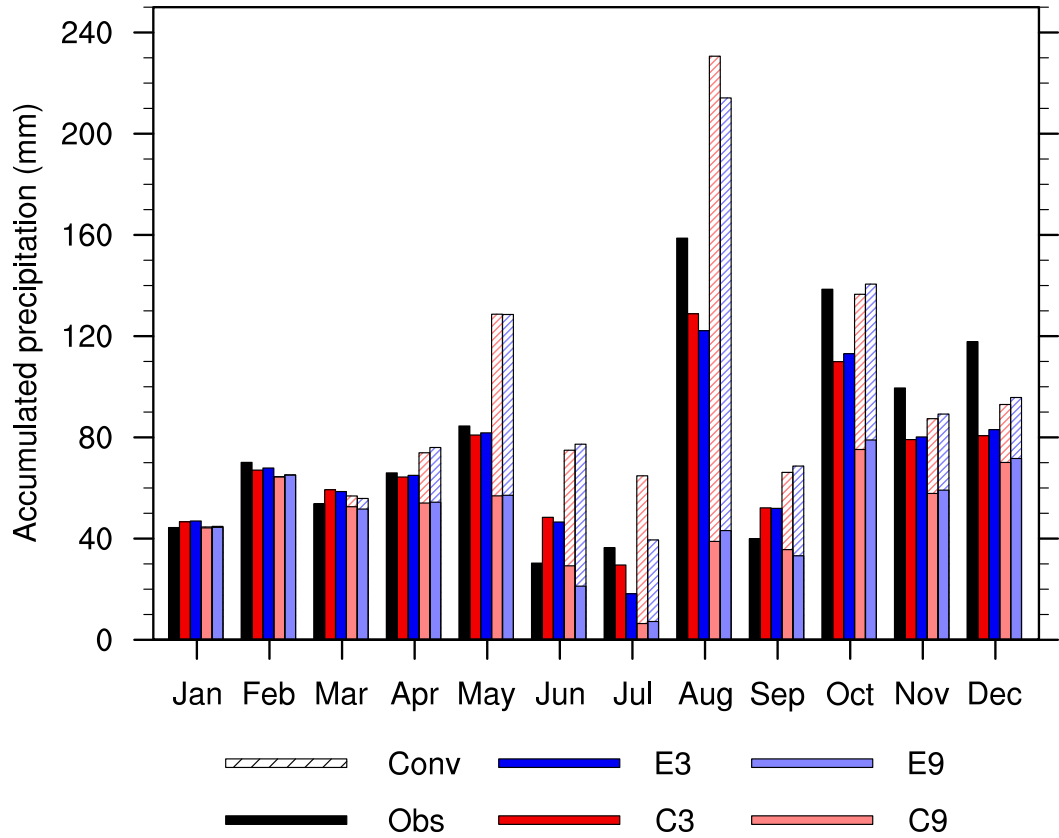
Figure 5.   Monthly-averaged accumulated precipitation (mm) over Denmark derived from gridded observations and simulations in the 10×10 km grid. Simulations using the KF-CPS scheme are represented by both the convective (stribed) and non-convective (solid) precipitation.
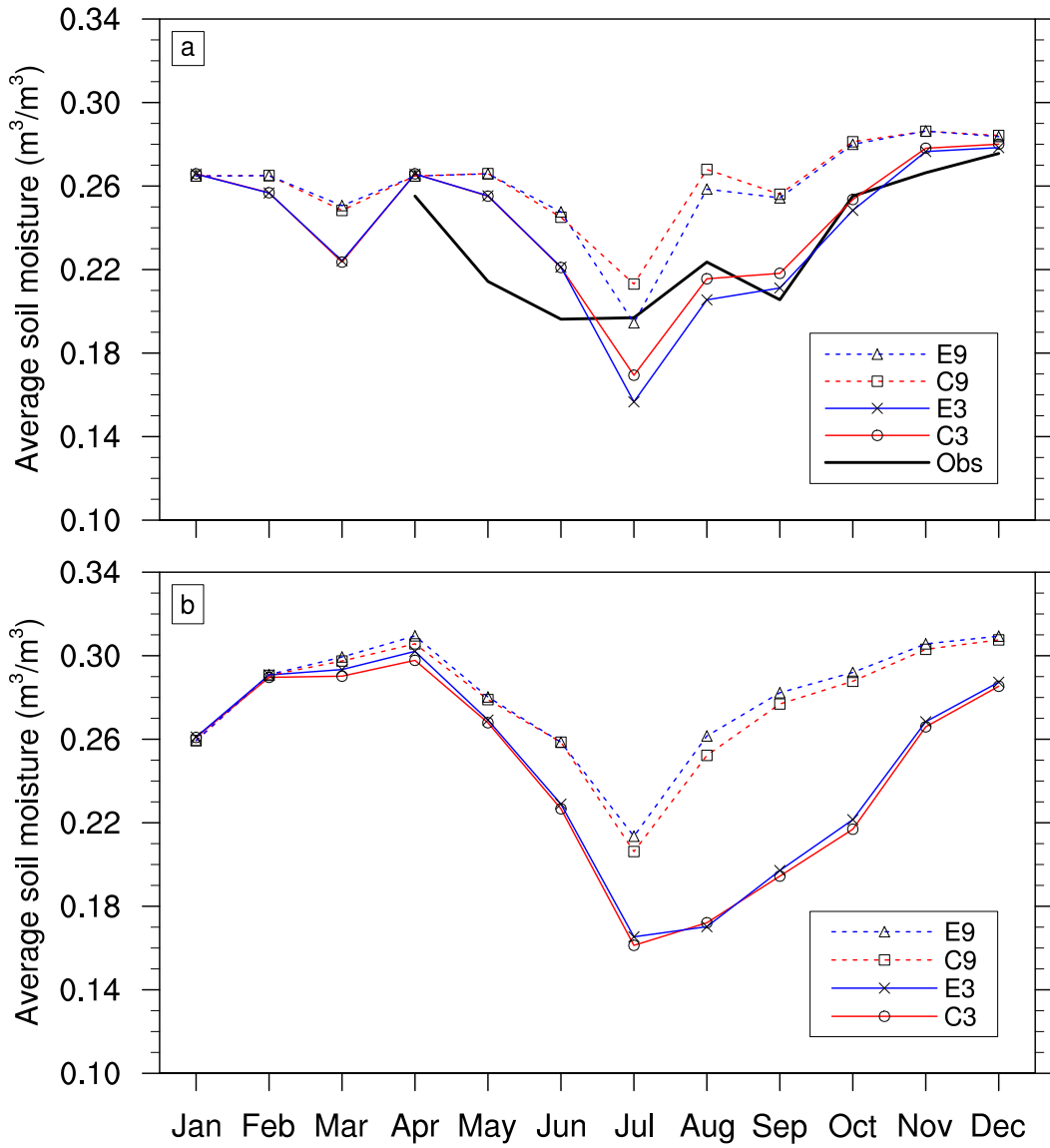
Figure 6.   Monthly-averaged soil moisture content $(\mathrm{m^3\,m^{-3}})$ over Denmark in: (a) top soil layer (0–0.1 m) on ESA-CCI grid, and (b) upper 1 m all WRF grid squares.
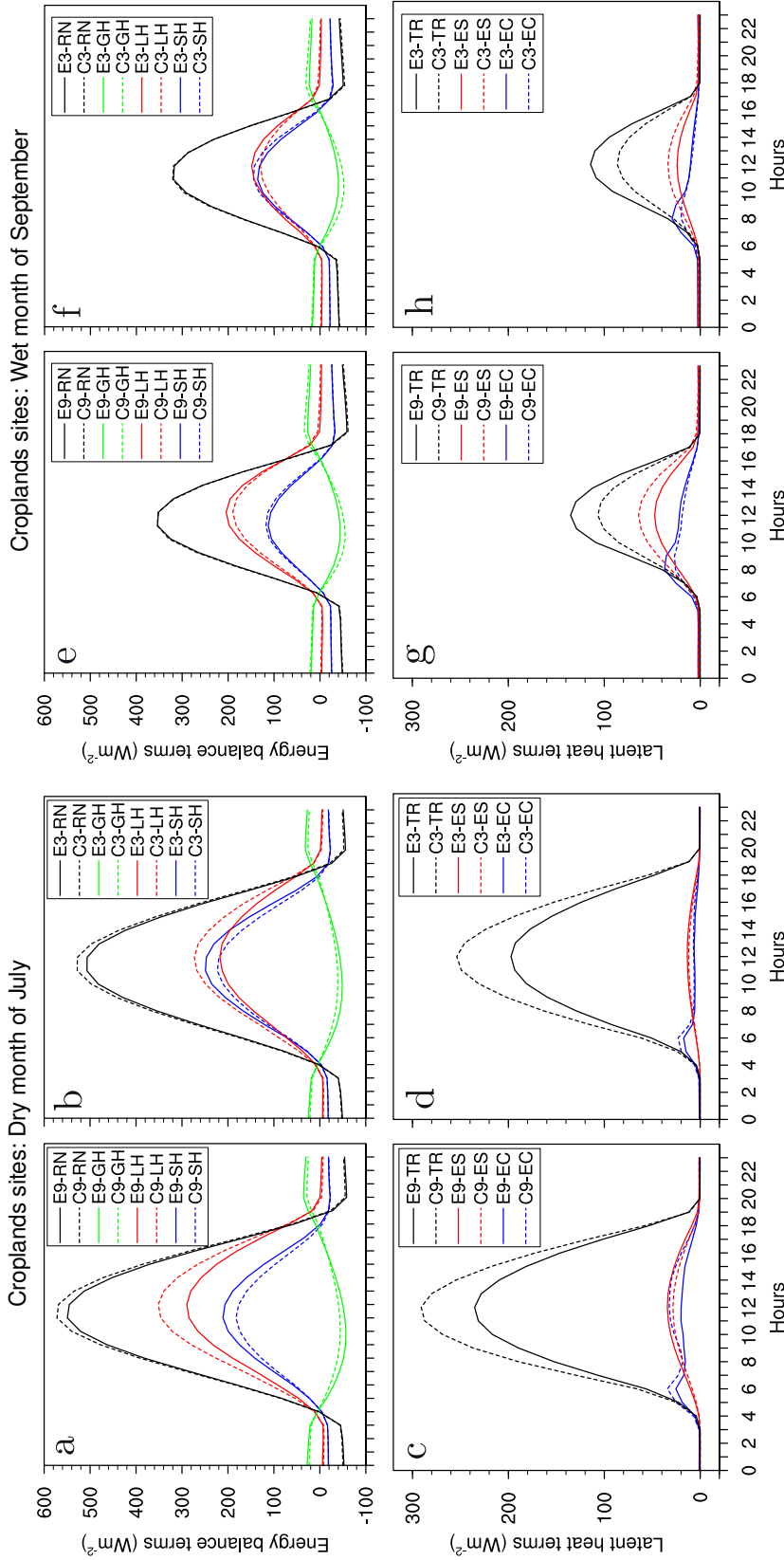
Figure 7. Mean diurnal cycles over CL for the components of the surface energy balance (a, b, e, and f) and the latent heat fluxes (c, d, g, and h) during July (a–d) and September (e–h) over Denmark during 2006. Components of the surface energy balance for C9 and E9 (a and e) and C3 and E3 (b and f): net radiation (RN), sensible heat flux (SH), latent heat flux (LH) and ground heat flux (GH). Components of the latent heat flux for C9 and E9 (c and g) and C3 and E3 (d and h): transpiration (TR), soil evaporation (ES) and evaporation of intercepted water by vegetation canopy (EC). Units in W m^{-2}.
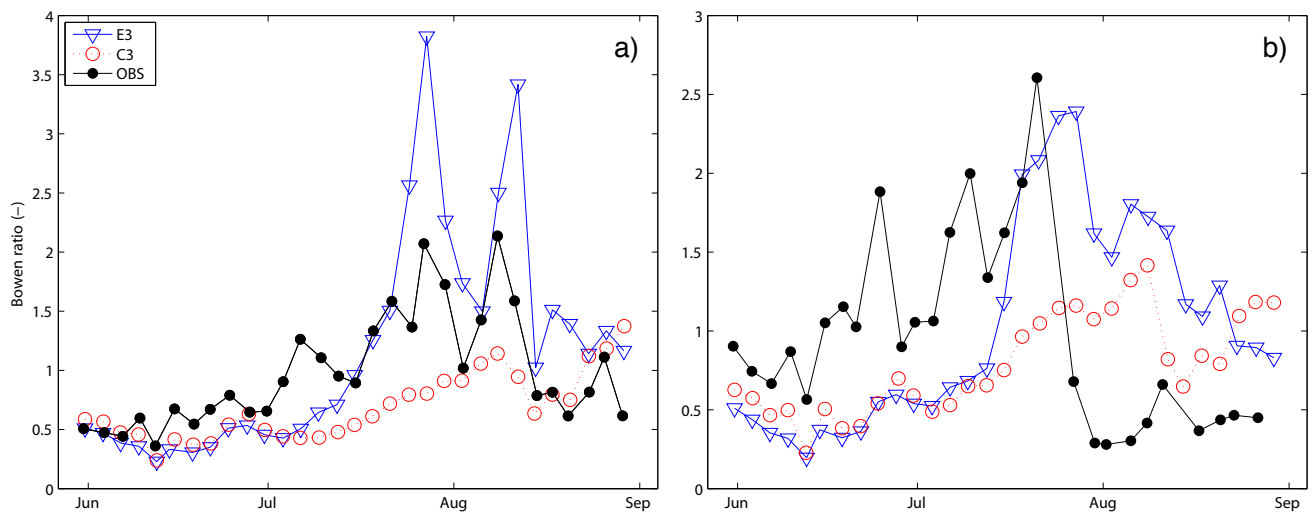
Figure 8. Temporal evolution of Bowen ratios during JJA at (a) "Risbyholm" and (b) "Lille Valby" for the observations and the simulations C3 and E3. The station locations are indicated by red stars in Fig. 1.
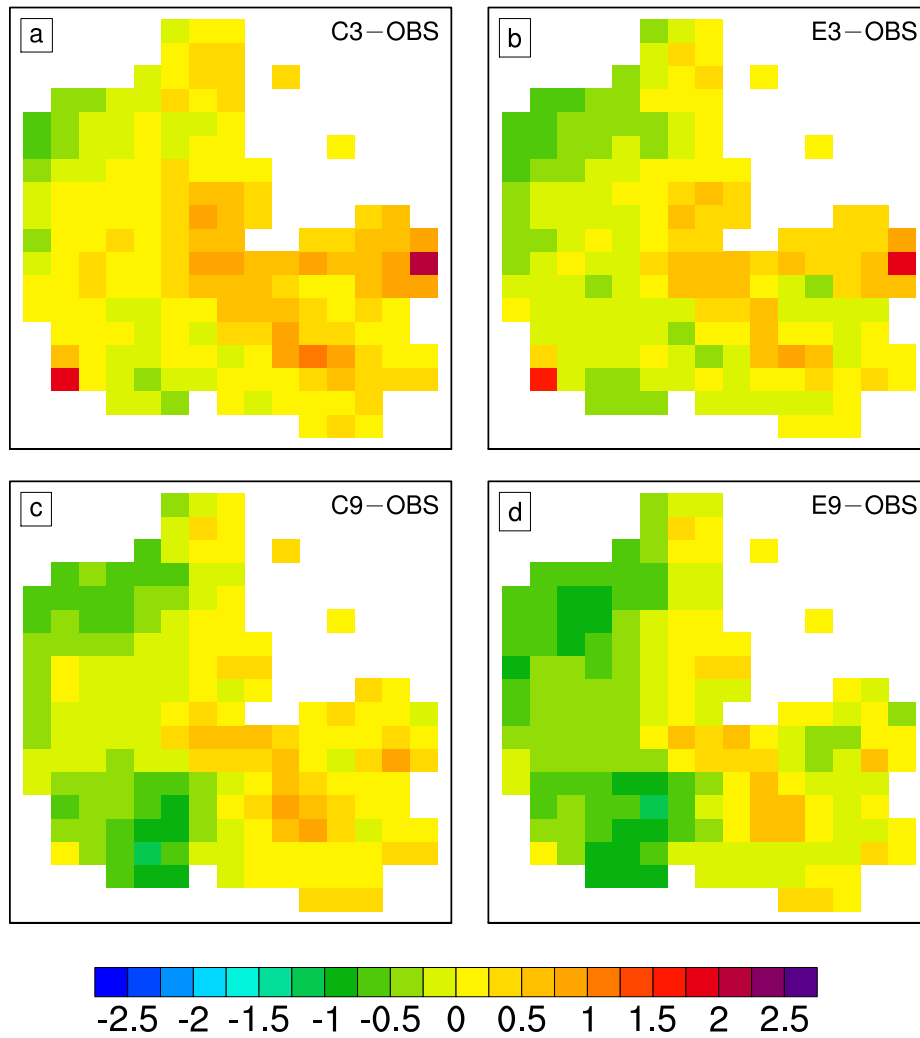
Figure 9. Differences (WRF minus observations) in September averaged 2-m temperature (K) on the 20×20 km DMI climate grid for the simulations: (a) C3, (b) E3, (c) C9, and (d) E9.
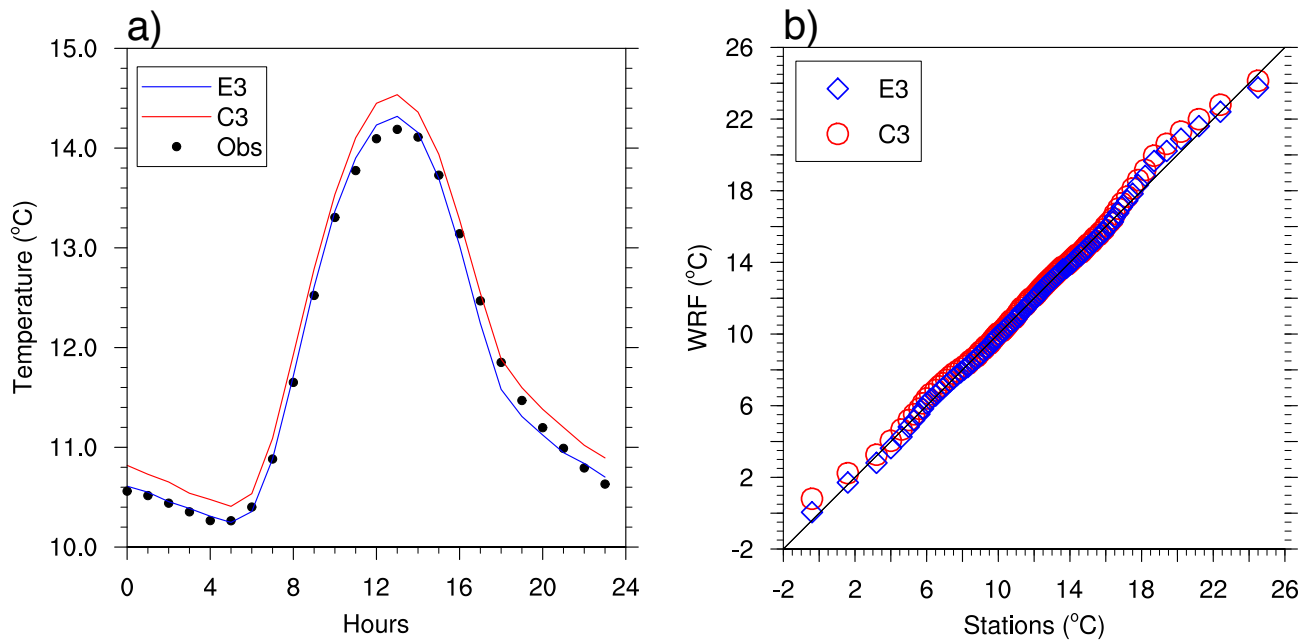
Figure 10.   (a) Average diurnal cycle and (b) Q-Q plot of the 2-m temperature during SON computed at the 10 stations (black circles) shown in Fig. 1. Units in °C.
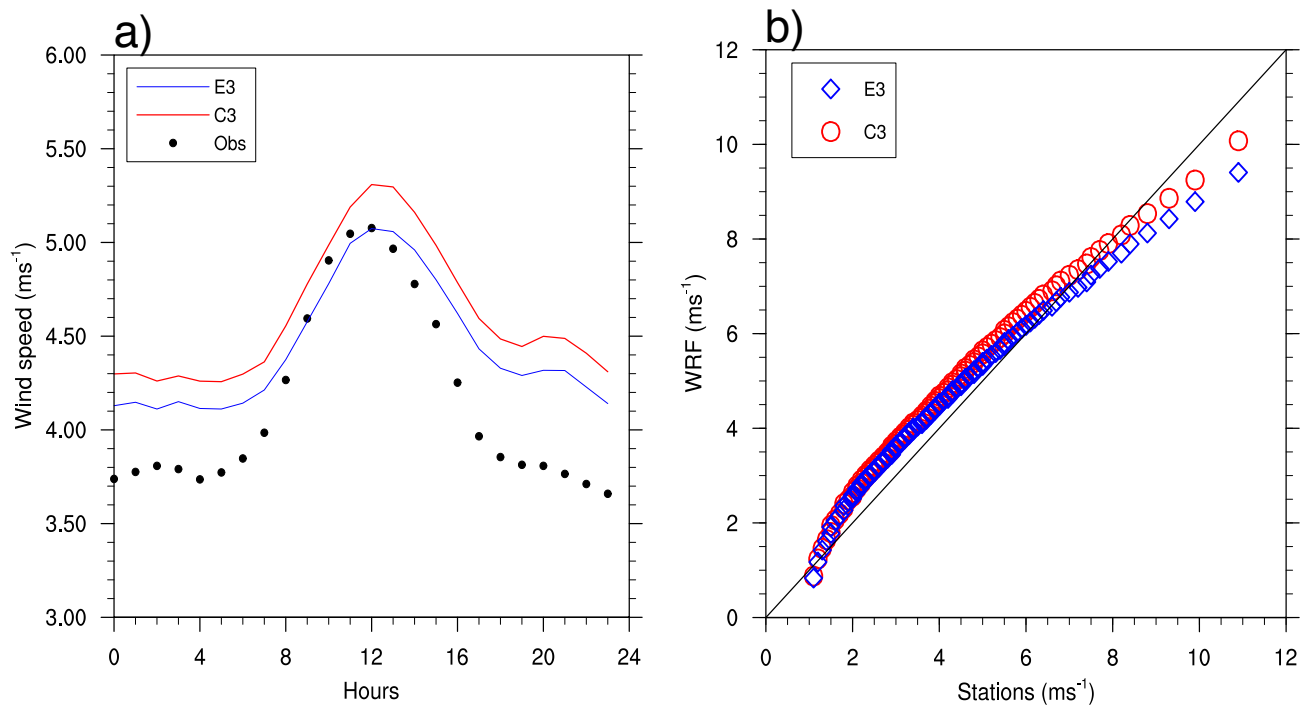
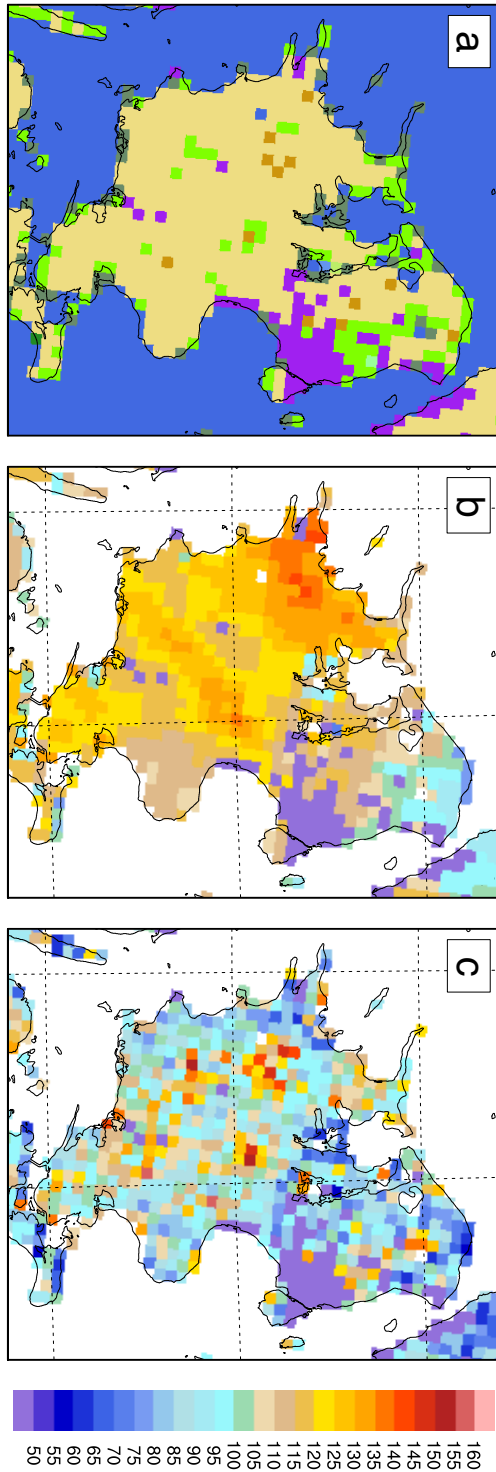**Figure 11.** As in Fig. 10 but for 10-m wind speeds in $\mathrm{m\,s}^{-1}$.

Figure 12. (a) Land use categories (as in Fig. 1) and total mean latent heat flux (W m^{-2}) over the Island of Zealand (Denmark) during July 2006 for (b) C3 and (c) E3.